UAB
Universitat Autònoma de Barcelona

Lesky Wave Antennas and Electromagnetic Field Confinement Devices based on Periodic and Uniform Structures

Alvaro-Patricio Jaque Jiménez

ADVERTIMENT. L'accés als continguts d'aquesta tesi doctoral i la seva utilització ha de respectar els drets de la persona autora. Pot ser utilitzada per a consulta o estudi personal, així com en activitats o materials d'investigació i docència en els termes establerts a l'art. 32 del Text Refós de la Llei de Propietat Intel·lectual (RDL 1/1996). Per altres utilitzacions es requereix l'autorització prèvia i expressa de la persona autora. En qualsevol cas, en la utilització dels seus continguts caldrà indicar de forma clara el nom i cognoms de la persona autora i el títol de la tesi doctoral. No s'autoritza la seva reproducció o altres formes d'explotació efectuades amb finalitats de lucre ni la seva comunicació pública des d'un lloc aliè al servei TDX. Tampoc s'autoritza la presentació del seu contingut en una finestra o marc aliè a TDX (framing). Aquesta reserva de drets afecta tant als continguts de la tesi com als seus resums i índexs.

ADVERTENCIA. El acceso a los contenidos de esta tesis doctoral y su utilización debe respetar los derechos de la persona autora. Puede ser utilizada para consulta o estudio personal, así como en actividades o materiales de investigación y docencia en los términos establecidos en el art. 32 del Texto Refundido de la Ley de Propiedad Intelectual (RDL 1/1996). Para otros usos se requiere la autorización previa y expresa de la persona autora. En cualquier caso, en la utilización de sus contenidos se deberá indicar de forma clara el nombre y apellidos de la persona autora y el título de la tesis doctoral. No se autoriza su reproducción u otras formas de explotación efectuadas con fines lucrativos ni su comunicación pública desde un sitio ajeno al servicio TDR. Tampoco se autoriza la presentación de su contenido en una ventana o marco ajeno a TDR (framing). Esta reserva de derechos afecta tanto al contenido de la tesis como a sus resúmenes e índices.

WARNING. The access to the contents of this doctoral thesis and its use must respect the rights of the author. It can be used for reference or private study, as well as research and learning activities or materials in the terms established by the 32nd article of the Spanish Consolidated Copyright Act (RDL 1/1996). Express and previous authorization of the author is required for any other uses. In any case, when using its content, full name of the author and title of the thesis must be clearly indicated. Reproduction or other forms of for profit use or public communication from outside TDX service is not allowed. Presentation of its content in a window or frame external to TDX (framing) is not authorized either. These rights affect both the content of the thesis and its abstracts and indexes.

UAB
Universitat Autònoma
de Barcelona

Leaky Wave Antennas and Electromagnetic Field Confinement Devices based on Periodic and Uniform Structures

Ph. D. Thesis written by
Álvaro-Patricio Jaque Jiménez

Under the supervision of
Jordi Bonache Albacete
and
Gerard Zamora González

Bellaterra, December 2023

UAB
Universitat Autònoma
de Barcelona

Leaky Wave Antennas and Electromagnetic Field Confinement Devices based on Periodic and Uniform Structures

Ph. D. Thesis

Written by
Álvaro-Patricio Jaque Jiménez

Under supervision of
Prof. Jordi Bonache Albacete
and
Dr. Gerard Zamora González

Ph. D. programme in Electronic and Telecommunication Engineering

Universitat Autònoma de Barcelona

Electronic Engineering Department

Bellaterra (Cerdanyola del Vallès), December 2023

UAB
Universitat Autònoma
de Barcelona

The undersigned, **Prof. Jordi Bonache Albacete** and **Dr. Gerard Zamora González**, Professors of the Electronic Engineering Department (Engineering School) of the *Universitat Autònoma de Barcelona*,

CERTIFY:

That the thesis entitled "*Leaky Wave Antennas and Electromagnetic Field Confinement Devices based on Periodic and Uniform Structures*" has been written by the Ph.D. candidate **Álvaro-Patricio Jaque Jiménez** under their supervision, in fulfilment of the requirements of the PhD programme in Electronic and Telecommunication Engineering.

And hereby to acknowledge the above, sign the present.

Universitat Autònoma de Barcelona
Engineering School
Electronic Engineering Department

Bellaterra (Cerdanyola del Vallès), December 2023.

Contents

Contents i

Acknowledgments iii

Summary v

1. Motivation and objectives 1

2. Introduction 7

2.1 Space harmonics and k vs β diagram 7

2.2 Leaky Wave Antennas 10

2.3 Electromagnetic field confinement device 25

2.3.1 Applications, Market Scope, and State of the Art 26

2.3.2 Principle of operation of EMFCD 28

3. Microwave devices 3D printing-based prototyping 43

3.1 Characterization of the metallization processes 44

3.2 Microstrip devices based on 3D printing 53

3.2.1. Stepped impedance filter design 54

3.2.2. Filter prototyping and measured results 56

3.3 Waveguide prototyping based on 3D printing 58

3.3.1 Horn antenna 59

3.3.1.1 Pyramidal horn antenna design 60

3.3.1.2 Prototyping and measured results 63

3.3.2 Slotted waveguide 67

3.4 3D prototyping conclusions 68
4. Leaky Wave Antenna Design 75
4.1 Proposed Unit Cell and analysis 75
4.2 Design of the Leaky Wave Antenna 83
4.3 Fabrication and experimental results 91
4.4 Conclusions 98
5 Design of Electromagnetic Field Confinement Devices 105
5.1 Electromagnetic Field Confinement based on SIW for RFID applications 105
5.1.1 Principle of operation 106
5.1.2 Device design 108
5.2 Electromagnetic Field Confinement based on Waveguide 118
5.2.1 Principle of operation 118
5.2.2 Device design 120
5.3 Comparison and conclusions 133
Conclusions and future work 139
APPENDIX I 143
APPENDIX II 147
Author list of publications 149

Acknowledgments

I would like to express my deepest gratitude to my thesis supervisors, Porf. Jordi Bonache Albacete and Dr. Gerard Zamora González, for their invaluable guidance, unwavering support, and knowledge throughout the entire research process. Their experience and dedication have been instrumental in shaping this work.

A special thanks to my colleagues from the department, Jonathan Muñoz, Emili Salvador, Martí Raya, Anna Ruiz, Matteo Villani, Jan Coromina, Ferran Paredes, Paris Vélez and Gerard Sisó, whose collaboration and camaraderie not only made the research journey more enjoyable but also created many great memories together. Moreover, I would like to show my appreciation to my friends Jin, Gerard, Rocío, Panda, Xavi, Sergio, Adri and Taba, among others for being there and contributing to numerous good moments.

Finally, thanks must also go to all my family, especially my parents, Maria Jesús and Patricio for their unwavering support and love, to my sister, Julia, for being my constant source of inspiration, to my cousins, Diego and Rubén, to my aunt Conchi and my uncle Javi and to my grandmother Concepcion. Furthermore, I would like to dedicate a special memory to my grandfather, Félix, who unfortunately left us during the COVID-19 pandemic. His memory and influence in my life will always be cherished.

Heartfelt thanks to everyone who generously shared their time, love, and positive energy, making the journey towards this Ph.D.

Álvaro-Patricio Jaque Jiménez

Summary

In recent years, significant effort has been done to the study and development of telecommunication devices and technologies. The increasing use of wireless communication and the rising needs of different applications have led to innovation in antenna design and functionality. Furthermore, in the context of the Internet of Things, new needs must be addressed not only in long-range communication systems but also in near-field applications.

This thesis focuses around two key aspects: the design of electromagnetic field confinement devices, which rely on generating evanescent waves through periodic and uniform structures, and the design of leaky wave antennas. The former is essential for close-range applications (for example RFID, wireless energy transfer, drug monitoring, etc.), enabling interaction between the field and transponders, sensors, actuators, and other components. On the other hand, the latter finds application in diverse scenarios such as radar systems, object tracking, information transmission, imaging, and more. Moreover, this thesis explores the realm of prototyping microwave devices using 3D printing, offering a cost-effective and efficient approach to construct intricate structures. Furthermore, diverse methodologies for metallizing the printed structures have been proposed and tested. The results obtained in this thesis extend the state-of-the-art in the field of leaky wave antennas and electromagnetic field confinement devices. Proof-of-concept prototypes support the validity and viability of the suggested devices. Theoretical analysis, electromagnetic simulations, and experimental results exhibit a high level of concordance.

Chapter 1

Motivation and objectives

The transmission and reception of information has been a fundamental requirement in the development of human society. The earliest telecommunications technologies employed to transmit information across distances visual cues be means of beacons or smoke, and acoustic signals with tools like drums, horns, and trumpets. Telecommunications have evolved significantly since then, becoming not only a fundamental element of our modern environment but also a revolutionary force shaping our interactions with the world [1]-[3]. They play a critical role in binding our society together, bridging gaps between distant regions, and enabling the global exchange of information. Telecommunications drive essential concepts like globalization, Internet of Things, and the advent of Industry 4.0. They become indispensable in an extensive array of activities, including financial, commercial, entertainment, and business activities. Moreover, their influence extends to automation application, tracking object in real time, efficient control of industrial processes, and enhancing resource management efficiency, among others.

Antennas, as integral components of wireless communication systems, play a central role in this evolution. They serve as the interface between wired systems and the propagation of waves through free space, enabling the transfer of signals. The behavior of antennas is thoroughly explained by Maxwell's

equations, offering a strong understanding. The historical development of antennas includes iconic designs such as the dipole antenna, parabolic antenna (parabolic reflector), Yagi-Uda antenna, among others [4]-[9]. The rapid growth of wireless communications, microwave sensors, remote control, imaging needs, and radars has triggered the introduction of innovative antenna designs over the past decade. The use of powerful computational tools has further fueled this innovation, enabling the realization of new antenna designs driven by a desire for more efficient, multifunctional, and cost-effective solutions. The commercial mobile communications industry has been a key driver in the growing demand for antenna design, with antennas now widely used in public applications such as cellular communication, 5G, 6G, GPS, satellite connections, WIFI, RFID, Bluetooth, among other technologies.

In the field of communication systems, there's a rising demand for applications that ensure precise interaction within specific volumetric regions between the transmitting device and the receiving entity (including samples, actuators, transponders, or sensors). Some examples of such applications include points of sale at shops with desktop RFID readers, wireless energy transfer, optical fiber coupling for biosensor applications, therapeutic drug monitoring, and efficient control of department stores, among others. Conventional antenna designs face significant challenges in achieving effective control over the illumination area, as radiation often leaks beyond the intended range, making it difficult to ensure the desired level of confinement. These limitations underscore the need for new and innovative solutions. In this context, our research group proposes a novel structure concept, called electromagnetic field confinement device, aimed at addressing these challenges and opening the door to improved designs that provide better control and efficiency in confined communication scenarios.

Nowadays 3D printing is revolutionizing the way to create intricate structures and models that used to be expensive and technically challenging to build. In the world of microwave device manufacturing, this breakthrough opens up new possibilities for cheap prototyping. While our research group has the means to independently self-produce prototypes in planar technology (e.g., microstrip) with a milling machine, the production of waveguides continues to present a significant challenge. The accessibility of 3D printers, however, offers

a unique opportunity that enables us to explore new design and technological possibilities.

The aim of this thesis is to advance beyond the current state of Leaky-Wave Antennas, by introducing new designs based on waveguides that ensure proper functionality within their operational bandwidth. Additionally, the study will continue by exploring new designs for electromagnetic field confinement devices, specifically for RFID and high-power applications, using SIW and air-filled waveguide technology. As a secondary objective, different approaches for prototyping microwave devices using the tools and materials available within our research group will be analyzed for their feasibility. With these goals in mind, the thesis has been organized as follows:

- **Chapter 1** introduces the current motivation and objectives of this thesis, delineates how the thesis has been structured in each successive chapter, and shows the projects and grants that contribute to its development.
- **Chapter 2** is an overview of leaky wave antennas (LWAs) and electromagnetic field confinement devices (EMFCDs), their applications, and their potential impact on the market. Concepts like "space harmonic" and the "k vs. β diagram" are introduced to aid in understanding the discussed terminology.
- **Chapter 3** is focused on the exploration of 3D printing prototyping for telecommunications devices. It delves into the feasibility of various materials and metallization processes. The chapter involves the design of diverse communication devices using both planar and waveguide technology, aiming to assess the potential of in-house fabrication for subsequent devices.
- **Chapter 4** is dedicated to the design of a periodic leaky-wave antenna featuring backward-to-forward scanning capability. A novel design approach is put forth to efficiently address the open stopband issue inherent in periodic structures, that degrades the radiated beam around the broadside direction. Within this context, two antenna versions (with unidirectional and bidirectional radiation pattern) based on the same periodic structure are proposed, analyzed, fabricated, and characterized.

Furthermore, a matching network based on coaxial to waveguide transition is designed.

- **Chapter 5** is dedicated to the proposal and analysis of different electromagnetic field confinement devices. This chapter delves into the surface wave mode using two different approaches. The former based on uniform structure in SIW technology, and the later based on periodic structures in air-filled waveguide technology. Moreover, two matching networks to feed the different structures are designed.
- **Chapter 6** summarizes the most significant outcomes and contributions presented in this thesis. Moreover, this chapter proposes future research lines that stem from the results of this thesis.

The research conducted for this thesis, spanning the years 2018 to 2023, was carried out within the GEMMA/CIMITEC group (Grup d'Enginyeria de Microones, Metamaterials I Antenes / Centre d'Investigació en Metamaterials per a la Innovació en Tecnologies Electrònica i de Comunicacions) from 2018 to 2021 and the research group formed by Jordi Bonache and Gerard Zamora from 2021 to 2023, both of which are integral parts of the Electronics Engineering Department at the Universitat Autònoma de Barcelona. The activity of GEMMA-CIMITEC has been focused on RF/microwave engineering, and its research scope encompasses metamaterials, printed electronics, 3D printing, microfluidics, RFID, among others. Similarly, within the new group founded by Jordi and Gerard, their work in the field of RF/microwave engineering primarily revolves around the application of advanced concepts and technology for the design of RFID devices, electromagnetic field confinement devices, leaky wave antennas, 3D printing prototyping, among others.

This work has been funded by the Catalan and Spanish governments through various projects. Among the projects and contracts with different institutions and companies that have provided support for the development of these activities, we would like to acknowledge and highlight the following:

- Project TEC2016-75650-R by the Spanish Government. Title: *Diseño y síntesis de componentes de RF/microondas basados en conceptos avanzados y su aplicación a circuitos de comunicaciones, sensores y RFID (II).*

- Project PID2019-103904RB-I00 by the Spanish Government. Title: *Diseño y sintesis de componentes de RF/microondas basados en conceptos avanzados y su aplicacion a circuitos de comunicaciones, sensores y RFID (III).*

Finally, this Ph.D. thesis has also received support from a predoctoral fellowship FPI (Formación de Personal Investigador) grant from the Spanish ministry of Economia, Industria y Competitividad, with the reference BES-2017-081387.

REFERENCES

[1] Tom Standage, *"The Victorian Internet: The Remarkable Story of the Telegraph and the Nineteenth Century's On-line Pioneers."* Bloomsbury USA, 2014.

[2] José María Romeo López, Rafael Romero Frías. *"El ferrocarril y el telégrafo."* Fundación Telefónica and Departamento de Ingeniería Audiovisual y de Comunicaciones de la UPM, 2013.

[3] James Gleick, *"The Information: A History, A Theory", A Flood.* Fourth Estate, 2012.

[4] C. A. Balanis, *"Modern Antenna Handbook"*, Hoboken, NJ, USA:Wiley, 2008.

[5] J. L. Volakis, Antenna Engineering Handbook, USA, NY, New York:McGraw-Hill, 2007.

[6] Richard C. Johnson, *"Antenna Engineering Handbook"*, third edition, USA, NY, New York:McGraw-Hill, 2007

[7] Warren L. Stutzman, Gary A. Thiele, "Antenna Theory and Design" third edition, Hoboken, NJ, USA:Wiley, 2012

[8] Dennis Roddy, *"Satellite Communications"*, third edition, New York, NY, USA:McGraw-Hill, 2001

[9] C. A. Balanis, *"Antenna Theory: Analysis and Design"*, fourth edition, Hoboken, NJ, USA:Wiley, 2016

Chapter 2

Introduction

This chapter provides an overview of leaky wave antennas (LWAs), outlining different configurations and types, as well as discussing their key characteristics. It also includes an analysis of their current state of art and market scope. Moreover, the chapter serves as an introduction to electromagnetic field confinement devices (EMFCDs), while also delving into a discussion of the current state of the art, which sets the foundation for this research. The concept of ***space harmonic*** and the ***k vs. β diagram*** are shown, providing information about the concepts and terminology used throughout the discussion of both types of devices. Through these explanations and analyses, the chapter aims to lay a solid foundation for understanding and exploring leaky wave antennas and electromagnetic field confinement devices.

2.1 Space harmonics and k vs β diagram

In the realm of microwaves and radiofrequency technology, the analysis of radiation and signal propagation is essential for understanding and designing efficient and effective systems. Among the most powerful tools for visualizing and comprehending the dispersion and behavior of electromagnetic waves in antennas is the ***k* vs. *β* diagram**. This diagram provides valuable insight into the interaction between the propagation constant k_0 and the phase constant β

of a structure, allowing the analysis of wave propagation and scattering in various directions and frequencies as they interact with these structures. To enhance comprehension of this diagram, introducing the concept of space harmonics, particularly in the context of periodic structures, is essential.

When a periodic element is introduced into a uniform structure with a separation distance d, space harmonics emerges [1]. These harmonics represents different wave components that collectively contribute to the overall electromagnetic field.

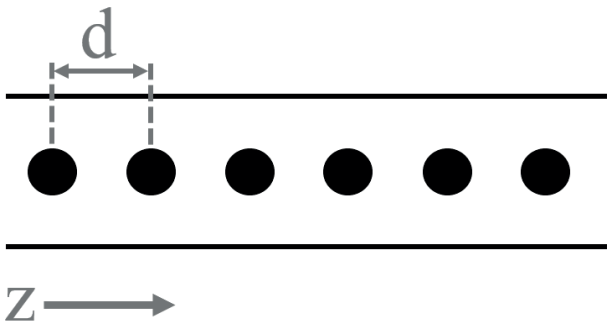


Figure 2.1. Uniform structure loaded with a periodic element.

According to Floquet's theorem, the behavior of the field within the periodic structure can be described as a combination of a fundamental traveling wave with a propagation wavenumber k_0 and a standing wave $P(z)$ that exhibits periodicity with the same pattern every distance d along the transmission direction z. This periodicity is defined by the following condition:

$$P(z) = P(z + d) \tag{2.1}$$

Expressing the standing wave $P(z)$ within each period d as a Fourier series gives:

$$P(z) = \sum_{n=-\infty}^{+\infty} P_n e^{-j(2\pi n/d)z} \tag{2.2}$$

Which leads to a representation of the waveform in terms of an infinite number of space harmonics:

$$\Psi(z) = e^{-\alpha z} \sum_{n=-\infty}^{+\infty} P_n e^{-j\beta_n z} \tag{2.3}$$

Where α is the attenuation constant of the propagated wave, and β_n is the phase constant of a specific n—space harmonic. The phase constant of each space harmonic can be defined as follows:

$$\beta_n = \left(\beta + \frac{2\pi n}{d}\right) \tag{2.4}$$

Where n is an integer representing the nth space harmonic. The understanding of how electromagnetic waves interact with periodic elements becomes particularly valuable when designing antennas [1]-[3], metamaterial structures [4]-[5], photonic crystals [6]-[8], optical gratings [9]-[11], and other electromagnetic devices based on periodic elements.

In figure 2.2 the dispersion diagram of air-filled rectangular waveguide periodically loaded with radiator elements (for i.e. rectangular slots placed in the wide wall) spaced d is represented according to equation (2.4).

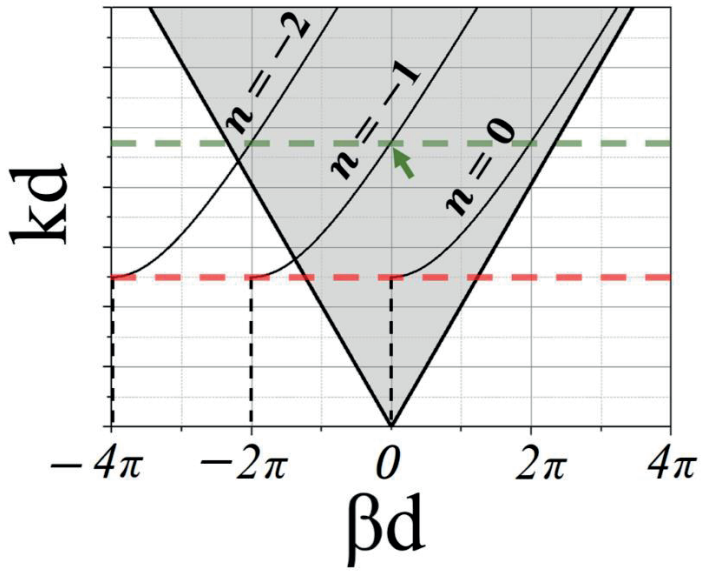


Figure 2.2. Representation of the dispersion diagram for different space harmonics within a periodically loaded air-filled waveguide. Radiation region is highlighted in gray. Red dotted line indicates cutoff frequency of the fundamental TE_{10} mode, and green dotted line indicate broadside frequency for the space harmonic n-1.

On the dispersion diagram, lines corresponding to different Floquet harmonics indicate the conditions under which electromagnetic waves can propagate within the periodic structure. In the specific context of antenna

design, valuable insights can be derived from the k vs. β diagram, yielding the following information:

- ***Radiation direction:*** The radiation direction of an antenna refers to the main direction in which the antenna emits or receives radiofrequency signals with maximum efficiency. Examination of the Floquet harmonics' positioning relative to the light cone unveils the radiation direction. The light cone essentially acts as a constraint in reciprocal space (Brillouin diagram), determining the region where the antenna radiates efficiently. When some space harmonic is located within the light cone and the first quadrant of the diagram, radiation occurs in the forward direction, aligned with the signal's propagation within the antenna. A phase constant β=0 implies broadside radiation. In this case, the waves propagate perpendicular to the propagation direction. When the phase constant lies within the second quadrant of the diagram, the radiation direction becomes backward. This indicates electromagnetic waves are emitted in the direction opposite to the signal's propagation within the structure. Finally, when the phase constant intersects with the light cone, the radiation is referred to as endfire or backfire, if it is in the first quadrant or the second quadrant, respectively.
- ***Cutoff Frequency:*** The cutoff frequency of an antenna is the minimum frequency at which the antenna can transmit or receive signals efficiently. Below this cutoff frequency, the antenna will not operate optimally, and signal propagation will be deficient. In figure 2.2 red dotted line indicate cutoff frequency of the fundamental TE_{10} mode (higher order modes are omitted).
- ***Grating lobes:*** These lobes represent additional directions in which a periodic antenna can emit or receive signals efficiently, apart from the main or desired direction. The presence of grating lobes becomes evident by observing overlapping regions in the dispersion diagram, where multiple harmonics coexist at the same frequency region within the light cone.

2.2 Leaky Wave Antennas

Leaky Wave Antennas have been one of the most active areas of research in microwave engineering since 40's when a slotted rectangular waveguide LWA was proposed [12]. Leaky-wave antennas are based on a wave propagating along a guiding structure (travelling-wave structures) and gradually leaking its energy out to free-space in coherent radiation [13]-[14]. LWAs have gained

significant popularity in the microwave and higher frequency ranges due to their ability to achieve high directivity, narrow beamwidth over a wide frequency band (typically from about 1% to 10%), and beam scanning capability with a simple structure without the need for a complicated and costly feed network unlike array antennas [13], [15].

Main characteristics of 1-D LWAs

Leaky-wave antennas can be classified based on two principles. One is based on the wave propagation and other is on feeding location. These factors will influence the performance of the antenna.

When examining the wave propagation characteristics, LWAs can be categorized into two types: 1-Dimensional LWAs and 2-Dimensional LWAs. In the realm of 1-Dimensional LWAs, the antenna structure supports the waves which are travelling in a predetermined direction. On the other side, 2-Dimensional LWAs introduce a more intricate design, employing a guiding structure that facilitates radial wave propagation originating from the feed point. This design is a simple and easy way of receiving a beam pattern oriented in the broadside direction. 2-D LWAs are having a partially reflecting surface on the upper side of ground structure. 1-D LWAs are generally divided into three categories depending on the geometry: uniform, quasi-uniform, and periodic. Each category presents different performance attributes regarding main lobes, scanning range, dimensions, and more.

The performance of LWAs will also vary based on the feeding location. Typically, LWAs are fed at one end, allowing the wave to propagate along the structure's axis [2.3. (a)]. Alternatively, a center feed that generates bidirectional excitation is also possible [2.3. (b)]. It will become evident that a center feed proves valuable in generating broadside beams, particularly in structures where beam steering is limited to a single quadrant. Before delving into a more detailed discussion of the 1-D LWAs categories, it is important to describe the most significant attributes in antenna design. Below are descriptions of some of the most important terms related to Leaky Wave Antennas [16]-[17]:

- ***Radiation Pattern:*** Describes how the antenna radiates electromagnetic energy in different directions, providing insights into the directional behavior of the antenna's emission.

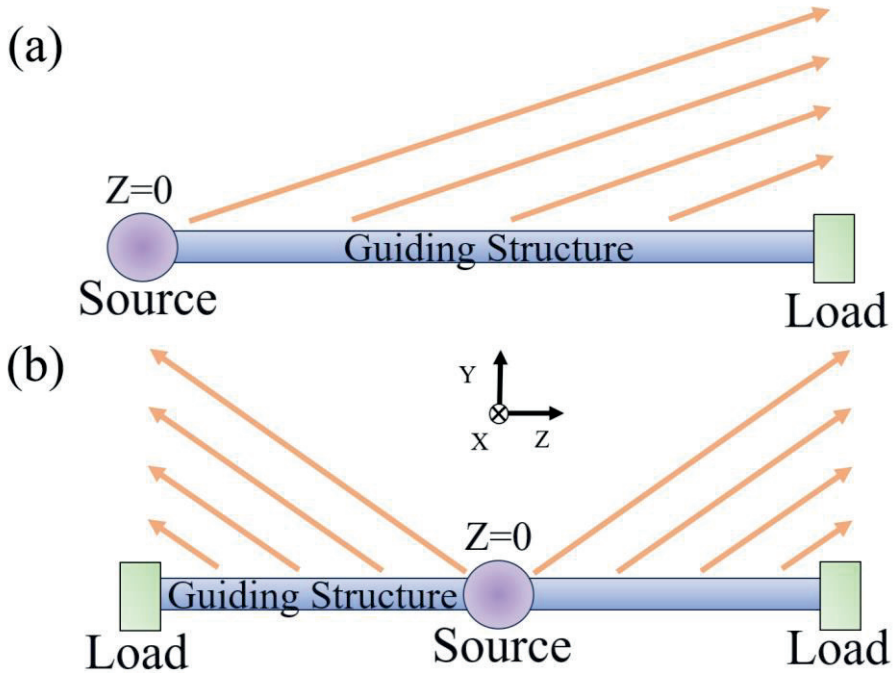


Figure 2.3. Illustration of different LWA feed modes. (a) Source located at one end of the guiding structure. (b) Source located in the center of the guiding structure.

- ***Directivity:*** Defined as the ratio between the radiation intensity of the antenna in the direction of its maximum and the radiation intensity of an isotropic antenna that radiates with the same total power. Directivity has no units and is commonly expressed in logarithmic units (dBi).
- ***Gain:*** Established as the power gain in the direction of maximum radiation. The unit of antenna gain is dBi.
- ***Beamwidth:*** Defines the angular span between the half-power points of the main lobe in the radiation pattern, providing information about the angular coverage of the antenna's emission.
- ***Scanning Capabilities:*** Refers to the antenna's ability to steer its radiation pattern in different directions.
- ***Leakage Constant:*** Describes the rate of power leakage along the antenna structure, influencing the antenna's directivity and radiation efficiency.
- ***Bandwidth:*** Specifies the range of frequencies over which the antenna's performance remains within acceptable limits, providing an indication of the frequency range of effective operation.

- ***Radiation Efficiency:*** Measures the proportion of input power that is converted into radiated power, providing insights into the antenna's effectiveness in transmitting electromagnetic energy.
- ***Frequency Sensitivity:*** Describes how the main beam angle of the antenna changes with variations in frequency, typically measured in degrees per Hertz (°/Hz).
- ***Aperture distribution:*** Is the space distribution or pattern of current or power across the aperture (opening) of an antenna. The aperture distribution is a fundamental characteristic of an antenna's design and operation, and it plays a significant role in determining the antenna's radiation properties.
- ***Sidelobe level (SLL):*** Quantifies how much electromagnetic energy is radiated in the sidelobes. Typically, in uniform aperture distribution, sidelobes are 13 dB lower than main lobe. A lower sidelobe level is generally desirable for many antenna applications to maximize directivity, reduce interferences, and avoid false detections.
- ***Antenna Size:*** Physical dimensions of the LWA. Often indicated in terms of wavelength.
- ***Polarization:*** Describes the orientation of the electric field vector of the radiated electromagnetic wave, which influences the wave's interaction with other objects and media.

Typically, the radiation efficiency e_r aiming for around 90% efficiency and can be approximated with the load absorption by

$$e_r = 1 - e^{-2\alpha L} \tag{2.5}$$

Where α is the leakage constant (i.e. attenuation constant without considering dielectric or ohmic losses), and L the total length of the radiating aperture. Another characteristic of the LWA is that typically emits a conical beam at an angle θ from the z-axis [Fig.2.4. (a)]. Furthermore, when multiple LWAs are arranged side by side, it is possible to achieve a pencil beam [Fig.2.4. (b)] [14]-[15], [18]. In both scenarios, considering only the real part of the wave vector is enough for determining the emission angle, which can be computed as follows:

$$Cos(\theta) = \frac{\beta}{k_0} \tag{2.6}$$

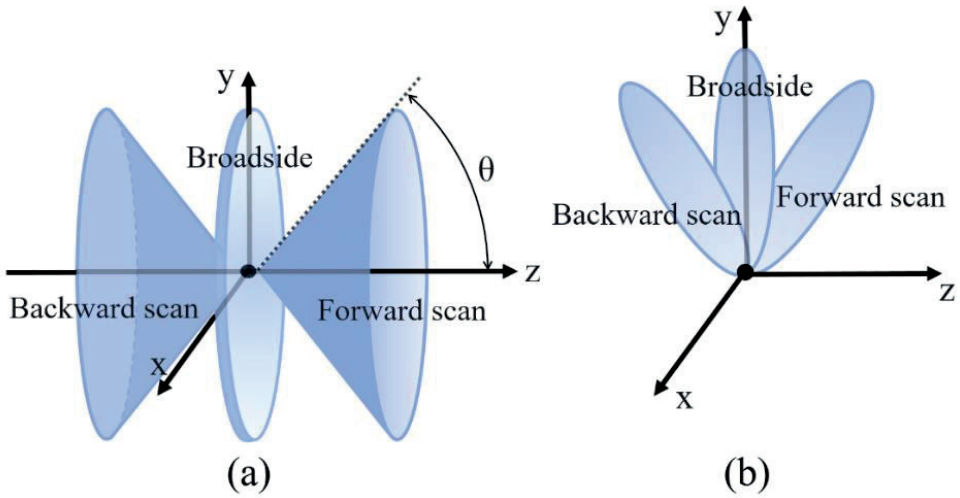


Figure 2.4. An illustration of the type of beam produced by LWAs that propagates the signal in z-direction. (a) Conical beam. (b) Pencil beam.

It's important to distinguish the two distinct approaches in travelling-wave antennas: ***dielectric-filled*** and ***air-filled*** [14]-[19]. Each of these approaches has its own characteristics and introduces different design considerations, giving rise to a wide spectrum of innovative designs. The former, where dielectric-filled transmission lines and dielectric-filled or partially dielectric-filled waveguides are used as the propagating medium generally result in slow wave structures. The latter, fully metallic designs that result in fast wave propagation structure. Air-filled LWAs are a good option for scanning applications where high-power handling capability, low loss, good stability, and reliability is required. On the other hand, dielectric-filled structures allow for miniaturized designs compared to air-filled structures. When dielectric-filled structures are based on planar technology (i.e. microstrip, SIW, coplanar, among other), designs allow fast and cheap prototyping, low metal losses and easier integration with PCBs. However, when the application requires high frequencies (for example mmW, sub-mmW, etc.), dielectric-filled structures require a very thin substrate, which can make designs challenging to implement due to the short wavelength [15]. Moreover, dielectric losses in dielectric-filled structures can lead designs to be unreliable for hard environments due to the dielectric loss tangent and dielectric constant is often a function not only of frequency, but also temperature, humidity, material quality, etc. Additionally, as frequency increases, dielectric losses

become higher compared to metal losses. This can be inferred from the equations that describe losses [20]-[21] in transmission lines and waveguides. The attenuation constant α can be decomposed into at least three components: one accounting for metal loss α_c, another for dielectric loss attributed to the loss tangent α_d, and another associated with radiation α_r. Omitting losses due the radiation, the metal losses α_c and dielectric losses α_d in microstrip transmission lines are given by:

$$\alpha_c = \frac{R_s}{WZ_0} \quad (Neper/m) \tag{2.7}$$

$$\alpha_d = \frac{\pi\sqrt{\varepsilon_r}\, tan\delta}{\lambda_0}\left(\frac{\varepsilon_{r_{eff}} - 1}{\varepsilon_r - 1}\right)\frac{\varepsilon_r}{\varepsilon_{r_{eff}}} \quad (Neper/m) \tag{2.8}$$

Where ε_{reff} is the effective relative permittivity of the dielectric material, ε_r is the relative permittivity, $tan(\delta)$ is the dielectric loss tangent, λ_0 is the wavelength in free space, Z_0 is the transmission line characteristic impedance, W is the line width, and R_S is the radio frequency (RF) sheet resistance (often called surface resistance or surface impedance) per unit length based on the physical dimensions of the structure. R_S is given by

$$R_s = \sqrt{\frac{\omega\mu_0}{2\sigma}} \quad (\Omega/m) \tag{2.9}$$

Where ω is the angular frequency, μ is vacuum magnetic permeability, and σ is the electric conductivity of the material. Below, metal losses α_c and dielectric losses α_d (in case of dielectric-filled waveguide) in rectangular waveguides for the mode TE_{10} are shown:

$$\alpha_d = \frac{k^2\, tan\delta}{2\beta_g} \quad (Neper/m) \tag{2.10}$$

$$\alpha_c = \frac{R_s(2b\pi^2 + a^3k^2)}{a^3b\beta_g k\eta} \quad (Neper/m) \tag{2.11}$$

Where β_g is the guided phase constant, a and b the width and the height of the waveguide respectively, η is the free space characteristic impedance. As can be

observed, in both cases, metal losses are proportional to $\sqrt{f}$. However, the dielectric losses increase proportional to the frequency in TEM/QuasiTEM transmission line and waveguides. Nevertheless, designs based on rectangular waveguides are typically air-filled, so the losses in the dielectric are 0.

The choice between dielectric-filled and air-filled structures will vary depending on the requirements of the application.

In uniform LWAs the guiding structure is uniform along its length and supports a fast wave with respect to free space. Furthermore, exists the possibility of introducing a taper along its length in order to achieve non-uniform current or aperture distribution. The use of non-uniform current distributions (i.e. Taylor distribution, cosine distribution, among others) can lead to lower levels of secondary lobes at the expense of increasing the width of the main beam or reducing the antenna's gain [17]. The radiation patterns achieved in these structures can vary significantly based on the source's placement (according to figure 2.3). In the first configuration, the antenna is fed at one end ($z = 0$), often with an absorber or matched load at the other end ($z = L$) for residual power absorption. In this case the phase constant is within the range $0 < \beta < k_0$. For such a uniform leaky-wave antenna fed at one end (and therefore supporting a wave propagating in a single direction on the guiding structure) it is difficult to obtain a beam exactly at broadside, since this corresponds to the cutoff frequency in the case of TE/TM structures and $f = 0$ in the case of TEM/QuasiTEM structures. In the second scenario, the structure is center-fed ($z = 0$), with matched loads at both ends ($z = \pm L/2$) to absorb remaining power. In this case, a bidirectional radiation pattern with angle $\pm\theta$ is generated in azimuth that can give rise to a relatively wide broadside beam when both main lobes steers to $\theta = \pm 90°$. The broadside direction coincides with the cutoff frequency; however, in this configuration the two generated lobes merge, resulting in a single broader broadside lobe compared to the two beams separately.

A slitted waveguide is a well-known uniform LWA typically based on a rectangular waveguide that has a narrow slot or slit cut along its length [13] - [14], [16] – [17]. The radiation properties of a slitted waveguide can be controlled by adjusting the width, length, and position of the slot. The value of α can be either large or small, dependent on the rate of leakage per unit length. The magnitude of α significantly influences the beam characteristics of the radiated wave. A larger α, indicating a higher rate of leakage, results in a shorter effective aperture and consequently a broader beamwidth. For instance, Figures 2.5 and

2.6 depict a slotted rectangular waveguide based on the WG14 standard. In the first design (Fig.2.5), the source was located at one end of the structure, and in the second device (Fig.2.6) the source was located at the center of the structure. The radiation pattern was obtained using CST Studio Suite 2014 software. The device was simulated under perfect matching conditions using waveguide ports. The dispersion diagram was inferred from the constant phase of the guided signal described by [20] - [21]:

$$\beta_g = \sqrt{k^2 - {k_c}^2} \tag{2.12}$$

Where k_c is the cutoff wavenumber.

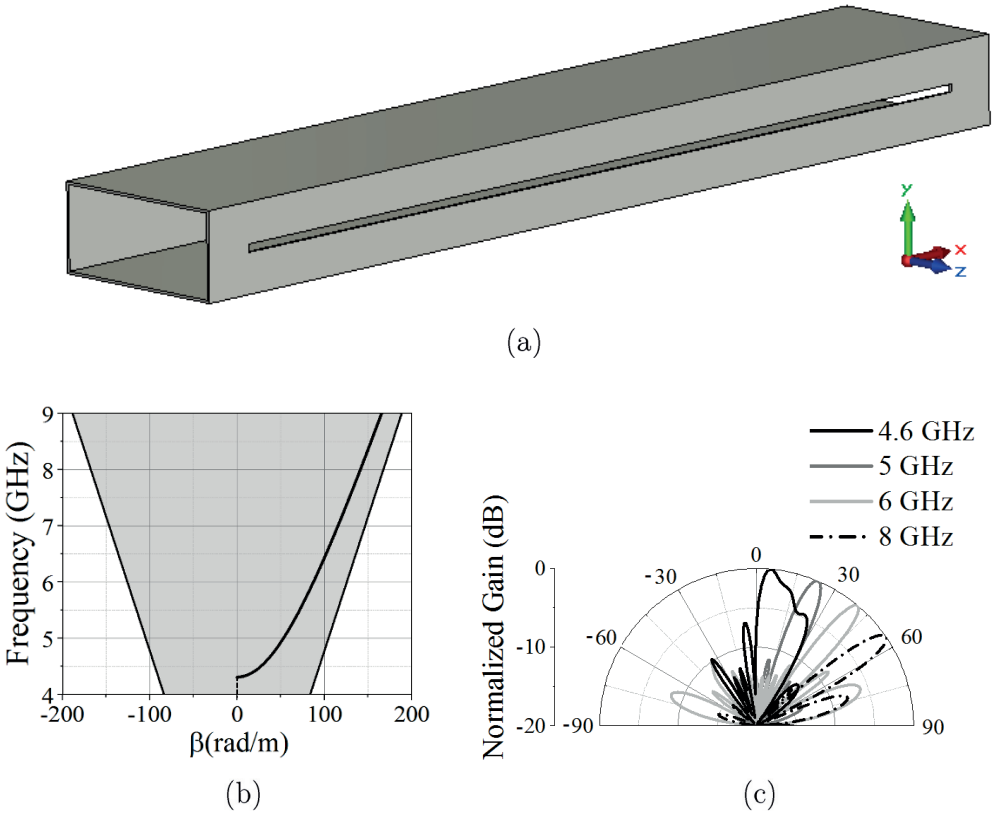


Figure 2.5. (a) End-fed slitted rectangular waveguide using standard WG14 (WR137) load with a slit (1x400 mm) in the center of the narrow wall under perfect matching condition. (b) Dispersion diagram. (c) Radiation pattern.

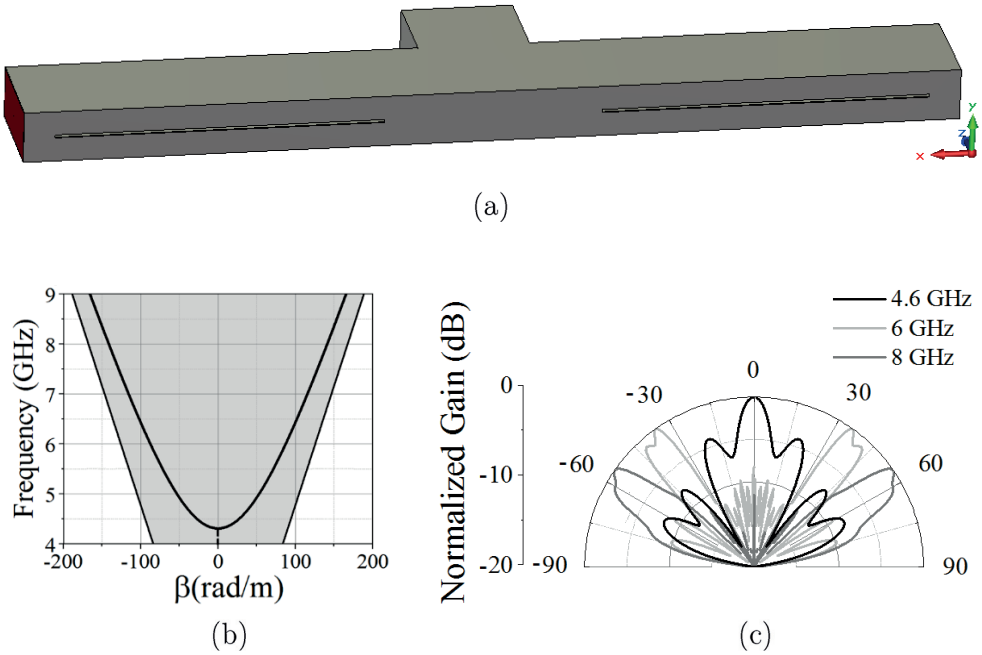


Figure 2.6. (a) Center-fed (be means of a T-junction) slitted rectangular waveguide using standard WG14 (WR137) load with a slit (1x500 mm) in the center of the narrow wall under perfect matching condition. (b) Dispersion diagram. (c) Radiation pattern.

In the first case (Fig. 2.5), it is observed that the radiation pattern is unidirectional but limited to the first quadrant, while in the second configuration, two main lobes are generated, enabling scanning in both quadrants. Additionally, it is noted how a broadside pattern is achieved with the second configuration.

Quasi-uniform LWAs operate in a similar way as uniform LWAs, except that a periodic guiding structure with a period $d << \lambda$ is used. Nevertheless, the periodicity plays no direct role in the radiation. As before, this results in a complex propagation wave number, with β and α determining beamwidth and radiation efficiency, similar to uniform leaky-wave antennas. The periodic modulation remains uniform along the structure's length, except if small taper of the periodic element along the length are used to control the sidelobes. For instance, figure 2.7 shows a rectangular waveguide loaded with transversal slots in the wide wall.

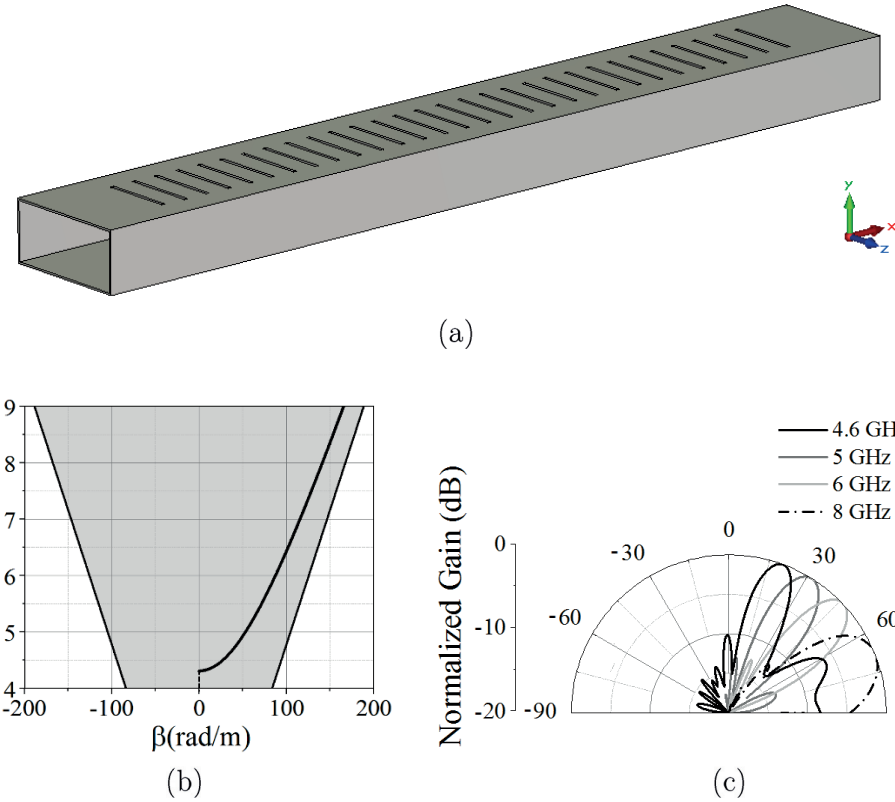
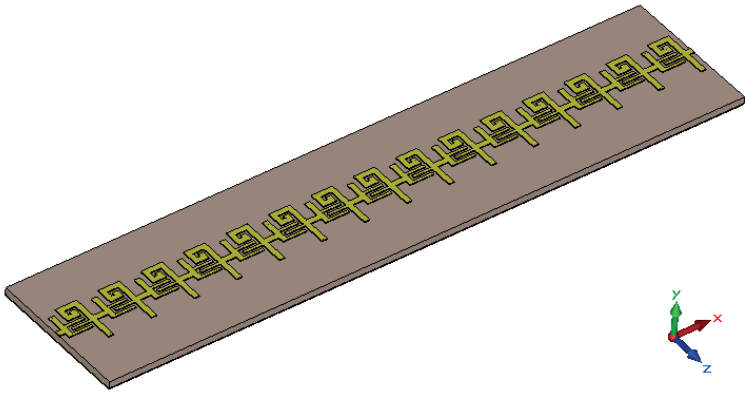


Figure 2.7. (a) End-fed rectangular waveguide using standard WG14 (WR137) load with 30 transversal slots (1x20 mm) in the wide wall and distanced 7 mm under perfect matching condition. (b) Dispersion diagram. (c) Radiation pattern.

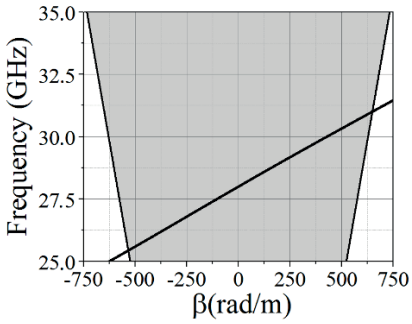
The radiation pattern was simulated using CST Studio Suite 2014 software and the dispersion diagram was inferred from (2.12). In the same way as uniform structures, this antenna is unidirectional and limited to the first quadrant. Additionally, a bi-directional configuration can be achieved by placing the source in the center of the structure, following the same approach as the uniform structure.

When metamaterials were proposed, the capability to obtain a backward to forward unidirectional beam steer with Quasi-Uniform LWAs based on Composite Right/Left-Handed (CRLH) became a possibility. Metamaterials are artificial structures capable of achieving specific electromagnetic properties not commonly found in natural materials [22]-[24]. CRLH metamaterials integrate LH (Left-Handed) structures, showcasing a negative index-material marked by simultaneous negative permittivity ε and permeability μ, alongside RH (Right-Handed) structures that exhibit attributes commonly observed in natural

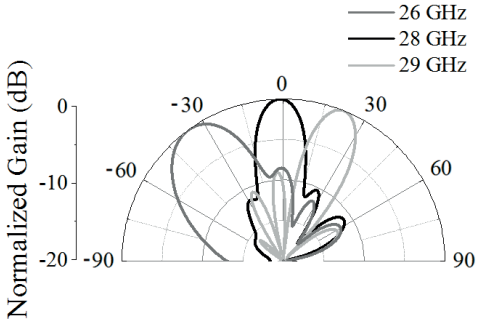
materials. LWAs based on CRLH structures are composed by unit cells with a length $d << \lambda$ that behave as a homogeneous effective medium. In figure 2.8 a LWA based on CRLH structure is shown [25]. The dispersion diagram was obtained from electromagnetic simulation of the unit cell under perfect matching condition.



(a)



(b)



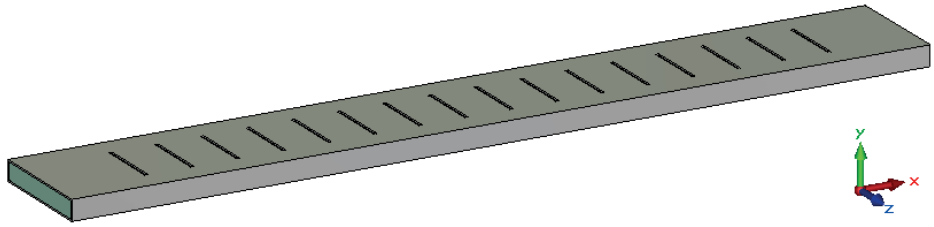
(c)

Figure 2.8. (a) End-fed CRLH metamaterial LWA composed by 15-unit cells according to [25] under perfect matching conditions. (b) Dispersion diagram. (c) Radiation pattern.

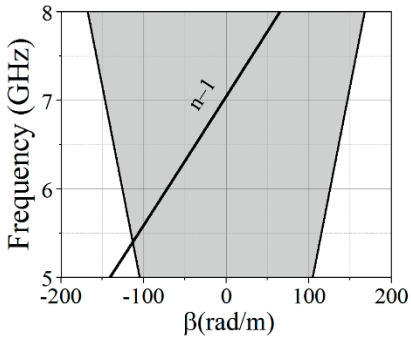
In contrast to previous designs, these structures, when the unit cell is in balanced condition the antenna provides unidirectional scanning from backward to forward with feeding at one end.

In periodic LWAs the guiding structure exhibits a periodic perturbation along its length. Normally, periodic LWAs are designed dielectric filled, supporting a wave that is slow with respect to free space. The periodic element generates the appearance of the infinite space harmonics, some of which are fast and can radiate. Periodic leaky-wave antennas are commonly designed to

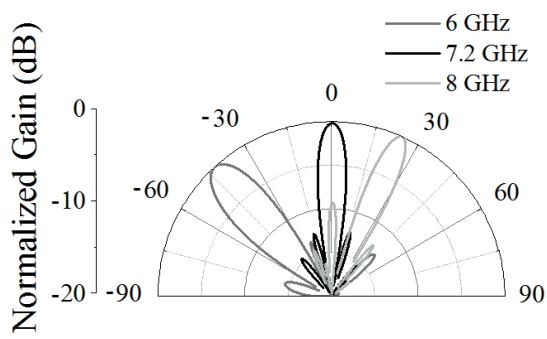
radiate with the n = −1 space harmonic. This type of antennas offers the capability to scan in frequency from backward to forward, through broadside, by feeding the antenna from one end. Similarly, following the approach of the previous cases, this configuration can also be fed from the center, resulting in bidirectional scanning. In figure 2.9. a rectangular dielectric-filled waveguide with transversal slots is shown. The dispersion diagram was inferred from equation (2.4) considering the phase constant of the space harmonic $n-1$.



(a)



(b)



(c)

Figure 2.9. (a) End-fed dielectric-filled (RO Rogers 3010, 50 mils, $\varepsilon_r = 10.2$) rectangular waveguide (34.8x5.2 mm) load with 16 transversal slots (20x1 mm) in the wide wall and distanced 14 mm under perfect matching condition. (b) Dispersion diagram. (c) Radiation pattern.

Similar to CRLH-based LWA, this type of structure allows single-beam scanning from backward to forward, feeding the antenna at one end. However, in periodic structures, the main beam and radiation efficiency degrade when approaching broadside due to a well-known phenomenon, Open StopBand (OSB) [13] - [19], [26]. There exist techniques to deal with this problem in periodic LWAs, which will be shown later. On the other hand, although OSB

degrades periodic LWA performance, this behavior is used in Electromagnetic Bandgap (EBG) structures to design filters, gratings, frequency-selective surfaces (FSS), photonic crystals, photonic band gaps (PBG), and so on [27] - [29]. The appearance of the open stopband in periodic structures is associated with a significant amount of power from the wave traveling along the structure being reflected back to the source, rather than radiated, producing a large mismatch. Since the proposed LWA designs in this thesis are based on periodic structures, the OSB phenomenon in LWAs will be further discussed in Chapter 4.

2.2.2 Applications, Market Scope, and State of the Art

LWAs have been the subject of extensive research and development, due to their frequency scanning capability, high directivity, and straightforward feeding network. These attributes make LWAs highly versatile across a wide range of applications. Some of the key application areas where LWAs play an indispensable role encompass [30]-[34]:

- ***Radar systems:*** LWAs find a pivotal role in radar systems for angle scanning and beamforming. Their capability to alter radiation angles without physical movement of the antenna proves advantageous in surveillance and tracking systems. This includes applications such as airborne early warning and control systems (AEW&C) in military settings, efficient control of airports and seaports, and velocity radar systems for vehicles.
- ***Security Systems:*** They are applied in security systems, including motion detection and vehicle scanning systems, where the ability to explore specific areas is essential.
- ***Imaging and Sensing applications:*** LWAs are effectively employed in microwave imaging systems, such as Synthetic Aperture Radars (SAR), terrestrial and space-based imaging systems. Additionally, in medical imaging contexts like magnetic resonance imaging (MRI) and computed tomography (CT), they have the capability to improve image quality by precisely concentrating radiation on specific areas of the body.
- ***Communications systems:*** In the domain of communications, these antennas can be harnessed for point-to-point and point-to-multipoint links. Their capability to adjust the radiation direction is valuable for directional signal transmission and interference suppression.

- ***Object Tracking:*** LWAs are utilized in object tracking systems, such as satellite tracking and global positioning systems (GPS), to track moving objects and adjust the direction of signal reception.
- ***Satellite communication:*** LWAs can track the positions of moving satellites without requiring physical antenna movement, ensuring constant and high-quality connectivity. Moreover, their low profile and electronic beam scanning capability make them a valuable choice for ground stations that need to communicate with multiple satellites in different orbits.
- ***Obstacle Detection Systems:*** They are applied in autonomous vehicles and obstacle detection systems to provide information about the distance and direction of nearby objects.

Various innovative LWA designs have been proposed in the past years. Regarding the LWAs, in [36] a novel antenna design is proposed, featuring a longitudinal slot in the center of the top wall of a ferrite-filled rectangular waveguide. Excited by the TE_{10} mode of a transversely magnetized ferrite waveguide, this antenna exhibits anti-symmetric surface current density, enabling it to scan its radiation beam direction by adjusting the bias magnetic field. The antenna offers several advantages over previous designs, such as ease of fabrication and reduced sidelobe levels. In [37] the work focuses on addressing the challenges associated with the slot-mode in a slitted waveguide, which has implications for high-power frequency beam scanning applications, particularly in the field of radar technology. The study presents two distinct structures as solutions. The first design successfully suppresses the slot-mode propagation and radiation over a substantial bandwidth, with its leaky wavenumber matching simulation predictions. The second design achieves complete suppression of the slot-mode radiation across the entire X-band, though it does not allow for the extraction of the wavenumber associated with the perturbed TE_{10} mode. Related with the unwanted slot-modes, in [38] a modified design for a substrate integrated waveguide (SIW) long slot leaky-wave antenna (LWA) is presented. The unwanted mode is identified using the amplitude and phase of the electric field at the slot. The authors introduce periodic transverse slots on one side of the uniform longitudinal slot to suppress the unwanted mode, resulting in a more accurate radiation pattern.

Focusing on the quasi-uniform approach, in [39] a leaky wave antenna based on an air-filled rectangular waveguide is presented. In this design, the radiation

occurs through transverse slots on the broad wall of the waveguide. A systematic design method is employed, based on thinned array theory, to achieve a low side-lobe level (SLL). It scans a portion of the forward quadrant with low SLL and high gain over the frequency band of 9.8-10.2 GHz. In the state of the art also some analytical studies for designing LWAs are presented. In [40] an analytical approach for designing quasi-uniform LWAs (QULWA) with very low sidelobe levels is introduced. The method leads to a general closed formula that can be used by antenna designers. It involves estimating the distribution of the electric field intensity in the QULWA slots through simulation, fitting a mathematical function to the simulation results, and using Floquet's theorem to derive a closed-form formula for designing QULWAs. Within quasi-uniform designs, LWAs based on metamaterials can also be encountered. In this context, LWA based on metamaterials, in conjunction with periodic structures, represent the two prominent categories that have garnered considerable attention in recent research [1]-[3], [15], [18], [25], [41]-[45] owing to their capabilities. In [41], a wideband compact frequency beam scanning LWA based on composite right-handed and left-handed unit cells is proposed for 5G millimeter-wave applications (Fig.2.8). This innovative unit-cell-based antenna design enables nearly linear frequency scanning within the frequency range of 24.0 GHz to 32.0 GHz while maintaining a uniform gain of approximately 8 dBi. In [41] is introduced a Composite Right/Left-Handed Slot Line Leaky-Wave Antenna (LWA) loaded with non-bianisotropic split ring resonators (NB-SRRs) and is compared with a Coplanar Waveguide (CPW) approach. This antenna demonstrates backward, broadside, and forward radiation from its fundamental mode, eliminating the far field cancelation issue associated with open planar waveguides. It operates in the left-handed and right-handed bands at 3 GHz, providing nearly constant gain across broadside radiation.

Finally, within the domain of periodic leaky-wave antennas, innovative solutions, especially those dealing with the open stopband phenomenon, can be found. In [42], a novel method is presented for achieving comprehensive open stopband suppression in dielectric-filled periodic LWAs by employing two non-identical elements within each unit cell. Similarly, in [43], the authors introduc a compact fully metallic millimeter-wave (MMW) periodic LWA based on corrugated parallel-plate waveguides loaded with non-identical transverse slots.

The design includes both a smooth plate and a corrugated plate that integrates corrugations for slow-wave transmission and radiating slots. The incorporation of two different elements within one radiating unit improves the open stopband effect and enables broadside scanning. The prototype achieves scanning beams with an angular range of 48° and peak gains between 11.9 and 16.0 dBi in the frequency range of 28 to 40 GHz, with a radiation efficiency exceeding 85%. In [44], a novel approach is proposed to control the scan rate of frequency-scanned antennas for bandwidth-limited applications with open stopband suppression. They discuss two techniques: optimizing unit cell dispersion and meandering unit cells with a specific periodicity. Another topic discussed within LWAs is the current distribution to achieve radiation patterns with fewer secondary lobes, primarily for radar and tracking applications. In this context, in [45] a ridge serpentine waveguide-based antenna loaded with inclined radiating slots in its narrow wall is shown. By adjusting the aperture distribution, this design achieves low SSL. However, this structure is affected by the open stopband phenomenon.

2.3 Electromagnetic field confinement device

Antennas have long been widely studied and used in the realm of electromagnetic communication systems. Their versatile functionality has enabled a myriad of applications, ranging from wireless information transfer to imaging, sensing, radar and object tracking, remote control, among others. With their capacity to operate efficiently across diverse frequency ranges and adapt to various scenarios [1]-[3], [13]-[21], [30]-[47].

Nevertheless, the traditional antenna designs that excel in long-range communication encounters unique challenges when applied to near-field scenarios. Efficient control of electromagnetic field distribution in space is essential across numerous applications where is required a precise electromagnetic interaction within specific regions between the transmitting device and the receiving entity (including samples, actuators, transponders, or sensors). The challenge lies in establishing well-defined, large bounded illumination regions with strong and robust field levels, particularly when these regions approach the wavelength dimensions.

Traditional methods of electromagnetic field distribution control face hurdles, particularly dealing with energy leakage in the form of radiation when the dimensions of the confined region are comparable to the wavelength [48].

2.3.1 Applications, Market Scope, and State of the Art

Various authors have worked in innovative solutions to address these issues, such as considering evanescent wave coupling. An evanescent wave is a type of electromagnetic wave that take place near an interface or surface between two media with different refractive indices, such as the boundary between air and a dielectric material. The field intensity of evanescent modes decreases exponentially with distance, ensuring minimal radiation. Some examples of applications involving evanescent modes are optical fiber coupling for biosensor applications [49], total internal reflection fluorescence microscope for medical applications in molecular measurements and therapeutic drug monitoring [50]-[53], ultrafast fiber laser [54]-[55], excitation of surface plasmon polaritons for information transmission in microprocessors, computer chips and high-resolution technologies (e.g., lithography) [56]-[59], integrated high power millimeter-wave switching for wireless backhaul in 5G and 6G communication networks [60]-[61], among others. However, this method have a limited performance because the confinement of these waves relies on the materials used for the coupler and the surrounding medium, which can lead to limited control over the field's decay as it extends over a distance. Furthermore, the fields exhibit strong confinement to the surface, constraining the maximum range over which enough electromagnetic field can be localized. This has a direct impact on the device's performance because, while some applications require extremely confined fields such as in microscopy or biosensors, other applications require high illumination distance as in Radio Frequency Identification (RFID) readers and must comply with regulations and standards like International Commission on Non-Ionizing Radiation Protection [ICNIRP] or EPC Gen2 RFID communication protocol [62]-[63].

Within the RFID systems, certain scenarios demand the ability to establish a detection region that is both controllable to prevent undesired detections and sufficiently extensive to cover the required detection area. These scenarios include points of sale at shops and stores in desktop readers [64]-[65], printer encoders [66]-[67], smart shelves [68]-[69], and smart point readers [70]-[71].

However, achieving an adequate illumination area with minimal radiation leakage beyond it presents a significant challenge. To address these difficulties, inductive coupling based on loop antennas has been used in the UHF band [62], [72]. Loop antennas with a perimeter much less than their operating wavelength generate a strong and uniform magnetic field distribution in proximity to the antenna surface. However, these structures achieve only a few centimeters of communication, which may be insufficient for some applications. Moreover, inductive and capacitive coupling system performance can be affected by the presence of surrounding media, which may compromise tag readability and reduce the read range [73]. Other designs, such as reconfigurable reader antennas (Modular Antennas) [74], have been proposed. These antennas make readers more flexible for specific operative scenarios, allowing for shaping of the interrogation field in the antenna NF region when the control of the reader output power is insufficient to guarantee high successful reading percentages on the illumination region/volume. Other structures, such as electrically large loop antennas [75] and meandered lines [76]-[77], have also been proposed. However, these configurations produce some radiation leakage in the far-field region and do not allow for theoretical predictions of the electromagnetic field decay from the device surface.

In 2016, the research group conducting this thesis proposed a novel design methodology to control field decay in the broadside direction without radiation leakage, publishing the results in the scientific journal "Scientific Reports" [48]. The paper introduces an electromagnetic field confinement device (EMFCD) based on a one-dimensional metamaterial guiding structure capable of propagating a surface wave mode. An EMFCD is based on a traveling wave structure that enables the imposition of a field decay factor on the generated evanescent wave around the structure. EMFCD devices hold the potential to bring significant advancements to various applications, including medical imaging, wireless power transfer, and near-field communication, such as RFID.

This thesis aims to make a substantial contribution to the exploration of different aspects of EMFC devices. The proposed methodology will be applied and adapted to various traveling wave structures, including rectangular waveguides and Substrate Integrated Waveguides (SIW).

2.3.2 Principle of operation of EMFCD

The operation and design methodology of electromagnetic field confinement devices is based on analysis of the propagated wave in a traveling wave structure featuring one or multiple apertures that interact with the surrounding medium. Depending on the configuration of the travelling wave structure, it is possible to either radiate a signal (as observed in the previous subsection) or create an evanescent mode on the surface, or even both, but in different frequency ranges. Evanescent waves rapidly decrease in amplitude as they move away from the interface and eventually vanish. These waves are confined close to the surface and do not carry significant energy far from it. In this context, the performance of the electromagnetic field confinement device will be contingent on the technology used (coplanar, waveguide, microstrip, etc.) as well as the geometry (periodic, uniform, etc.). However, the principle of operation will remain the same for all structures.

When a wave propagates from one medium to another with different properties (such as refractive index in the case of optics), the tangential component of the wave vector $\vec{k}$ must remain continuous at the interface between the two media. This means that the wave's propagation direction does not change abruptly at the interface but remains constant. According to the separability condition of the wave equation (illustrated in figure 2.10), the wave vector can be decomposed into rectangular coordinates as follows

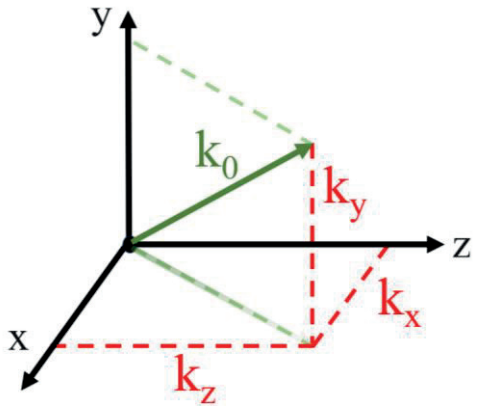


Figure 2.10. Decomposed wave vector in rectangular coordinates.

$$k_x^2 + k_y^2 + k_z^2 = k_0^2 \tag{2.13}$$

where each wave vector is composed of β_i and $j\alpha_i$ that corresponds to the

constant phase and the attenuation constant along *i*-axis respectively. Assuming that the propagating wave in the travelling wave structure has no variation along the z-axis ($kz = 0$) and propagates along the *x*-axis, in order to ensure continuity of the tangential components of the wave vector, k_x must be consistent with the wave vector inside the structure. Consequently, the wave vector in *y*-axis from the surface of the structure in the surrounding medium is described by

$$k_y = \pm\sqrt{{k_0}^2 - (\beta - j\alpha)^2} \tag{2.14}$$

Equation (2.14) leads into two different modes of operation for the wave that propagates within the structure. These modes are known as the radiative wave mode and the surface wave mode [48]. The radiative mode [figure 2.11 (a)] occurs when complex values of k_y are obtained. Under this situation the structure gradually leaks out a small amount of energy in form of coherent radiation, which implies an attenuation of the guided signal quantified by the parameter α. In this mode, considering only the real part of the wave vector is enough for estimating the emission angle of maximum radiation intensity (see eq. 2.5).

On the other hand, the surface wave mode [figure 2.11 (b)] consists of a wave that propagates along the direction of the guiding device (*x*-direction) while decays vertically in broadside direction (*y*-direction). In this mode, the phase constant β_y equals zero ($\beta_y = 0$) and de wave vector in y-direction k_y is determined only by $-j\alpha_y$. Due to the absence of radiation, assuming that losses in the guiding structure are negligible ($\alpha = 0$), the signal is propagated through the travelling-wave structure without attenuation. For the surface wave mode, equation (2.13) becomes:

$$k_y = \pm\sqrt{{k_0}^2 - \beta^2} \tag{2.15}$$

By employing the general solution for the propagation of plane waves in free space and appropriately adjusting the value of β to achieve purely imaginary values of k_y, the total field in the surrounding medium and the decay constant in the broadside direction can be expressed as follows:

$$A_i(x,y,t) = A_i e^{-j\beta x} A_i e^{-j\alpha_y \cdot y} e^{j\omega t} \tag{2.16}$$

$$\alpha_y = \sqrt{\beta^2 - {k_0}^2} \tag{2.17}$$

where A_i represents any component of the total electromagnetic field propagating within the surrounding medium. From equation 2.16, it can be inferred that the decay of the fields will be considered exponential in the y-direction. Moreover, the attenuation constant α_y can be designed through the phase constant of the guided mode. The ability to control the effective phase constant of the guided mode will depend on the characteristics of the device, including its technology, geometry, feeding system, among others.

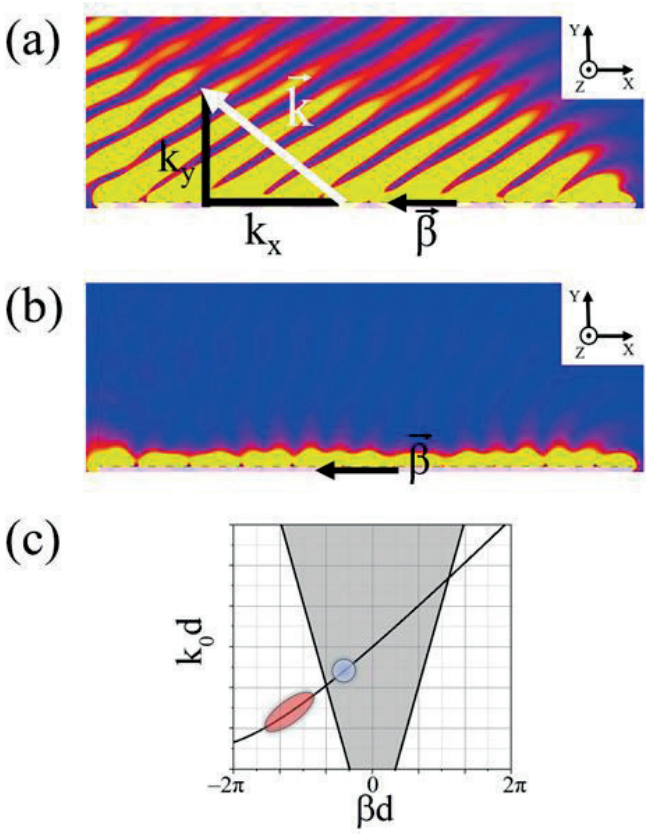


Figure 2.11. Field distribution around the travelling-wave structure. (a) Radiative mode operation. (b) evanescent mode operation. (c) Dispersion diagram (red marker corresponds to evanescent mode and blue marker corresponds to backward radiation).

A critical consideration in the design of electromagnetic field confinement devices is the field distribution. The prediction of exponential attenuation will be valid as long as the electric field distribution exhibits reasonably consistent linear dependence along the y-direction within the symmetry plane of the structure. However, if the field distribution reveals cylindrical dependence, the decay of the field will be described proportionally to

$$A_i(y) = A_i H_1^{(1)}(j\alpha y) \tag{2.18}$$

where $H_1^{(1)}(\mathrm{x})$ is the Hankel function of first kind, order 1 and argument x. In a practical scenario, diverse field distributions can be observed when examining a slot line on a dielectric substrate under various boundary conditions, as depicted in figure 2.12. As it can be appreciated in Fig. 2.12 (a) the field distribution in a slot line loaded with dielectric material, demonstrates elliptical behavior [94]. Under this condition, the electric field decay in y-axis can be approximated with an exponential dependence in the center of the structure. However, when considering distance y larger than the width of the slot s, it can be modeled as a line source of magnetic current, resulting in an evanescent wave with cylindrical symmetry, which is proportional to (2.18). Nevertheless, if two conducting plates are added at the ends of the structure, or equivalently, two electric walls, or a bidirectional arrangement of the structure, the electric fields will change their helical behavior to a flat dependence as the field moves away from the surface. Under such condition, the electric field will decay according to [2.16]. This phenomenon underscores the importance of the analysis of the field distribution of structure in order to correctly design the field decay.

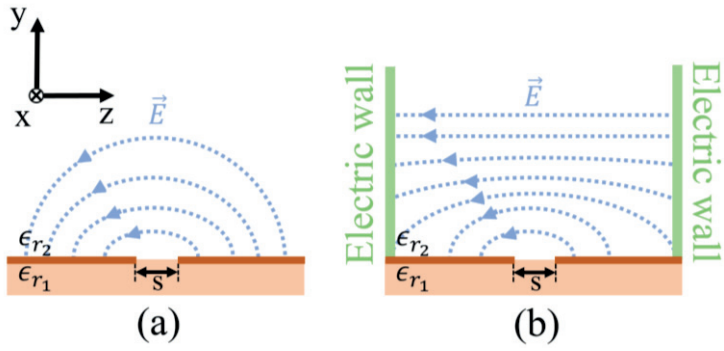


Figure 2.12. a) Electric field of a slot line on a dielectric substrate. b) Electric field of a slot line on a dielectric substrate with electric walls in the metal edges.

In summary, EMFCDs leverages the functionality of a wave-traveling structure, using the separability condition of the wave equation, the phase constant of the propagating wave within the structure and the field distribution to achieve precise control over electromagnetic field attenuation from the surface of the device. The key characteristics of EMFCD can be outlined as follows:

- ***Bandwidth:*** Refers to the range of frequencies within which the device can efficiently operate while maintaining its confinement properties.
- ***Insertion Losses:*** Quantify the signal's attenuation when it passes through the device. Minimizing these losses is sought to ensure that most of the signal can be confined and transmitted with minimal degradation. Typically indicated in dB or dB/cm.
- ***Radiation pattern:*** Radiation Pattern: Describes how the device emits or transmits the electromagnetic field. The goal is to achieve a controlled radiation pattern indicating a lack of gain, preferably below -10 dB, to achieve effective confinement.
- ***Attenuation constant (α):*** Represents how the electromagnetic field attenuates from the surface of the device in a direction. Expressed in dB/cm.
- ***Characteristic distance (d_α):*** Defined as $1/\alpha$, determines the maximum distance from the device where the field will be present. $5d_\alpha$ corresponds to an attenuation of 99% with respect to the field at the surface of the device.
- ***Linearity:*** Refers to the consistency of the attenuation constant with respect to frequency.
- ***Field distribution:*** Describes how the electromagnetic field is distributed across the device's surface. The aim is to achieve a distribution that avoids or minimizes spurious radiation and enables effective confinement along the device.

REFERENCES

[1] A. A. Oliner, "*1963 Short Course on Microwave Field and Network Techniques*" Brooklyn, Polytechnic Institute of Brooklyn, Tuesday, June 4, 1963.

[2] X. W. Dai, C. Ding, W. Yu, L. Liu and G. Q. Luo, "Ultrawide-Angle and Compact Leaky-Wave Antenna Based on Complex Periodic Structure," in IEEE Antennas and Wireless Propagation Letters, vol. 22, no. 6, pp. 1486-1490, June 2023, doi: 10.1109/LAWP.2023.3247435.

[3] G. Zamora, S. Zuffanelli, F. Paredes, F. J. Herraiz-Martínez, F. Martín and J. Bonache, "Fundamental-Mode Leaky-Wave Antenna (LWA) Using Slotline and Split-Ring-Resonator (SRR)-Based Metamaterials," in IEEE Antennas and Wireless Propagation Letters, vol. 12, pp. 1424-1427, 2013, doi: 10.1109/LAWP.2013.2287525.

[4] M. Nitas, C. S. Antonopoulos and T. V. Yioultsis, "E-B Eigenmode Formulation for the Analysis of Lossy and Evanescent Modes in Periodic Structures and Metamaterials," in IEEE Transactions on Magnetics, vol. 53, no. 6, pp. 1-4, June 2017, Art no. 9401004, doi: 10.1109/TMAG.2017.2683459.

[5] P. Aguilà, G. Zamora, F. Paredes, F. Martín and J. Bonache, "Planar fan-beam reflective array antenna based on non-bianisotropic complementary split-ring resonators (NB-CSRRs)," 2017 IEEE International Symposium on Antennas and Propagation & USNC/URSI National Radio Science Meeting, San Diego, CA, USA, 2017, pp. 1263-1264, doi: 10.1109/APUSNCURSINRSM.2017.8072674.

[6] Y. Tsuji, Y. Morita and K. Hirayama, "Photonic Crystal Waveguide Based on 2-D Photonic Crystal With Absolute Photonic Band Gap," in IEEE Photonics Technology Letters, vol. 18, no. 22, pp. 2410-2412, Nov.15, 2006, doi: 10.1109/LPT.2006.885295.

[7] C. Rockstuhl and F. Lederer, "Intrinsic Surface and Bulk Defect Modes in Quasi-Periodic Photonic Crystals," in Journal of Lightwave Technology, vol. 25, no. 9, pp. 2299-2305, Sept. 2007, doi: 10.1109/JLT.2007.901439.

[8] Y. S. Dadoenkova, N. N. Dadoenkova, I. L. Lyubchanskii, J. W. Kłos and M. Krawczyk, "Faraday Effect in Bi-Periodic Photonic-Magnonic Crystals," in IEEE Transactions on Magnetics, vol. 53, no. 11, pp. 1-5, Nov. 2017, Art no. 2501005, doi: 10.1109/TMAG.2017.2712278.

[9] T. Zhu, Y. Song, Y. Rao and Y. Zhu, "Highly Sensitive Optical Refractometer Based on Edge-Written Ultra-Long-Period Fiber Grating Formed by Periodic Grooves," in IEEE Sensors Journal, vol. 9, no. 6, pp. 678-681, June 2009, doi: 10.1109/JSEN.2009.2021187.

[10] Hojoong Jung, Yong Gon Seo, Woosung Ha, S. H. Park and Kyunghwan Oh, "New type of long-period fiber grating by self-assembled periodic polymerization in silica hollow optical fiber," 2009 Conference on Optical Fiber Communication, San Diego, CA, USA, 2009, pp. 1-3.

[11] A. M. Vengsarkar, P. J. Lemaire, J. B. Judkins, V. Bhatia, T. Erdogan and J. E. Sipe, "Long-period fiber gratings as band-rejection filters," in Journal of Lightwave Technology, vol. 14, no. 1, pp. 58-65, Jan. 1996, doi: 10.1109/50.476137.

[12] W. W. Hansen, Radiating electromagnetic waveguide, U.S., Patent 2.402.622, 1940.

[13] D. R. Jackson, C. Caloz and T. Itoh, "Leaky-Wave Antennas," in Proceedings of the IEEE, vol. 100, no. 7, pp. 2194-2206, July 2012, doi: 10.1109/JPROC.2012.2187410.

[14] C. A. Balanis, Modern Antenna Handbook, Hoboken, NJ, USA:Wiley, 2008.

[15] K. Sarabandi, A. Jam, M. Vahidpour, and J. East, "A Novel Frequency Beam-Steering Antenna Array for Submillimeter-Wave Applications," in IEEE Transactions on Terahertz Science and Technology, vol. 8, no. 6, pp. 654-665, Nov. 2018, doi: 10.1109/TTHZ.2018.2866019.

[16] Richard C. Johnson, Antenna Engineering Handbook, third edition, USA, NY, New York:McGraw-Hill, 2007.

[17] J. L. Volakis, Antenna Engineering Handbook, USA, NY, New York:McGraw-Hill, 2007.

[18] A. Ohadi and G. V. Eleftheriades, "Slotted Waveguide Frequency-Scanned Slow-Wave Antenna With Reduced Sensitivity of the Closed Stopband at Millimeter-Wave Frequencies," in IEEE Access, vol. 10, pp. 27783-27793, 2022, doi: 10.1109/ACCESS.2022.3152905.

[19] C. A. Balanis, *"Antenna Theory: Analysis and Design"*, fourth edition, Hoboken, NJ, USA:Wiley, 2016

[20] Robert E. Collin, "Foundations for Microwave Engineering", second edition, USA, New Jersey, IEEE Press, 2000

[21] David M. Pozar, "Microwave Engineering", fourth edition, Hoboken, NJ, USA:John Wiley & Sons Inc, 2011.

[22] Ricardo Marques, Ferran Martin, Mario Sorolla, "Metamaterials with Negative Parameters: Theory, Design and Microwave Applications", John Wiley & Sons, 2007.

[23] Tie Jun Cui, David R. Smith, Ruopeng Liu, "Metamaterials: Theory, Design, and Applications", Springer, 2010.

[24] Filippo Capolino, "Applications of Metamaterials (Metamaterials Handbook)", CRC Press, 2009.

[25] W. Shuping, N. Nasimuddin and A. Alphones, "Wideband Linear Frequency Scanning Antenna for 5G Millimeter Wave Applications," 2021 IEEE Asia-Pacific Microwave Conference (APMC), Brisbane, Australia, 2021, pp. 19-21, doi: 10.1109/APMC52720.2021.9661871.

[26] Warren L. Stutzman, Gary A. Thiele, "Antenna Theory and Design" third edition, Hoboken, NJ, USA:Wiley, 2012.

[27] Yang, F., & Rahmat-Samii, Y. (2008). Electromagnetic Band Gap Structures in Antenna Engineering (The Cambridge RF and Microwave Engineering Series). Cambridge: Cambridge University Press. doi:10.1017/CBO9780511754531

[28] B. Munk, "Frequency Selective Surfaces: Theory and Design", John Wiley & Sons, 2000

[29] Kurt Busch, Stefan Lölkes, Ralf B. Wehrspohn, Helmut Föll, "Photonic Crystals: Advances in Design, Fabrication, and Characterization", Wiley-VCH, 2004.

[30] Dennis Roddy, *'Satellite Communications'*, third edition, , New York, NY, USA:McGraw-Hill, 2001.

[31] Yang, S.T. and Ling, H., 2017. Application of compressive sensing to two-dimensional radar imaging using a frequency-scanned microstrip leaky wave antenna. Journal of electromagnetic engineering and science, 17(3), pp.113-119.

[32] Hafiz Suliman Munawar, " Applications of Leaky-wave Antennas: A Review ", International Journal of Wireless and Microwave Technologies(IJWMT), Vol.10, No.3, pp. 56-62, 2020.DOI:10.5815/ijwmt.2020.03.05.

[33] Rabbani, M.S., Churm, J. and Feresidis, A., 2018. Millimetre-wave beam steerable leaky-wave antenna for 5G systems.

[34] Karmokar, D.K. and Guo, Y.J., 2017, September. Planar leaky-wave antennas for low-cost radar. In 2017 IEEE-APS Topical Conference on Antennas and Propagation in Wireless Communications (APWC) (pp.112-115). IEEE.

[35] M. Skolnik, Radar Handbook, New York, NY, USA:McGraw-Hill, 2008.

[36] J. Ghalibafan and S. M. Hashemi, "Leaky-Wave Centerline Longitudinal Slot Antenna Fed by Transversely Magnetized Ferrite," in IEEE Transactions on Magnetics, vol. 52, no. 1, pp. 1-4, Jan. 2016, Art no. 4000104, doi: 10.1109/TMAG.2015.2474310.

[37] T. R. Cameron, A. T. Sutinjo and M. Okoniewski, "Analysis and Design of Slitted Waveguides With Suppressed Slot-Mode Using Periodic FDTD," in IEEE Transactions on Antennas and Propagation, vol. 60, no. 8, pp. 3654-3660, Aug. 2012, doi: 10.1109/TAP.2012.2201098.

[38] A. M. Malekshah, M. S. Majedi and A. R. Attari, "Improved Design of Uniform SIW Leaky Wave Antenna With Suppression of Unwanted Mode," in IEEE Access, vol. 9, pp. 157623-157627, 2021, doi: 10.1109/ACCESS.2021.3130929.

[39] N. Javanbakht, M. S. Majedi and A. R. Attari, "Thinned Array Inspired Quasi-Uniform Leaky-Wave Antenna With Low Side-Lobe Level," in IEEE Antennas and Wireless Propagation Letters, vol. 16, pp. 2992-2995, 2017, doi: 10.1109/LAWP.2017.2756990.

[40] A. -R. Kiani, F. Geran, S. M. Hashemi and K. Forooraghi, "A Presentation of a Mathematical Formula to Design of a Quasi-Uniform Leaky-Wave Antenna With Ultralow Sidelobe Level," in IEEE Antennas and Wireless Propagation Letters, vol. 18, no. 5, pp. 901-905, May 2019, doi: 10.1109/LAWP.2019.2905529.

[41] G. Zamora, S. Zuffanelli, F. Paredes, F. J. Herraiz-Martínez, F. Martín and J. Bonache, "Leaky-wave antenna (LWA) based on slot line and non-bianisotropic split ring resonators (NB-SRRs) and comparison with CPW approach," 2014 IEEE-APS Topical Conference on Antennas and Propagation in Wireless

Communications (APWC), Palm Beach, Aruba, 2014, pp. 48-51, doi: 10.1109/APWC.2014.6905522.

[42] J. Liu, et al., "A simple technique for open-stopband suppression in periodic leaky-wave antennas using two nonidentical elements per unit cell", IEEE Trans. Antennas Propag., vol. 66, no. 6, pp. 2741-2751, Jun. 2018, doi: 10.1109/TAP.2018.2819701.

[43] Z. Liu, H. Lu, J. Liu, S. Yang, Y. Liu and X. Lv, "Compact Fully Metallic Millimeter-Wave Waveguide-Fed Periodic Leaky-Wave Antenna Based on Corrugated Parallel-Plate Waveguides," in IEEE Antennas and Wireless Propagation Letters, vol. 19, no. 5, pp. 806-810, May 2020, doi: 10.1109/LAWP.2020.2980993.

[44] A. J. Mackay and G. V. Eleftheriades, "Meandered and Dispersion Enhanced Planar Leaky-Wave Antenna With Fast Beam Scanning," in IEEE Antennas and Wireless Propagation Letters, vol. 20, no. 8, pp. 1596-1600, Aug. 2021, doi: 10.1109/LAWP.2021.3091979.

[45] W. Yin et al., "Frequency Scanning Single-Ridge Serpentine Dual-Slot-Waveguide Array Antenna," in IEEE Access, vol. 8, pp. 77245-77254, 2020, doi: 10.1109/ACCESS.2020.2989318.

[46] M. Hamedani, H. Oraizi, D. Zarifi and A. Amini, "Design of Ku-band Leaky-Wave Slot Array Antenna Based on Ridge Gap Waveguide," 2019 13th European Conference on Antennas and Propagation (EuCAP), Krakow, Poland, 2019, pp. 1-3.

[47] F. Xu, K. Wu and X. Zhang, "Periodic Leaky-Wave Antenna for Millimeter Wave Applications Based on Substrate Integrated Waveguide," in IEEE Transactions on Antennas and Propagation, vol. 58, no. 2, pp. 340-347, Feb. 2010, doi: 10.1109/TAP.2009.2026593.

[48] Bonache, J., Zamora, G., Paredes, F. et al. Controlling the Electromagnetic Field Confinement with Metamaterials. Sci Rep 6, 37739 (2016).

[49] J. Jing et al., "Theoretical Investigation of Optical Fiber Waveguide Coupled Surface Plasmon Resonance Sensor with Narrow Full Width at Half-Maximum," 2021 19th International Conference on Optical Communications and Networks (ICOCN), Qufu, China, 2021, pp. 1-2, doi: 10.1109/ICOCN53177.2021.9563778.

[50] E. Savchenko and O. Kuznetsova, "Total Internal Reflection Fluorescence Microscopy for Investigation of Dynamics of Single Molecules," 2018 IEEE International Conference on Electrical Engineering and Photonics (EExPolytech), St. Petersburg, Russia, 2018, pp. 268-271, doi: 10.1109/EExPolytech.2018.8564372.

[51] S. Z. Uddin and M. A. Talukder, "Reduction of detection volume in total internal reflection fluorescence microscopy using graphene," 2016 9th International Conference on Electrical and Computer Engineering (ICECE), Dhaka, Bangladesh, 2016, pp. 143-146, doi: 10.1109/ICECE.2016.7853876.

[52] Y. F. Yu, T. Bourouina and A. Q. Liu, "On-chip droplet enhanced fluorescence emission for low concentration protein measurement," TRANSDUCERS 2009 - 2009 International Solid-State Sensors, Actuators and Microsystems Conference, Denver, CO, USA, 2009, pp. 1250-1252, doi: 10.1109/SENSOR.2009.5285885.

[53] B. Adinolfi et al., "Total Internal Reflection Fluorescence-based Optical Biochip for the Detection of Immunosuppressants in Transplanted Patients," 2015 1st Workshop on Nanotechnology in Instrumentation and Measurement (NANOFIM), Lecce, Italy, 2015, pp. 39-42, doi: 10.1109/NANOFIM.2015.8425324.

[54] Y. Lin, C. Yang, J. Liou, C. Yu and G. Lin, "Using graphene nanoparticle embedded in photonic crystal fiber for evanescent wave mode locking of fiber laser", Opt. Express, vol. 21, no. 4, pp. 16763-16776, 2013.

[55] L. Gao, T. Zhu and Y. Li, "Watt-level, ultrafast fiber laser functioned with ultraweak evanescent field," 2017 Conference on Lasers and Electro-Optics Pacific Rim (CLEO-PR), Singapore, 2017, pp. 1-2, doi: 10.1109/CLEOPR.2017.8118870.

[56] V. Fitio, I. Yaremchuk, O. Vernyhor and Y. Bobitski, "Surface Plasmon Polariton Resonance Excitation by Grating on the Metal Substrate," 2019 International Conference on Information and Telecommunication Technologies and Radio Electronics (UkrMiCo), Odessa, Ukraine, 2019, pp. 1-4, doi: 10.1109/UkrMiCo47782.2019.9165347.

[57] A. Shaaban, H. Shaban, L. R. Gomaa and M. Swillam, "Surface Plasmon Polariton Excitation Based on Refractive Index Tunable Technique," 2022 Photonics North (PN), Niagara Falls, ON, Canada, 2022, pp. 1-1, doi: 10.1109/PN56061.2022.9908352.

[58] R. A. Pavelkin, S. Hayashi, V. A. Soifer and D. V. Nesterenko, "Anticrossing behavior of surface plasmon polaritons coupled with vibrational modes in planar plasmon structures," 2021 International Conference on Information Technology and Nanotechnology (ITNT), Samara, Russian Federation, 2021, pp. 1-4, doi: 10.1109/ITNT52450.2021.9649101.

[59] Y. -Q. Liu, J. Sun, L. Li and H. Yin, "Excitation of High-mode Spoof Surface Plasmon Polaritons(SSP) on a Metallic Grating by Electron Beam at Terahertz Spectrum," 2019 IEEE International Conference on Computational Electromagnetics (ICCEM), Shanghai, China, 2019, pp. 1-2, doi: 10.1109/COMPEM.2019.8778880.

[60] T. R. Jones, A. Fisher, D. W. Barlage and D. Peroulis, "A Photogenerated Silicon Plasma Waveguide Switch and Variable Attenuator for Millimeter-Wave Applications," in IEEE Transactions on Microwave Theory and Techniques, vol. 69, no. 12, pp. 5393-5403, Dec. 2021, doi: 10.1109/TMTT.2021.3121692.

[61] T. Sickel, P. Meyer and P. W. van der Walt, "An in situ Tunable Diode Mounting Topology for High-Power X-Band Waveguide Switches," in IEEE Transactions on Microwave Theory and Techniques, vol. 55, no. 2, pp. 281-286, Feb. 2007, doi: 10.1109/TMTT.2006.889146.

[62] Finkenzeller, K. RFID Handbook: Radio-Frequency Identification Fundamentals and Applications (Wiley, Chichester, 2004).

[63] "International Commission on Non-Ionizing Radiation Protection", [online] Available: https://www.icnirp.org/.

[64] R. Caso, A. Michel, A. Buffi, P. Nepa and G. Isola, "A modular antenna for UHF RFID near-field desktop reader," 2014 IEEE RFID Technology and Applications Conference (RFID-TA), Tampere, Finland, 2014, pp. 204-207, doi: 10.1109/RFID-TA.2014.6934228.

[65] A. Michel and P. Nepa, "UHF-RFID Desktop Reader Antennas: Performance Analysis in the Near-Field Region," in IEEE Antennas and Wireless Propagation Letters, vol. 15, pp. 1430-1433, 2016, doi: 10.1109/LAWP.2015.2511926

[66] A. Michel, A. Buffi, P. Nepa and G. Manara, "Antennas for UHF-RFID printer-encoders," 2015 IEEE 15th Mediterranean Microwave Symposium (MMS), Lecce, Italy, 2015, pp. 1-4, doi: 10.1109/MMS.2015.7375399.

[67] A. Michel, A. Buffi, P. Nepa and G. Manara, "Optimal antennas for RFID printer-encoders," 2016 IEEE International Symposium on Antennas and Propagation (APSURSI), Fajardo, PR, USA, 2016, pp. 1475-1476, doi: 10.1109/APS.2016.7696444.

[68] C. R. Medeiros, J. R. Costa and C. A. Fernandes, "RFID Smart Shelf With Confined Detection Volume at UHF," in IEEE Antennas and Wireless Propagation Letters, vol. 7, pp. 773-776, 2008, doi: 10.1109/LAWP.2008.2008672.

[69] J. S. Choi, H. Lee, D. W. Engels and R. Elmasri, "Passive UHF RFID-Based Localization Using Detection of Tag Interference on Smart Shelf," in IEEE Transactions on Systems, Man, and Cybernetics, Part C (Applications and Reviews), vol. 42, no. 2, pp. 268-275, March 2012, doi: 10.1109/TSMCC.2011.2119312.

[70] A. Michel, M. Rodriguez Pino and P. Nepa, "Reconfigurable Modular Antenna for NF UHF RFID Smart Point Readers," in IEEE Transactions on Antennas and Propagation, vol. 65, no. 2, pp. 498-506, Feb. 2017, doi: 10.1109/TAP.2016.2640140.

[71] A. Michel, M. Rodriguez Pino and P. Nepa, "Reconfigurable Modular Antenna for NF UHF RFID Smart Point Readers," in IEEE Transactions on Antennas and Propagation, vol. 65, no. 2, pp. 498-506, Feb. 2017, doi: 10.1109/TAP.2016.2640140.

[72] Shi, J., Qing, X., Chen, Z. N. & Goh, C. K. Electrically large dual-loop antenna for UHF near-field RFID reader. IEEE Trans. Antennas Propag. 61, 1019–1025 (2013).

[73] Michel, P. Nepa and M. R. Pino, "An overview on Modular Antennas for Near-field UHF-RFID systems," 2016 IEEE International Conference on RFID Technology and Applications (RFID-TA), Shunde, Foshan, China, 2016, pp. 16-18, doi: 10.1109/RFID-TA.2016.7750741.

[74] A. Michel, M. Rodriguez Pino and P. Nepa, "Reconfigurable Modular Antenna for NF UHF RFID Smart Point Readers," in IEEE Transactions on Antennas and Propagation, vol. 65, no. 2, pp. 498-506, Feb. 2017, doi: 10.1109/TAP.2016.2640140.

[75] Shi, J., Qing, X., Chen, Z. N. & Goh, C. K. Electrically large dual-loop antenna for UHF near-field RFID reader. IEEE Trans. Antennas Propag. 61, 1019–1025 (2013).

[76] X. Ren, Y. Yao, Y. Liang, J. Yu and X. Chen, "A Novel Multi-polarization UHF RFID Reader Antenna for Near-field Applications," 2020 IEEE International Symposium on Antennas and Propagation and North American Radio Science Meeting, Montreal, QC, Canada, 2020, pp. 1599-1600, doi: 10.1109/IEEECONF35879.2020.9329453.

[77] R. Xu and Z. Shen, "A Meander Line UHF RFID Reader Antenna with Uniform Near-field Distribution," 2021 IEEE International Symposium on Antennas and Propagation and USNC-URSI Radio Science Meeting (APS/URSI), Singapore, Singapore, 2021, pp. 175-176, doi: 10.1109/APS/URSI47566.2021.9704803.

Chapter 3

Microwave devices 3D printing-based prototyping

Currently, 3D printing has brought about a revolution in manufacturing and prototyping methods, facilitating the creation of intricate structures and models that were once prohibitively challenging or expensive to construct. This breakthrough has unlocked a myriad of possibilities for prototyping across diverse domains of research and industrial design, encompassing an array of applications, ranging from medical prosthetics [1] and biomaterials [2] to support structures and spare parts for industrial machinery.

3D printers offer a valuable solution in the realm of microwave applications, where the design and construction of prototypes typically incur higher costs and longer manufacturing times. 3D printing manufacturing can significantly reduce their production costs and provide research centers and small businesses with greater autonomy in the prototyping process.

When it comes to developing microwave devices using 3D printers, there exists various approaches that can be divided into two main approaches. In method one, non-conductive materials like polymers or ceramics are initially printed, and then specific areas or features of the device are metallized using techniques such as sputtering, conductive ink deposition, etc. These techniques have enabled rapid prototyping of antennas with favorable radiation characteristics [3]- [8]. The second method focuses on printing directly with

conductive materials [9]-[12]. This method uses conductive filaments containing metal particles or directly metal inks, eliminating the need for a separate metallization step. By directly printing with conductive materials, it becomes possible to fabricate microwave more intricate components or structures with integrated conductivity, such as antennas, transmission lines, or electronic circuits among others. Limited research has focused on 3D printing using conductive materials directly, with most studies focused on the use of 3D-printed dielectric filaments. It is important to note that standard PLA can also serve as a substrate for dielectric-filled waveguides and planar technology designs, enabling the complete fabrication of both dielectric and metallic parts using 3D printing. Nevertheless, this second method tends to be significantly costlier, as it requires more expensive materials and equipment. The choice between these approaches depends on factors including the specific requirements of the device, the intricacy of the design, and the availability of resources.

Taking into account that the designs of the electromagnetic field confinement devices and leaky wave antennas of this thesis are fundamentally rooted in waveguide technology, this chapter is dedicated to exploring and characterizing 3D printing-based prototyping with the Ultimaker 3 printing available in the research group. Section 3.1 provides an analysis of the characteristics of different metallization processes and are applied to PTFE-filled laminate transmission lines. In Section 3.2, microstrip stepped impedance filter based on 3D printing prototypes and metallization process are designed and characterized. Finally, Section 3.3 focuses on the study of the viability to fabricate a slotted rectangular waveguide using 3D printing techniques and the design and fabrication of a horn antenna.

3.1 Characterization of the metallization processes

In this section, the main objective is to show the viability of different 3D prototyping approaches. For this purpose, a preliminary study was conducted to determine the conductivity levels and performance that various materials could offer for microwave applications. The materials used were a conductive 3D filament (***Electrifi)*** from the company Multi3D [13], ***silver paint, nickel spray,*** and ***aluminium adhesive tape.***

Electrical conductivity is a property of materials that describes their ability to conduct electric current. This is crucial for microwave devices because low conductivity leads to poorer efficiency in signal transmission and reception. The higher the electrical conductivity of a material, the better its ability to allow electric current to flow through it. The electrical resistivity of a material, is related to electrical conductivity through the following equation [14]- [17]

$$\sigma = \frac{1}{\rho} \tag{3.1}$$

Where σ is the electric conductivity of the material in siemens per meter (S/m) and ρ is the electrical resistivity of the material in ohms per meter ($\Omega \cdot$ m). The resistivity can be computed by

$$\rho = R\,\frac{A}{l} \tag{3.2}$$

Where R is the electrical resistance in ohms (Ω), l is the length of the material along which electric current flows in meters (m), A is the cross-sectional area of the material through which electric current flows in square meters (m^2). From equation 3.2, it can be deduced that the resistivity of a material will increase as its geometry becomes narrower and larger.

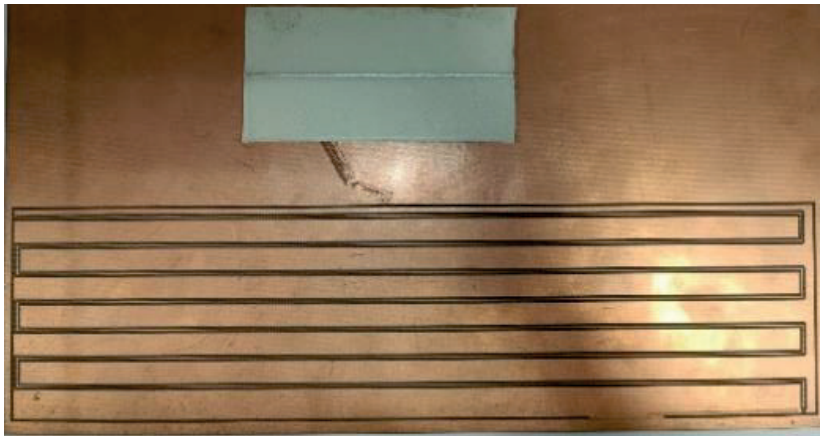


Figure 3.1. FR4 laminate and silver paint over printed PLA laminate.

Due to the limited capabilities of the ammeters available to measure low electrical resistance values (minimum 1Ω), long and narrow geometries were used to provide significant resistance. Figure 3.1 shows a copper serpentine line on a commercial FR4 laminate milled with a milling machine, and the silver line painted in a printed PLA structure. In the same way, the electric conductivity of the nickel spray, and the aluminum tape were characterized by means of long and narrow lines. As for the conductive filament, an Ultimaker 3D extended printer was used to print a narrow line. The Ultimaker 3 Extended printer is a high-performance 3D printer that offers dual extrusion capabilities, enabling the use of two different printing filaments. Furthermore, it is compatible with a wide range of materials, from common ones like PLA, nylon, and ABS to more advanced options.

Table 3.1. Comparison of electrical conductivity in different materials.

Material	Dimensions (mm)	Measured Resistance (Ω)	Theoretical conductivity (S/m)	Computed conductivity (S/m)
Copper	2100*0.3*0.035	5.1	$5.96*10^7$	$3.92*10^7$
Silver paint	100*0.5*0.05	7.1	$6.3*10^7$	$5.6*10^5$
Nickel spray	27*1.3*0.1	19.6	$1.43*10^7$	$1.05*10^4$
Aluminium tape	510*1*0.04	2.7	$3.77*10^7$	$4.72*10^6$
Electrifi [13]	30*1.3*0.2	40000	$16.6*10^3$	2.88

In Table 3.1 the dimensions of the material, the theoretical and computed electric conductivity and measured resistance are shown. The conductivity of copper in the FR4 laminate, calculated using this system, yields very similar results to that of pure copper. The adhesive aluminum also displayed very good conductivity, being only 10 times below than pure aluminum. This factor may be attributed to the aluminum being coated with plastic and adhesive material. The electrical conductivity of the silver paint obtained is 100 times lower than that of pure silver; however, it still surpasses that achieved by the nickel spray.

Finally, as it can be seen, the conductivity obtained was 1000 times smaller than what the supplier claims. In the time when this thesis was conducted, according to the information provided by the company, Electrifi was described as a unique 3D printing filament with a resistivity of 0.006 Ω cm, purportedly making it the only truly conductive filament available in the market. However, the results obtained demonstrate that this material is not a good electrical conductor. Adding to this issue, the material left residues on the printer head, eventually causing it to become clogged after only a few uses. It is important to mention that some studies demonstrate that it is possible to design certain RF applications with this material [11]-[12]. However, to make these designs viable, the use of special conductive pastes or inks is required, and even then, significant losses are experienced due to the low conductivity.

The use of aluminum adhesive can be impractical for complex designs, so at this point, it was decided to enhance the conductivity of the nickel spray and silver paint. To achieve this, the electrochemical process known as galvanization was proposed.

Electroplating or galvanization is an electrochemical process in which a metal is coated with another [18]-[21]. Has its origins in the pioneering work of Luigi Galvan. This process is commonly used to provide protection against corrosion, aesthetic qualities, and enhance the durability of metals. Electroplating is one of the main types of galvanization, alongside cold galvanization and hot-dip galvanization. The selection of the appropriate type of galvanization depends on the specific requirements of the application at hand. Each method offers its own advantages and can be tailored to achieve the desired outcome, ensuring the protection and longevity of the metal objects in various industries and applications. Cold galvanization involves the application of a zinc coating onto the metal using tools like spray guns, brushes, or rollers. This method creates a protective barrier against corrosion by depositing a layer of zinc. Hot-dip galvanization, in contrast, requires immersing the metal in a bath of molten zinc at high temperatures. This results in a strong bond between the zinc and the metal, generating a thick and durable coating. On the other hand, in electroplating, a solution containing salts and an electric current is employed to deposit a layer of metal onto the surface of the object. This method offers precise control over the thickness of the coating, making it suitable for achieving specific desired properties. Electroplating is widely used to add

various properties to surfaces that otherwise lack them, such as resistance to abrasion, wear, corrosion protection, lubrication needs, and even aesthetic qualities. It can also be employed to restore worn-out parts by increasing their thickness, as is the case with hard chrome plating.

During the electroplating process, the surface properties of an object undergo modification, encompassing changes in its chemical, physical, and mechanical characteristics. These changes are confined to the surface and does not affect the object's interior structure. This process can enhance the conductivity of a material (provided that the material possesses a certain level of conductivity) by depositing a metal with higher conductivity. In this electrochemical process, the anode and cathode of the cell are connected to an external power supply [see Fig.3.2 (a)]. They are submerged in a bath containing a solution of salts specific to the chemical element used for coating the object. The cathode, representing the object to be coated (receptor), is connected to the negative terminal, while the anode (donor), linked to the positive terminal releases ions into the solution through oxidation replenishing those consumed in the electrochemical reaction.

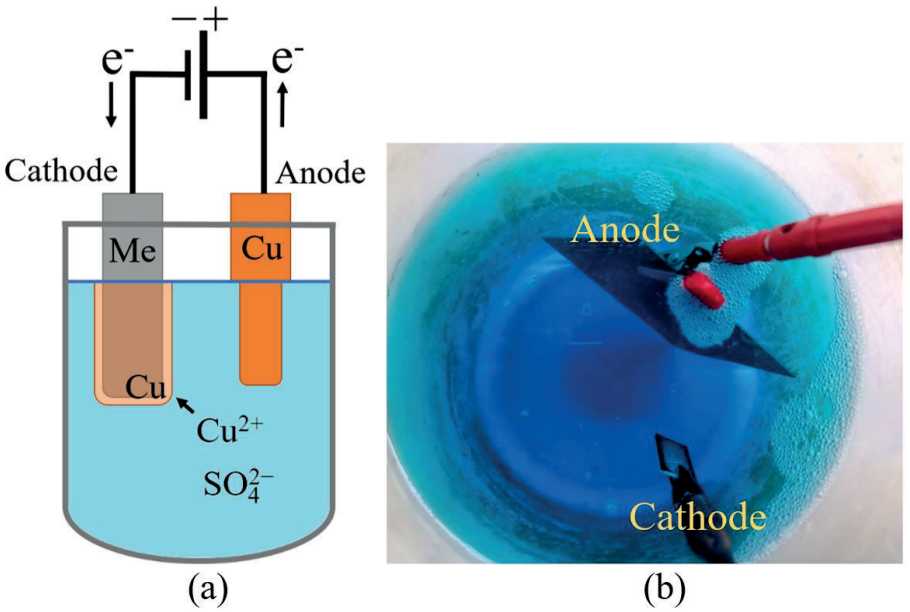


Figure 3.2. (a) Electroplating sketch. (b) Electroplating process with FR4 laminate as a donor and nickel T.L. as a receptor.

To carry out the electroplating process, a copper-coated FR4 sheet was employed as the donor material, with copper sulfate (II) used as the water-soluble crystalline substrate ($CuSO_4$). As depicted in Figure 3.2 (b), a plastic beaker was employed to contain the solution and immerse both the receptor and donor materials. The power supply was set at 2.5V and 0.5A throughout the entire process, which lasted 20 minutes for the silver paint case and 50 minutes for the nickel spray case. The following image (Fig. 3.3) shows the difference between the electrically conductive material deposited on a Roger RO3010 substrate before and after the electroplating process.

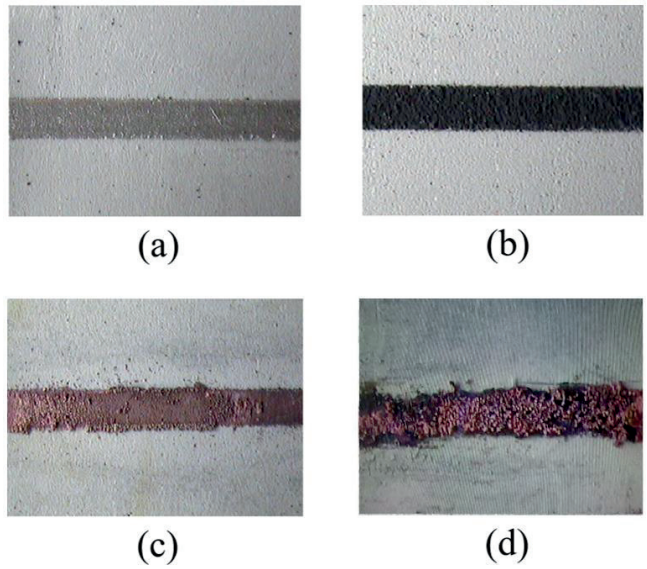


Figure 3.3. (a) Line made with silver ink. (b) Line made with nickel spray. (c) Line made with silver ink and galvanized with copper (20 mins). (d) Line made with nickel spray and galvanized with copper (50 mins).

Table 3.2. Comparison of electrical conductivity in different galvanized materials.

Material	LT Dimensions (mm)	Measured Resistance (Ω)	Theoretical conductivity (S/m)	Measured conductivity (S/m)
Silver paint	100*0.5*0.07	4.6	$6.3*10^7$	$6.2*10^5$
Nickel spray	27*1.3*0.12	8.3	$1.43*10^7$	$2*10^4$

In Figure 3.3, it can be observed that copper has been deposited in greater quantity on the silver paint; however, this hasn't translated into a significant improvement in conductivity, as it has only increased by 15% (Table 3.2). The line made with nickel spray has higher resistivity than the one composed of silver paint, so the copper deposition relative to the other under the same scenario will be lower. In this case, the nickel spray, which initially exhibited higher electrical resistivity, has doubled its conductivity. Nevertheless, silver paint still provides better conductivity, making it a better choice for metallizing 3D structures.

After measuring the electrical conductivity of the conductive materials, a transmission line was designed on a PTFE-filled laminate. The transmission line was designed to match the SMA connectors impedance (50 Ω) using Rogers RO3010 (h=50 mils, ε_r=10.2, tanδ=0.0023). The width W of the transmission line can be computed by [22]-[24].

$$\frac{W}{h} \leq 2 \begin{cases} \dfrac{W}{h} = \dfrac{8e^{A}}{e^{2A}-2} \\ A = \dfrac{Z_0}{60}\left\{\dfrac{\varepsilon_r+1}{2}\right\}^{0.5} + \dfrac{\varepsilon_r-1}{\varepsilon_r+1}\left\{0.23+\dfrac{0.11}{\varepsilon_r}\right\} \end{cases} \tag{3.3}$$

$$W/h \geq 2 \begin{cases} \dfrac{W}{h} = \dfrac{2}{\pi}\left\{(B-1)-\ln(2B-1)+\dfrac{\varepsilon_r-1}{2\varepsilon_r}\left[\ln(B-1)+0.39-\dfrac{0.61}{\varepsilon_r}\right]\right\} \\ B = \dfrac{60\pi^2}{Z_0\sqrt{\varepsilon_r}} \end{cases} \tag{3.4}$$

The computed width was validated with the design tool LineCalc from Advanced Design System (ADS) software. The computed width of the T.L. was 1.3 mm and the length was fixed at 30 mm.

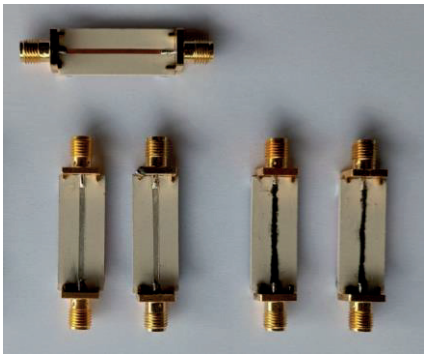


Figure 3.4. Transmission lines fabricated with different materials in Rogers RO3010.

One prototype of each conductor material was fabricated with a copper ground plane and other version was fabricated with the respective conductor material and both were compared to a copper fabrication (Fig.3.4).

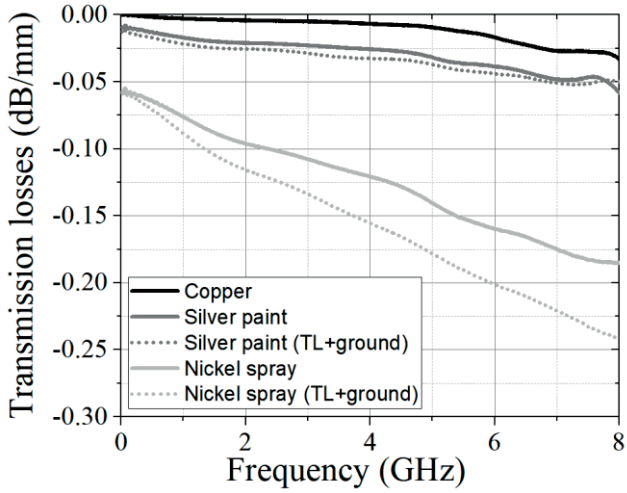


Figure 3.5. Transmission losses in dB/mm of transmission lines fabricated with different materials (solid line corresponds to copper ground plane, while the dotted line represents the ground plane made of the respective material.).

The scattering parameters of the microstrip lines were measured using a PNA Network Analyzer N5221A on a frequency band from 0.001 to 8 GHz. The measurement results in terms of transmission losses (in dB/mm) for all the fabricated lines are presented in Fig. 3.5. It can be seen that the transmission losses (in dB/mm) of the silver paint are quite similar independent to the ground plane material. However, in the case of the nickel spray, the difference of the transmission losses increases as frequency. These results are explained be the skin effect, referred as the tendency of electric current to distribute unevenly within a conductor. Its density is higher on the surface and lower in the inside. The skin depth of conductors is defined as [25]-[26]

$$\delta = \sqrt{\frac{1}{\pi f \mu \sigma}} \tag{3.5}$$

Where μ is the magnetic permeability of the material, σ is the electrical conductivity of the material and f is the operation frequency. Beyond 5δ from the surface, the electric current will be negligible. As the frequency increases,

the penetration depth δ decreases, indicating that the currents in the conductive layer cannot penetrate the material as deeply. Because the current is concentrated in a thinner surface layer, this layer experiences greater resistance due to its smaller cross-sectional area. This effect is especially exacerbated in the case of the transmission line made of nickel because it is a poorer conductor. Figure 3.6 and 3.7 shows the transmission losses of the fabricated transmission lines before and after electroplating process.

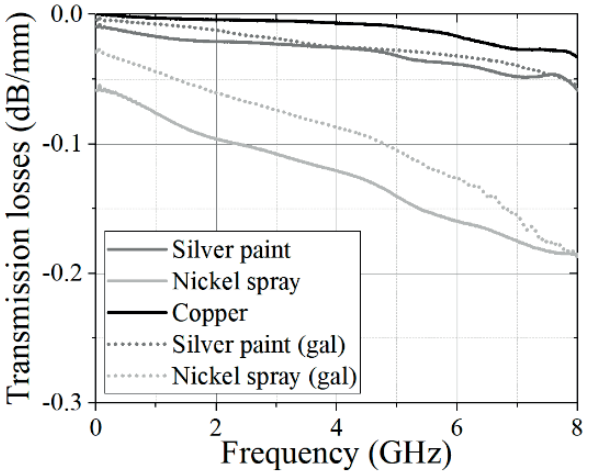


Figure 3.6. Transmission losses in dB/mm of transmission lines with copper ground plane fabricated with different materials (the solid line corresponds to the non-galvanized designs, while the dotted line represents the galvanized designs).

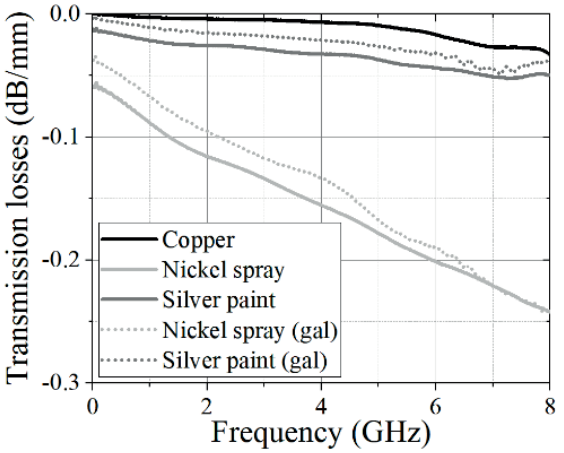


Figure 3.7. Transmission losses in dB/mm of TL fabricated with different materials (the solid line corresponds to the non-galvanized designs, while the dotted line represents the galvanized designs).

The measured transmission losses indicate that the electroplating process increase the conductivity in RF applications. However, it can be observed that from 6 to 8 GHz and higher frequencies, the transmission losses between the fabrications before and after the electroplating process tend to become equal.

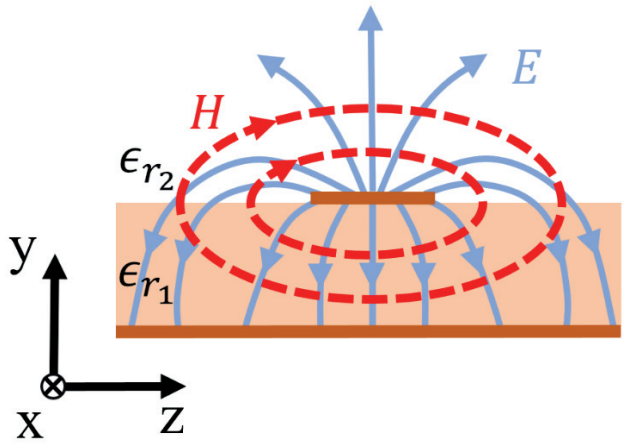


Figure 3.8. Microstrip line E and H field distribution.

As shown in Figure 3.8, electric field primarily interact with the inner layers of the structure. This leads to the fact that starting from 6 GHz, and given that the skin depth is 0.046 mm, most of the electric field only interacts with nickel and not with the electroplated copper layer, increasing the total resistance and, consequently, the Joule effect losses. Therefore, beyond a certain frequency, the impact of the electroplating process is negligible to increasing the electrical conductivity of the material. The frequency at which the electroplating process becomes ineffective will be determined by the electrical conductivity and the initial thickness of the material before undergoing electroplating.

3.2 Microstrip devices based on 3D printing

When considering planar technology prototyping methods, several options offer distinct advantages and constraints. **Drilling Machines** are renowned for their mechanical precision, making them ideal for crafting high-frequency circuits and microwave components; however, they require CNC programming skills, access to milling machines, and are slower for mass production. **Chemical Etching** boasts scalability and cost-effectiveness, yet it grapples with precision limitations, particularly in fine geometries and high-frequency applications. It

also demands stringent safety precautions and offers less precision than other methods. **Laser Engraving** stands out for its precision and speed in material removal, making it suitable for intricate geometries and high-frequency applications, though accessibility hinges on equipment availability. Finally, **PCB Printing** is widely accessible and cost-effective, ideal for both prototyping and small-scale production, but it may have limitations in precision, primarily suited to less complex circuit designs. The choice among these methods hinges on project-specific requirements, including precision needs, budget constraints, production scale, and equipment availability.

In this context, **3D printing** has emerged as a transformative technology for planar technology prototyping. It allows for the rapid fabrication of intricate structures with high precision and repeatability. 3D printers can accommodate a wide range of materials, including specialized substrates tailored to microwave applications.

In the previous chapter, an analysis was conducted on several processes and methods for metallizing structures fabricated by using 3D printing. Nevertheless, it is of particular interest to assess the capabilities they can offer in specific design scenarios. In this chapter, a transmission line and a microwave low-pass filter based on stepped impedance is designed and fabricated using a 3D printer.

3.2.1. Stepped impedance filter design

Microwave filters are essential in modern communication systems and radar technology by shaping and controlling signal bandwidth. These devices come in various types, depending on the frequency range they allow to pass through: low pass, high pass, band pass, and band-reject (or notch) filters. While at lower frequencies, conventional components like lumped inductors and capacitors can be used for filters, the challenge becomes significant when dealing with high-frequency signals, especially in the UHF and L-band regions. At these frequencies, achieving the required inductance and capacitance values becomes exceptionally challenging, making practical implementation unfeasible.

To overcome this limitation, engineers employ alternative techniques such as microstrip and resonant cavity methods to create high-frequency filters. Resonant cavity filters [27]-[28], for example, involve intricate mechanical structures that contain coupled cavities within a mechanical block, enhanced

by tuning screws and probes. In contrast, microstrip filters are constructed with conductive copper structures etched onto the top surface of a high-frequency, low-loss substrate with varying thickness, accompanied by a ground plane on the bottom surface. This technology provides a versatile platform for designing a wide range of filters, including coupled line filters [29]-[30], stub-loaded filters [31]-[32], substrate integrated waveguide (SIW) filters [33]-[35], stepped impedance filters [36]-[38], among others.

Stepped impedance filters provide a relatively straightforward approach to implementing low pass filters, involving alternating sections of high and low impedance lines. The designed low-pass filter is a Butterworth filter, order N=5, Z_0=50 Ω, f_c=1.5 GHz, Z_{High}=85 Ω, Z_{Low}=20 Ω, L_{ar}=3dB, ε_r=2.3. The design methodology can be found [36]-[38]. First of all, it must determine the value of g_1 - g_5 components and decide the impedance order. These parameters can be obtained from the Butterworth polynomials table in coefficient form [22], [39]. Then, the length of the high and low impedances can be found with the following equations [22], [36]-[38]:

$$l_{C_n} = g_n \frac{Z_{low}}{Z_0}\beta \tag{3.6}$$

$$l_{L_n} = g_n \frac{Z_0}{Z_{high}}\beta \tag{3.7}$$

Finally, the width can be easily computed by means of LineCalc or applying (3.3)-(3.4). In this design, the thickness of the dielectric was forced to be $h = 1$ mm. In Table 3.3 and Figure 3.9, the physical parameters of the designed filter are displayed.

Table 3.3. Dimensions of the stepped impedance filter.

l_1 (mm)	l_2 (mm)	l_3 (mm)	l_4 (mm)	l_{total} (mm)	w_1 (mm)	w_2 (mm)	w_3 (mm)
3	5.4	20	16	74.8	3	10	1.2

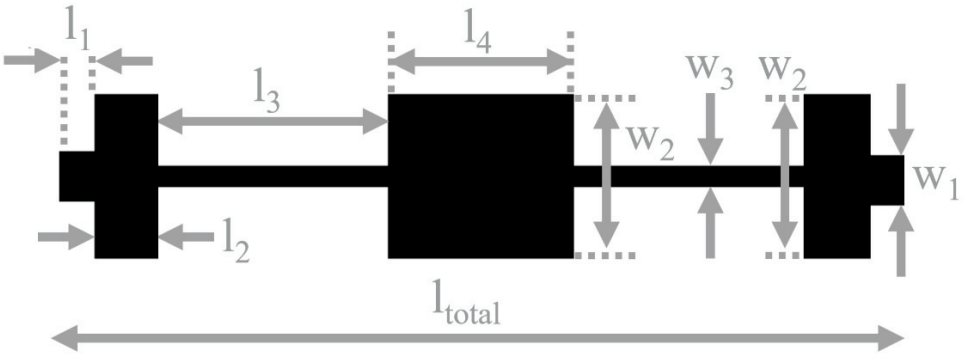
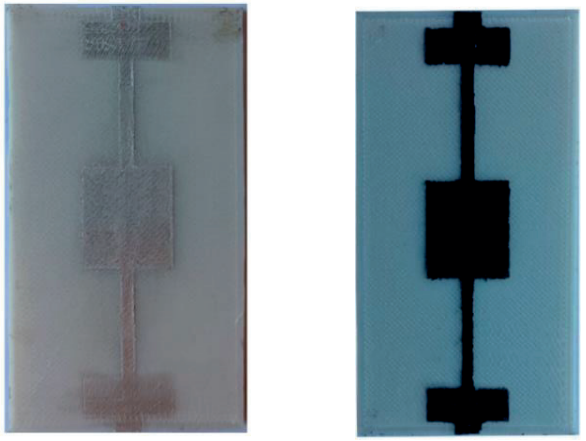


Figure 3.9. Layout of the stepped impedance filter.

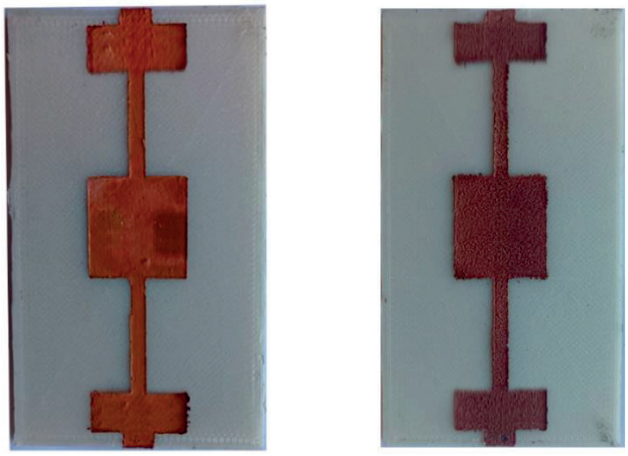
3.2.2. Filter prototyping and measured results

To manufacture the filter, the substrate was 3D printed in PLA. This material has been characterized in the laboratory and, with a 20% infill, it offers a relative permittivity ε_r=2.3. The thickness of the substrate ($h = 1$ mm) was specifically chosen to allow for the SMA connectors to be press-fit without the need for epoxy or soldering, to avoid deforming the substrate or modify the electric conductivity. To prime the material, a mask was created. This involved placing aluminum adhesive tape over the PLA laminate and removing it according to Fig.3.9 using a milling machine. Subsequently, the conductive material was applied (Fig.3.10). After obtaining the necessary experimental results, electroplating was used (Fig.3.11).



(a) (b)

Figure 3.10. Fabricated filter. (a) Silver ink. (b) Nickel spray.



(a) (b)

Figure 3.11. Fabricated filter. (a) Silver ink galvanized with copper. (b) Nickel spray galvanized with copper.

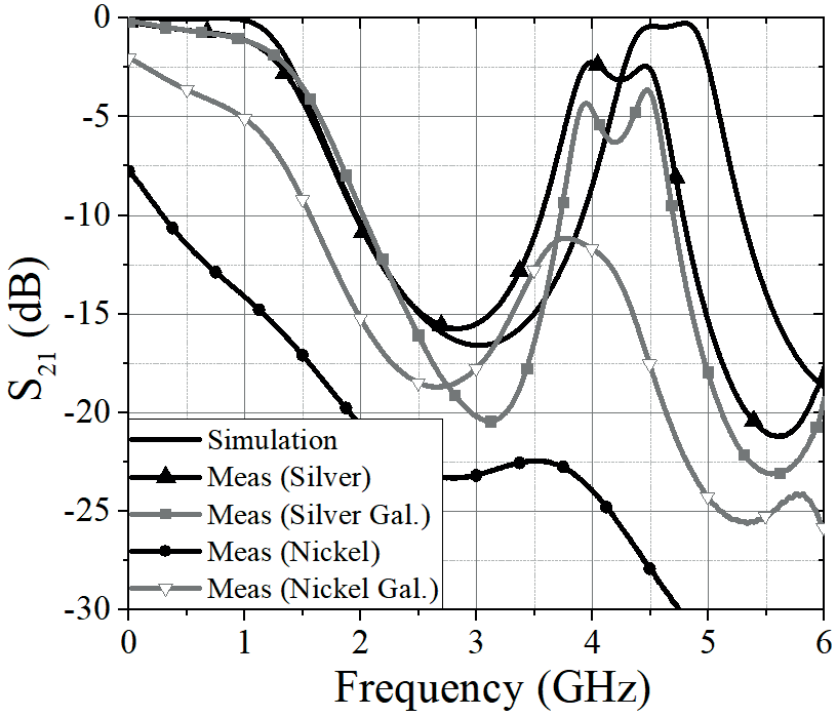


Figure 3.12. Transmission coefficient of the fabricated stepped impedance filters (the solid black line represents simulated results, the black line with triangles corresponds to silver paint, the grey line with squares represents galvanized silver paint, the black line with dots shows nickel spray, and the gray line with triangles indicates galvanized nickel spray).

Figure 3.12 shows the frequency response for the 5-section stepped impedance filter for different prototypes and simulation results. The simulation results were obtained by means of ADS. The materials used in the simulation were lossy copper as the metal layer, along with a lossy dielectric ($\varepsilon_r = 2.3$, $h = 1$ mm, $tan\delta = 0.023$). The results confirm the attainment of a 1.5 GHz cutoff frequency with silver paint. Additionally, it is noteworthy that there are 1 dB transmission losses within the passband. Conversely, for the nickel spray cases, the losses in the band pass are exceedingly high, resulting in passband losses exceeding -3 dB. These results shows that nickel spray is an inefficient choice for metallizing microwave structures due to its low conductivity and consequential losses. In contrast, silver paint demonstrated consistently favorable performance. The following section will showcase the results obtained from prototyping with silver-painted waveguides.

3.3 Waveguide prototyping based on 3D printing

The manufacturing of 3D microwave devices, including air-filled waveguides, corrugated waveguides, parallel plates, among other, has traditionally incurred substantial costs compared to planar technology. Various methods have been employed, such as manual machining, traditional casting processes, and more contemporary techniques like Computer Numerical Control (CNC) machining. Among these, CNC machining is the most widely used due to its ability to provide high precision, repeatability, and the capacity to create intricate and detailed components, leading to enhanced production efficiency and a reduction in human errors. Nevertheless, the high costs associated with CNC machining and the necessity for specialized equipment have restricted its accessibility, particularly for small research groups and projects with limited budgets.

In this context, 3D printing is a relatively rapid prototyping technology that offers significant advantages in terms of cost-effectiveness and accessibility, making it an appealing option for researchers and teams with constrained financial resources.

Although our research group can independently produce prototypes using milling machines (i.e., microstrip, coplanar, SIW, among others), creating waveguides remains a notable challenge. Nonetheless, access to an 3D printed

(Ultimaker 3 Extended) has been secured, allowing for 3D design capabilities and the potential production of waveguide prototypes. Moreover, 3D printer offers technical support for the measurement systems and equipment available within the research group. The aim is to ascertain whether this 3D printer can consistently manufacture the designs outlined in Sections 4 (Leaky Wave Antennas) and 5 (Electromagnetic Field Confinement Devices) while also determining the most efficient metallization processes. Initially, a pyramidal horn antenna design is explored due the relatively simple design and construction, facilitating an assessment of metallization processes. It's worth noting that attempts to create a slotted waveguide were hindered by the 3D printer's limited resolution. However, the successful fabrication of the pyramidal horn antenna highlights the 3D printer's potential for our research needs.

3.3.1 Horn antenna

Horn antennas, also known as microwave horns, consist of a metal waveguide that gradually expands into the shape of a horn. This design is used to focus and direct radio waves into a well-defined beam. The earliest forays into the world of horn antennas date back to 1897 when the Indo-Bengali researcher Jagadish Chandra Bose constructed one of the first versions during his pioneering experiments with microwaves. This milestone marked the beginning of exploring the capabilities of these antennas for the transmission and reception of electromagnetic signals. However, the modern design of the horn antenna, as we know it today, was independently developed in 1938 by Wilmer Barrow and G. C. Southworth. This advancement laid the foundation for their application in a wide range of technological fields.

These antennas exhibit remarkable features that make them highly versatile and valuable in various applications. Their high directivity allows for precise focusing of electromagnetic energy into directional beams, making them an ideal choice for situations requiring accurate pointing. In addition to being known for their low losses, their ability to operate over a broad frequency range, from microwaves to higher frequencies, makes them suitable for a variety of scenarios. Usually, horn antennas exhibit minimal losses, resulting in their directivity being approximately equal to their gain. They are commonly used as feed antennas (feed horns) in larger antenna structures [40]-[42]. They also

serve as standard calibration antennas for measuring the gain of other antennas and microwave radiometers, among other applications [43]-[44]. There are various types of horn antennas, each with specific designs and unique characteristics, allowing their use to be tailored to the specific needs of each application. These designs include pyramidal horn antennas, sectorial horns, conical horns, corrugated horns, ridged horns, among other variants [45]. Each type of horn antenna has its own advantages and specific applications in the communications and technology industry.

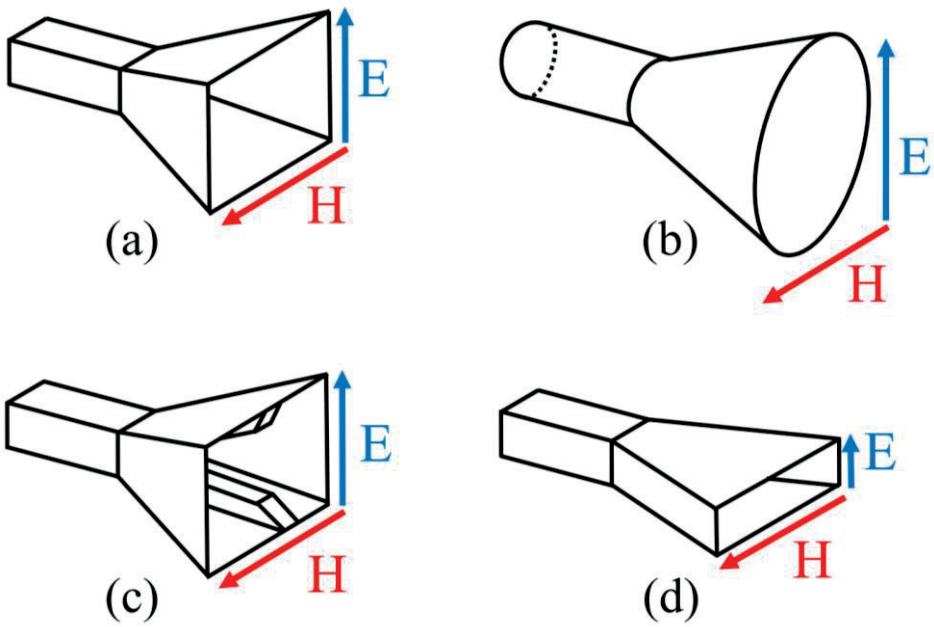


Figure 3.13. (a) Pyramidal horn. (b) Conical hon. (c) Ridged horn. (d) Sectorial H-plane horn.

3.3.1.1 Pyramidal horn antenna design

To design and manufacture a pyramidal horn antenna, the design methodology outlined in [45]-[47] for achieving optimum gain was used. Typically, when designing a pyramidal horn, the desired gain G_0 and the dimensions of the rectangular feed waveguide a and b are known. The objective is to determine the remaining dimensions that will result in optimum gain. In this specific design, the chosen operating frequency was 6 GHz, with a target

gain of 16 dB. The design used the WR159 waveguide standard with dimensions a = 40.38 mm and b = 20.19 mm. Figure 3.14 provides a visual representation of the horn structure, highlighting its key physical parameters. The feed system was based on a commercial SMA connector (50Ω), which was inserted inside the waveguide (it acts as a $\lambda/4$ antenna) and connected to a coaxial cable. In this commonly employed technique, the most efficient location for placing the probe is typically at the center of the wide wall, $\lambda_g/4$ (where λ_g is the guided wavelength of the guided mode) distance from the shorted-end end of the waveguide, and parallel to the narrow wall. A more comprehensive explanation of waveguide feeding systems is provided in Chapter 4.

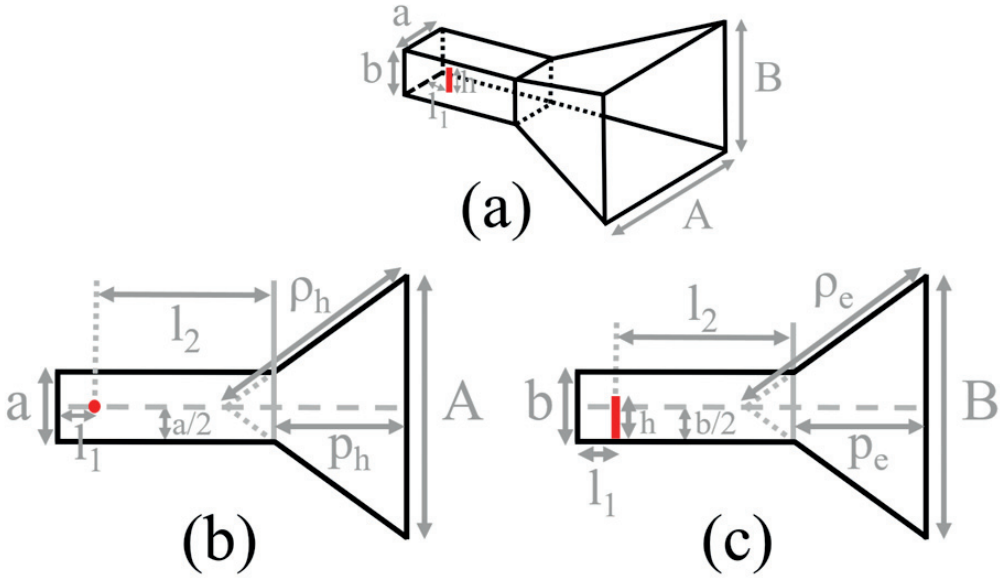


Figure 3.14. (a) Pyramidal horn. (b) H-plane view. (c) E-plane view.

As an initial design step, it must determine the value of χ according to the iterative equation (3.8). This parameter establishes the relationship between the antenna's physical dimensions and the wavelength of the operating frequency. The value of χ (Table 3.4) can be easily obtained using computational software tools such as Wolfram Alpha, Matlab, Python, etc.

$$\left(\sqrt{2\chi}-\frac{b}{\lambda}\right)^2(2\chi-1)=\left(\frac{G_0}{2\pi\sqrt{\chi}}\sqrt{\frac{3}{2\pi}}-\frac{a}{\lambda}\right)^2\left(\frac{{G_0}^2}{6\pi^3\chi}-1\right) \tag{3.8}$$

Where G_0 is the desire gain in linear scale, and λ de wavelength in free space. After obtaining the value of χ, the next steps involve calculating the slant heights ρ_e and ρ_h, corresponding to the E-field and H-field directions, and subsequently determining the optimal aperture sizes A and B using the following equations:

$$\frac{\rho_e}{\lambda} = \chi \tag{3.9}$$

$$\frac{\rho_h}{\lambda} = \frac{{G_0}^2}{8\pi^3\chi} \tag{3.10}$$

$$A \approx \sqrt{3\lambda\rho_h} \tag{3.11}$$

$$B \approx \sqrt{2\lambda\rho_e} \tag{3.12}$$

Finally, the optimum aperture distance can be determined through next equation

$$p_e = (B-b)\left[\left(\frac{\rho_e}{B}\right) - \frac{1}{4}\right]^{1/2} \approx p_h \tag{3.13}$$

For the design of the matching network, the first step is to calculate the guide wavelength at the operation frequency. This will provide an initial value for the probe's position and length, which will later need to be optimized through simulation. In a waveguide, the mode guide wavelength is given by

$$\lambda_g = \frac{2\pi}{\beta_g} = \frac{2\pi}{\sqrt{{k_0}^2 - {k_c}^2}} = \boxed{\frac{2\pi}{\sqrt{{k_0}^2 - \left(\sqrt{\left(\frac{m\pi}{a}\right)^2 + \left(\frac{n\pi}{b}\right)^2}\right)^2}}} \tag{3.14}$$

Where k_0 is the wavenumber in vacuum and k_c is the cutoff wavenumber. Applying equation (3.14) considering only the mode TE_{10} (m=1, n=0), the parameter was found to be $l_1 = 16$ mm. The quarter-wave prove at 6 GHz lead to $h = 12.5$mm. Nevertheless, these parameters are indicative. Through an

iterative simulation procedure, it is possible to obtain a more accurate value. To perform this process, acquire the value of l_2, and to validate the design, the antenna was simulated using CST Studio Suite 2014 software. The material used in the simulation was lossy aluminium and Rogers RT5870 ($\varepsilon_r = 2.33$, $\tan\delta = 0.0012$) in the dielectric coaxial modelling. The final optimized design parameters are summarized in Table 4 and the structure is shown in Fig.3.15.

Table 3.4. Dimensions of the horn antenna.

	χ	A(mm)	B(mm)	p_e (mm)	h(mm)	l_1(mm)	l_2(mm)
Value	2.3179	143.4	107.9	85	10.5	7	43

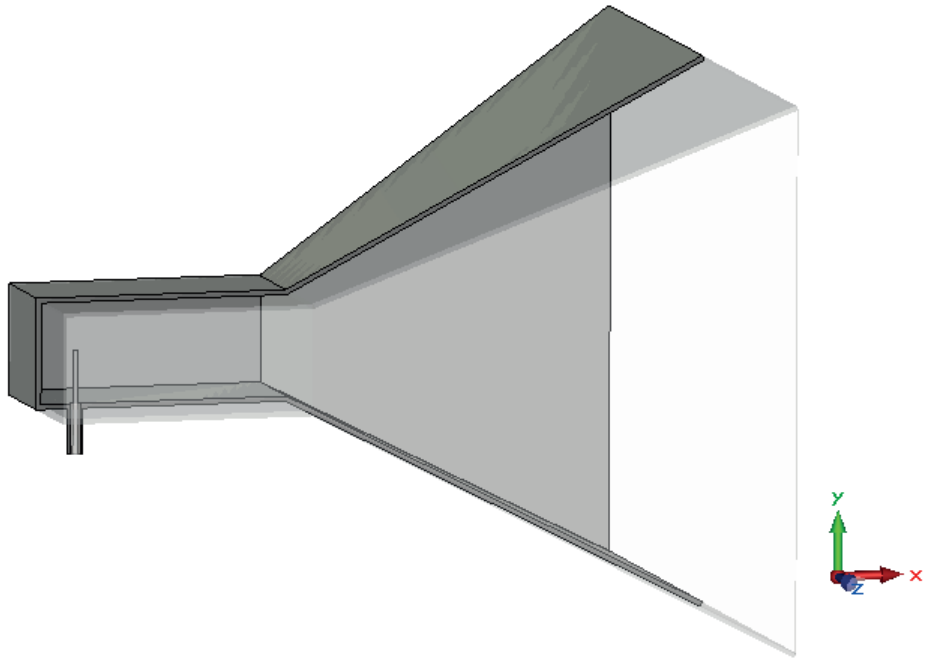


Figure 3.15. Design of the horn antenna.

3.3.1.2 Prototyping and measured results

After completion of the design, the antenna was modified to accommodate the SMA connector, and was divided into 6 parts to enable 3D printing (see Fig. 3.16). The coaxial connector used (RS Pro straight panel mount SMA connector, jack, solder termination, RS Stock No: 546-3181) underwent

modifications to ensure it matched the dimensions specified in the simulation design. The same software employed for antenna design was used to split the antenna into different pieces. After 3D printing the PLA pieces, they were subsequently coated with metal. In one instance, silver paint was employed for metallization, while aluminum adhesive tape was used in the other. Following metallization, the assembly process took place, which involved attaching the SMA connector. The image below (Fig.3.16) depicts this prototyping procedure.

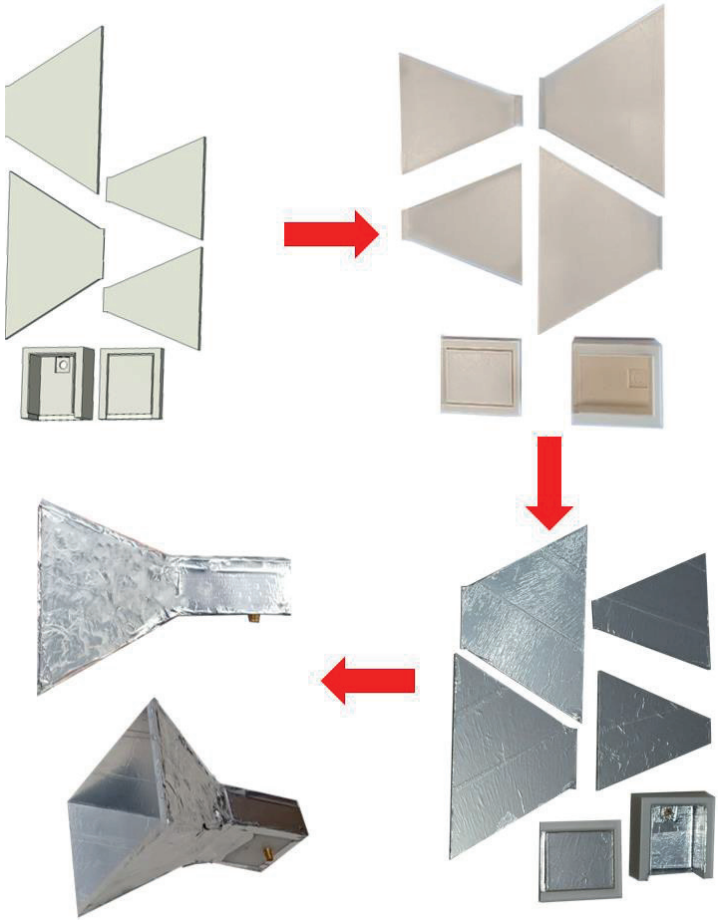


Figure 3.16. Antenna fabrication procedure.

The measured and simulated input reflection coefficient of both prototypes are shown in Fig.3.17. The S-parameters were measured with the Agilent N5221A PNA Network Analyzer. The fabricated antennas show a very reasonably good agreement with the simulated results. The bandwidth with reflection coefficient below -10 dB is between 5.6 GHz to 6.35 GHz.

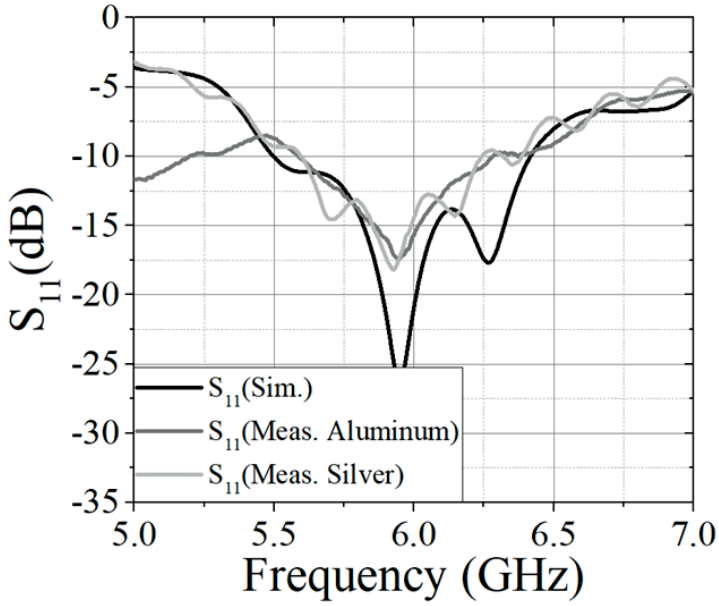


Figure 3.17. Reflection coefficient (the black line represents simulated results, dark grey indicates measured results with aluminium tape, and light grey shows measured results with silver paint).

To validate the prototyping procedure, a far-field measurement system was also used (Fig.3.18). The measurement setup consists of an Agilent E8364B PNA series 2-port network analyzer and a characterized horn antenna as reference antenna.

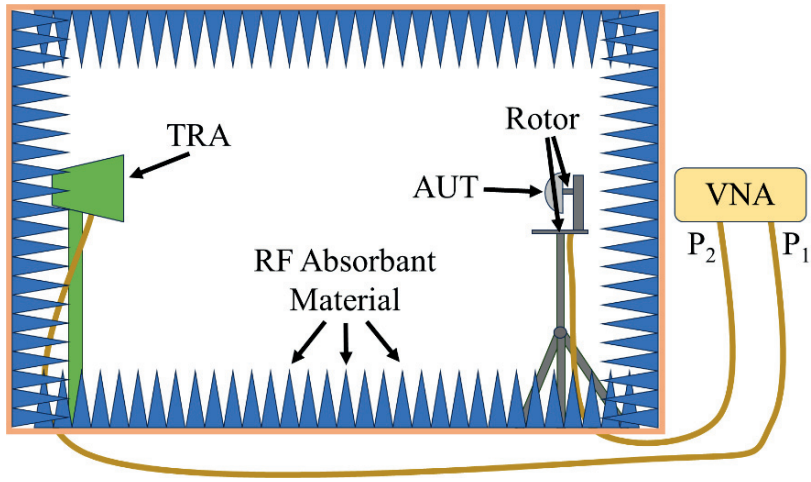


Figure 3.18. Scheme of the far-field Antenna measurement setup.

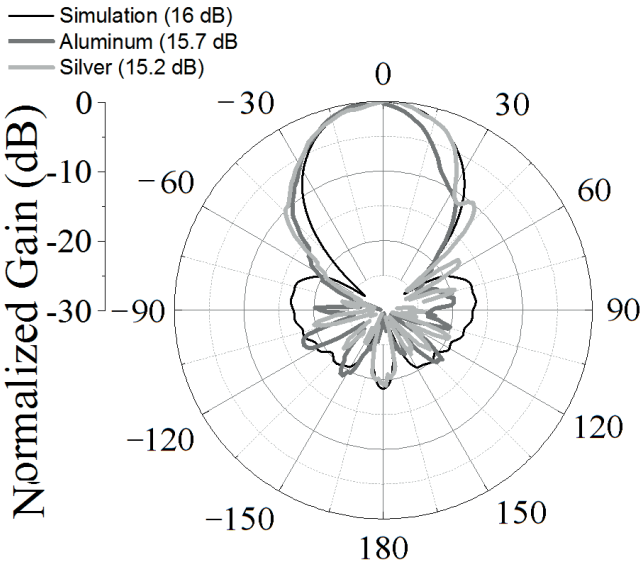


Figure 3.19. Co-polarization normalized gain at 6 GHz (the black line represents simulated results, dark grey corresponds to measured results with aluminium tape, and light grey indicates measured results with silver paint).

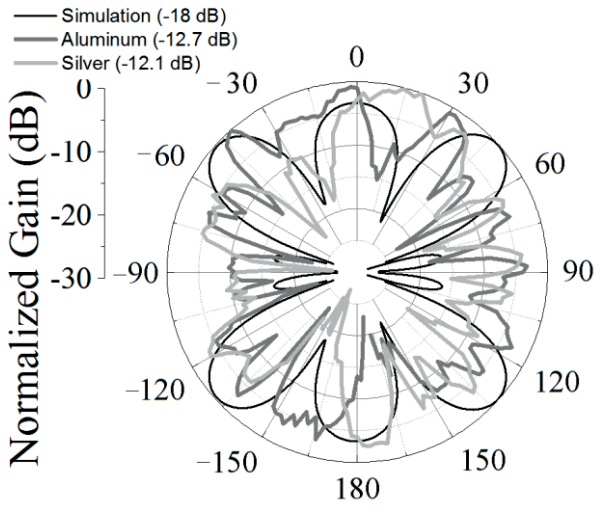


Figure 3.19. Cross-polarization normalized gain at 6 GHz (the black line represents simulated results, dark grey corresponds to measured results with aluminium tape, and light grey indicates measured results with silver paint).

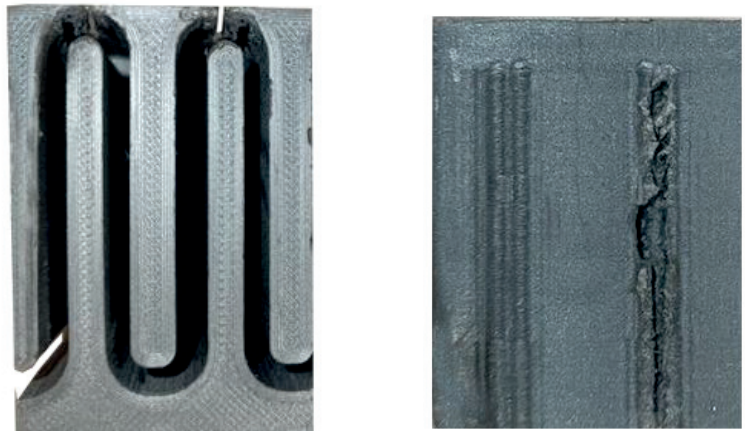
The simulated and measured normalized radiation far-field patterns of the antenna in the E-plane and H-plane at 6 GHz are presented in Figures 3.18 and 3.19, respectively. The measured co-polarization shows good agreement with

the simulated results. As observed, the prototype metallized with aluminum adhesive tape demonstrates a higher gain (15.7 dB) compared to the prototype metallized with silver paint (15.2 dB). In the operational frequency range, the measured cross-polarization levels for the antennas fabricated with aluminum and silver are below -12.7 dB and -12.1 dB, respectively, while the simulated results show values below -18 dB. Nevertheless, it's not a very significant difference, and can be primarily attributed to conductor losses and the manufacturing tolerances of the printer and assembly process.

This prototype, being based on PLA, has a low density compared to an aluminum-made antenna, making it ideal for applications where a lightweight design is required.

3.3.2 Slotted waveguide

The main prototype of the structures outlined in Chapter 4 and Chapter 5 are based on air-filled waveguide structure. The proposed devices are founded on a serpentine rectangular waveguide loaded with transversal slots. Diverse prototypes with different dimensions and printer configurations were experimented for various operation frequencies. Regrettably, as illustrated in Figure 3.20, despite employing a reduced printing speed and the smallest print heads (extruder), the structure could not be successfully fabricated, leading to various complications in the slots and the joints.



(a) (b)

Figure 3.20. (a) Transversal view of a serpentine slotted waveguide structure. (b) top view of serpentine slotted waveguide structure.

Additionally, the total printing time and material required were excessively long. Consequently, the decision was made to look for an external company that could manufacture the structures in aluminum. Ultimately, a company specializing in CNC (Computer Numerical Control) machining was commissioned to create the prototype.

3.4 3D prototyping conclusions

In this chapter, the viability of 3D printing for various RF devices, as well as different metallization processes and their optimization through electroplating, has been investigated. The conductivity of silver paint, nickel spray, aluminum adhesive tape, and the Electrifi 3D printing material has been characterized. A stepped impedance filter with a PLA-based substrate was designed and manufactured, allowing for practical experimentation with the results provided by both nickel spray and silver paint. Furthermore, a functional horn antenna was fabricated using PLA, resulting in excellent performance with both silver paint and aluminum.

Although the results were not the desired ones related to the main designs, this work served to support the designs used in the following chapters. As will be demonstrated, the aluminum tape was employed to mitigate reflection losses between the matching network and the periodic structure, among other parts of the waveguide structure, across various configurations. On the other hand, silver paint was used to metallize the sides of the Substrate Integrated Waveguide (SIW) structure.

In the future, a resin 3D printer can be tested. This type of printer typically offers higher resolution and precision than a filament printer. Additionally, it can use other conductive materials or metallization techniques.

REFERENCES

[1] Tian Y, Chen C, Xu X, Wang J, Hou X, Li K, Lu X, Shi H, Lee ES, Jiang HB. A Review of 3D Printing in Dentistry: Technologies, Affecting Factors, and Applications. Scanning. 2021 Jul 17;2021:9950131. doi: 10.1155/2021/9950131. PMID: 34367410; PMCID: PMC8313360.

[2] Zhu W, Ma X, Gou M, Mei D, Zhang K, Chen S. 3D printing of functional biomaterials for tissue engineering. Curr Opin Biotechnol. 2016 Aug;40:103-112. doi: 10.1016/j.copbio.2016.03.014. Epub 2016 Apr 1. PMID: 27043763.

[3] S. Mufti, A. Tennant and L. Seed, "3D printed electrically small planar inverted-F antenna: Efficiency improvement through voluminous expansion", Proc. IEEE Int. Symp. Antennas Propag. (APSURSI), pp. 811-812, Jun./Jul. 2016.

[4] E. A. Rojas-Nastrucci, J. Nussbaum, T. M. Weller and N. B. Crane, "Metallic 3D printed Ka-band pyramidal horn using binder jetting", Proc. IEEE MTT-S Latin Amer. Microw. Conf. (LAMC), pp. 1-3, Dec. 2016.

[5] C. R. Garcia, R. C. Rumpf, H. H. Tsang and J. H. Barton, "Effects of extreme surface roughness on 3D printed horn antenna", Electronics Letters, vol. 49, pp. 734-736, 2013.

[6] Y. Tawk, M. Chahoud, M. Fadous, J. Costantine and C. G. Christodoulou, "The miniaturization of a partially 3-D printed quadrifilar helix antenna", IEEE Trans. Antennas Propag., vol. 65, no. 10, pp. 5043-5051, Oct. 2017.

[7] J. -M. Poyanco, N. Castro, F. Pizarro and E. Rajo-Iglesias, "3D-printed Wideband Hyperbolic Lens Antenna for Ka-band," 2020 14th European Conference on Antennas and Propagation (EuCAP), Copenhagen, Denmark, 2020, pp. 1-5, doi: 10.23919/EuCAP48036.2020.9135878.

[8] J. Pourahmadazar, S. Sahebghalam, S. Abazari Aghdam and M. Nouri, "A millimeter-wave fresnel zone plate lens design using perforated 3D printing material", 2018 IEEE MTT-S International Microwave Workshop Series on Advanced Materials and Processes for RF and THz Applications (IMWS-AMP), pp. 1-3, July 2018.

[9] S. Roy, M. B. Qureshi, S. Asif and B. D. Braaten, "A model for 3D-printed microstrip transmission lines using conductive electrifi filament", Proc. IEEE

Int. Symp. Antennas Propag. USNC/URSI Nat. Radio Sci. Meeting, pp. 1099-1100, Jul. 2017.

[10] O. Yurduseven, S. Ye, T. Fromenteze, B. J. Wiley, D. R. Smith. "3D Conductive Polymer Printed Metasurface Antenna for Fresnel Focusing". MDPI Designs, September 4, 2019.

[11] N. Lazarus, S. S. Bedair, S. H. Hawasli, M.-J. Kim, B. J. Wiley, G. L. Smith. "Selective Electroplating for 3D-Printed Electronics". Advanced Materials Technology, May 20, 2019.

[12] F. Pizarro, R. Salazar, E. Rajo-Iglesias, M. Rodríguez, S. Fingerhuth and G. Hermosilla, "Parametric Study of 3D Additive Printing Parameters Using Conductive Filaments on Microwave Topologies," in IEEE Access, vol. 7, pp. 106814-106823, 2019, doi: 10.1109/ACCESS.2019.2932912.

[13] MULTI3D, Sep. 2023, [online] Available: https://www.multi3dllc.com/.

[14] David Halliday, Robert Resnick, Jearl Walker, Fundamentals of Physics, Binder Ready Ve edition, WILEY, 2013.

[15] Nilsson James, Riedel Susan, Electric Circuits, first edition, Financial Times Prentice Hall, 2014.

[16] David J. Griffiths, Introduction to Electrodynamics 4th edition, Cambridge University Press, 2017.

[17] Paul A. Tipler, Gene P. Mosca, Physics for Scientists and Engineers, 5th edition, W.H.Freeman & Co Ltd, 2003.

[18] Mordechay Schlesinger, Milan Paunovic, Modern Electroplating, 5th edition, Wiley, 2014.

[19] Jack W. Dini, "Electrodeposition: The Materials Science of Coatings and Substrates (Materials Science and Process Technology)", 1st Edition, William Andrew, 1994.

[20] Allen-J Bard, Larry-R Faulkner, Electrochemical Methods: Fundamentals and Applications, 2nd Edition, Wiley, 2001.

[21] J.R. Davis, Surface Engineering for Corrosion and Wear Resistance, 1st Edition, CRC Press, 2001.

[22] David M. Pozar, Microwave Engineering, fourth edition, Hoboken, NJ, USA:John Wiley & Sons Inc, 2011.

[23] K. C. Gupta, Ramesh Garg, I. J. Bahl, Microstrip Lines and Slotlines, 1st edition, Artech House Publishers, 1979.

[24] J.-S. Hong and M. J. Lancaster, Microstrip Filters for RF/Microwave Applications, 1st edition, New York:Wiley-Interscience, 2001.

[25] William Hayt, John Buck, "Engineering Electromagnetics", seventh edition, McGraw-Hill Education, 2005.

[26] Roald K. Wangsness, Electromagnetic Fields, 1st edition, John Wiley & Sons Inc, 1979.

[27] R. Lovato and X. Gong, "A Third-Order SIW-Integrated Filter/Antenna Using Two Resonant Cavities," in IEEE Antennas and Wireless Propagation Letters, vol. 17, no. 3, pp. 505-508, March 2018, doi: 10.1109/LAWP.2018.2799518.

[28] D. Psychogiou, B. Vaughn, R. Gómez-García and D. Peroulis, "Reconfigurable Multiband Bandpass Filters in Evanescent-Mode-Cavity-Resonator Technology," in IEEE Microwave and Wireless Components Letters, vol. 27, no. 3, pp. 248-250, March 2017, doi: 10.1109/LMWC.2017.2661882.

[29] Chao-Huang Wu, Yo-Shen Lin, Chi-Hsueh Wang and Chun Hsiung Chen, "Novel microstrip coupled-line bandpass filters with shortened coupled sections for stopband extension," in IEEE Transactions on Microwave Theory and Techniques, vol. 54, no. 2, pp. 540-546, Feb. 2006, doi: 10.1109/TMTT.2005.862710.

[30] C. -J. Chen, "A Coupled-Line Coupling Structure for the Design of Quasi-Elliptic Bandpass Filters," in IEEE Transactions on Microwave Theory and Techniques, vol. 66, no. 4, pp. 1921-1925, April 2018, doi: 10.1109/TMTT.2017.2783378.

[31] N. Sekiya and S. Sugiyama, "Design of Miniaturized HTS Dual-Band Bandpass Filters Using Stub-Loaded Meander Line Resonators and Their Applications to Tri-Band Bandpass Filters," in IEEE Transactions on Applied Superconductivity, vol. 25, no. 3, pp. 1-5, June 2015, Art no. 1500805, doi: 10.1109/TASC.2014.2362352.

[32] B. Ren, X. Liu, X. Guan and Z. Ma, "High-Selectivity High-Temperature Superconducting Triband Balanced Bandpass Filter Using Symmetric Stub-Loaded Resonator," in IEEE Transactions on Applied Superconductivity, vol.

33, no. 8, pp. 1-5, Nov. 2023, Art no. 1501905, doi: 10.1109/TASC.2023.3315072.

[33] T. R. Jones and M. Daneshmand, "Miniaturized Slotted Bandpass Filter Design Using a Ridged Half-Mode Substrate Integrated Waveguide," in IEEE Microwave and Wireless Components Letters, vol. 26, no. 5, pp. 334-336, May 2016, doi: 10.1109/LMWC.2016.2549000.

[34] M. Nosrati, Z. Abbasi and M. Daneshmand, "Single-Layer Substrate-Integrated Waveguide Evanescent-Mode Filter," in IEEE Microwave and Wireless Components Letters, vol. 28, no. 12, pp. 1107-1109, Dec. 2018, doi: 10.1109/LMWC.2018.2875313.

[35] J. R. Sánchez, C. Bachiller, M. Juliá, V. Nova, H. Esteban and V. E. Boria, "Microwave Filter Based on Substrate Integrated Waveguide With Alternating Dielectric Line Sections," in IEEE Microwave and Wireless Components Letters, vol. 28, no. 11, pp. 990-992, Nov. 2018, doi: 10.1109/LMWC.2018.2871644.

[36] A. Baloolad, R. K. Manjunath, P. Kumar, S. Kareemulla and K. Sreelakshmi, "Design, Simulation and Analysis of Stepped Impedance Micro-Strip Low Pass Filter for 10GHz band," 2022 2nd International Conference on Intelligent Technologies (CONIT), Hubli, India, 2022, pp. 1-5, doi: 10.1109/CONIT55038.2022.9848198.

[37] W. Zhou, W. Xia, J. Zhang, D. He, C. Liu and Z. Wu, "Flexible Graphene Based Films for Stepped Impedance Lowpass Microstrip Filter," 2018 IEEE International Conference on Computational Electromagnetics (ICCEM), Chengdu, China, 2018, pp. 1-3, doi: 10.1109/COMPEM.2018.8496690.

[38] Jia-Sheng Hong, M. J. Lancaster, Microstrip Filters for RF/Microwave Applications, 1st edition, Wiley-Interscience, 2001.

[39] Steven Smith, Digital Signal Processing: A Practical Guide for Engineers and Scientists, 1st edition, Newnes, 2002.

[40] O. B. Jacobs, J. W. Odendaal and J. Joubert, "Elliptically Shaped Quad-Ridge Horn Antennas as Feed for a Reflector," in IEEE Antennas and Wireless Propagation Letters, vol. 10, pp. 756-759, 2011, doi: 10.1109/LAWP.2011.2163050.

[41] K. K. Shee and W. T. Smith, "Optimizing multimode horn feed arrays for offset reflector antennas using a constrained minimization algorithm to reduce cross

polarization," in IEEE Transactions on Antennas and Propagation, vol. 45, no. 12, pp. 1883-1885, Dec. 1997, doi: 10.1109/8.650210.

[42] O. B. Jacobs, J. W. Odendaal and J. Joubert, "Elliptically Shaped Quad-Ridge Horn Antennas as Feed for a Reflector," in IEEE Antennas and Wireless Propagation Letters, vol. 10, pp. 756-759, 2011, doi: 10.1109/LAWP.2011.2163050.

[43] M. Zhu, P. Chen and X. Yu, "Design of an L-band orthogonal dual-polarized horn antenna with metal grids for microwave radiometer," 2020 International Conference on Microwave and Millimeter Wave Technology (ICMMT), Shanghai, China, 2020, pp. 1-3, doi: 10.1109/ICMMT49418.2020.9386390.

[44] H. Wang, "Compact Multi-frequency Feed Horn for Radiometer," 2021 IEEE International Symposium on Antennas and Propagation and USNC-URSI Radio Science Meeting (APS/URSI), Singapore, Singapore, 2021, pp. 1779-1780, doi: 10.1109/APS/URSI47566.2021.9704558.

[45] C. A. Balanis, Antenna Theory: Analysis and Design, 4th edition, New Jersey:John Wiley & Sons Publication (Wiley Interscience), 2005.

[46] A. Alam, S. Urooj and A. Q. Ansari, "Design and Simulation of 24 GHz high gain pyramidal Horn Antenna for Bio-Radar Sensing Application," 2023 International Conference on Recent Advances in Electrical, Electronics & Digital Healthcare Technologies (REEDCON), New Delhi, India, 2023, pp. 596-599, doi: 10.1109/REEDCON57544.2023.10151440.

[47] K. T. Selvan, "Accurate Design Method for Pyramidal Horns of Any Desired Gain and Aperture Phase Error," in IEEE Antennas and Wireless Propagation Letters, vol. 7, pp. 31-32, 2008, doi: 10.1109/LAWP.2007.914119.

Chapter 4

Leaky Wave Antenna Design

In this chapter a periodic LWA with backward to forward radiation with efficient broadside radiation is designed and characterized. The structure is based in a serpentine waveguide loaded with transversal slots in the wide wall. Both unidirectional and bidirectional versions are introduced. Moreover, the matching network is also designed in order to achieve coaxial to waveguide transition. Finally, some other LWA arrangements rooted in the same concept are shown.

4.1 Proposed Unit Cell and analysis

In the design of periodic LWAs, two primary challenges need to be addressed: the occurrence of an open stopband, which degrades the radiated beam around broadside, and the emergence of grating lobes in the radiation pattern. When dealing with periodic structures filled with dielectric material, the typical concern of grating lobes may not apply provided that the dielectric material sufficiently slows the wave, enabling the scanning with the presence of a single spatial harmonic. Various techniques have been proposed for eliminating the open stopband in such structures [1]-[7]. In [1], the approach involves the use of two non-identical slots within each unit cell in order to eliminate the OSB. This novel design achieves to mitigate the OSB. Meanwhile, [2] introduces a design combining dispersion enhancement and meandered unit

cells, demonstrating successful outcomes in OSB mitigation. In [7] is proposed a novel design for a LWA in the form of a half-annular structure with suppressed OSB and integrated feeding. The technique employed to eliminate the OSB involves the use of asymmetric unit cells. These techniques, when applied to dielectric-filled LWAs, have successfully mitigated or even eliminated the open stopband (OSB). Nevertheless, when dealing with air-filled structures, a distinct approach is often required.

Air-filled waveguide based periodic LWAs are a good option for scanning applications where high-power handling capability, low loss, good stability, and reliability is required [8]-[9]. One of the common techniques to eliminate or at least reducing the open stopband is to load the waveguide with two radiating elements per unit cell at a distance $\lambda_g/4$ (λ_g being the guided wavelength at the broadside frequency) [10]. Commonly used techniques to eliminate the grating lobes are reducing the interelement spacing [11] or using spatial filters [12]-[13]. The serpentine arrangement in rectangular waveguide technology is a good candidate for backward to forward radiation capability, to avoid grating lobes and to eliminate the OSB [14]. In these configurations, a waveguide is typically loaded with longitudinal radiating slots placed in the narrow wall of the waveguide. However, this results in a LWA with large lateral profile that hinders the possibility to place several of them side-by-side for the implementation of an array antenna [14]-[15].

The proposed structure is based on a serpentine rectangular waveguide loaded with transverse, non-resonant, radiating slots in the wide wall.

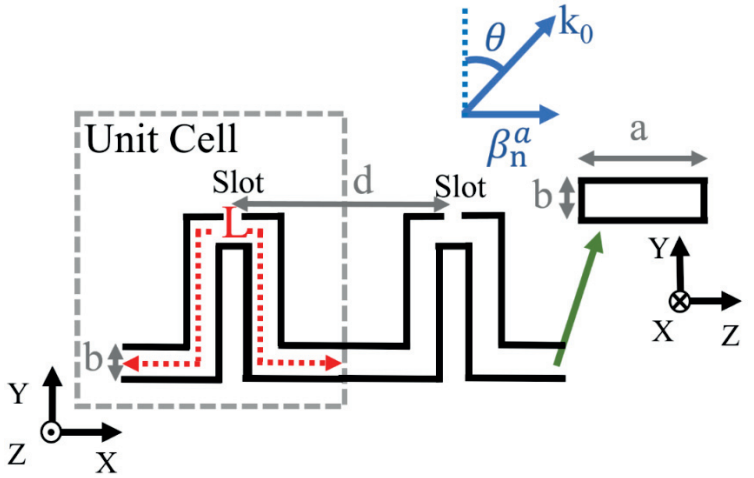


Figure 4.1. Sketch of a serpentine waveguide-based LWA.

As can be seen in Figure 4.1, the distance between two consecutive slots corresponds to the length of the unit cell d. The dimensions of the waveguide walls a and b will define the cutoff frequency of each mode. In a rectangular waveguide, the cutoff frequency is defined by:

$$f_c = \frac{c}{\sqrt{\varepsilon_r \mu_r}} \sqrt{\left(\frac{m}{2a}\right)^2 + \left(\frac{n}{2b}\right)^2} \tag{4.1}$$

Where ε_r and μ_r are the relative permittivity and the relative permeability respectively, m and n are the modes of the propagating wave, and c the speed of light. According to the Floquet's theorem [14], the propagating mode inside the proposed periodic structure can be decomposed into an infinite number of space harmonics. The phase constant of each of the nth space harmonics can be written as

$$\beta_n = \beta + \frac{2\pi n}{L} \tag{4.2}$$

where β is the phase constant of the fundamental ($n = 0$) space harmonic that approaches the phase constant of the closed waveguide (i.e., when the loading tends to zero) and L is the meandered length of a unit cell. As it is known, the illumination of the near fields determines the far field radiation pattern [11]. The fields on the radiating aperture of the structure shown in Figure 4.1 are characterized by a phase constant which, for the nth space harmonic, is given by

$$\beta_n^a = \frac{L}{d}\beta_n \tag{4.3}$$

Thus, the phase constant of the aperture fields is increased by a factor of L/d with respect to the fields inside the waveguide. Radiation will occur provided that one of the space harmonics on the aperture is a fast wave or, equivalently, lies within the radiation cone of the Brillouin diagram. Considering the serpentine waveguide shown in Figure 4.1 with dimensions $a = 60$ mm, $b = 3.1$ mm, $L = 74$ mm, $d = 19.42$ mm, which leads to the increasing factor $L/d = 3.81$. Assuming the propagation of the TE_{10} mode, the analytical dispersion diagram for the space harmonics inside the waveguide and

on the aperture are shown in Fig.4.2 and Fig.4.3, according to (4.2) and (4.3) respectively.

It can be seen in Figure 4.2 that none of the space harmonics inside the waveguide pass completely through the edges of the radiation region. Notice that the $n = 0$ space harmonic tends asymptotically to the positive edge of the radiation cone. However, the space harmonics $n < 0$ on the aperture completely cross the cone edges as shown in Figure 4.3. Flatter curves can be obtained by increasing the value of L/d, so that the frequency variation for scanning from backward to forward end-fire becomes smaller.

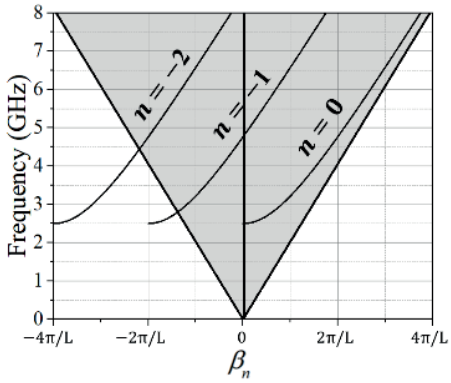


Figure 4.2. Dispersion diagram for the space harmonics inside the air-filled serpentine waveguide. The radiation region is highlighted in gray.

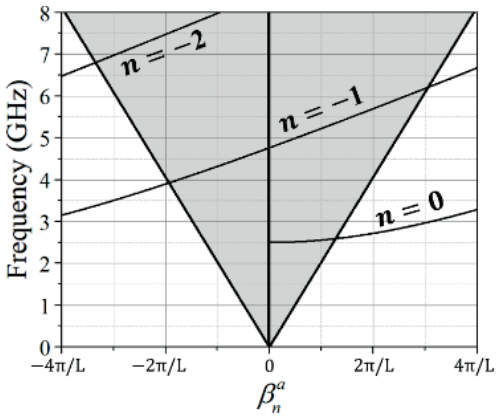


Figure 4.3. Dispersion diagram for the scape harmonics on the aperture. The radiation region is highlighted in gray.

Notice that the space harmonic on the aperture capable of scanning with the lowest frequency variation is the $n = -1$. The angle θ (measured from the

y-axis, within the y-x plane, according to Fig.4.1) of the main radiated beam due to this space harmonic can be obtained from [10]

$$Sin(\theta) = \frac{\beta_{-1}^{a}}{k} \tag{4.4}$$

To have single-beam scanning over the entire range (i.e., only the $n = -1$ space harmonic radiates), the presence of unwanted space harmonics within the radiation region that would produce grating lobes must be avoided. Thus, both the $n = 0$ and $n = -2$ space harmonics on the aperture must remain a slow wave as the -1 space harmonic is scanned from backfire to end-fire. This requires that the difference between the effective phase constants β_{-1}^{a} and β_{-2}^{a} must be greater than $2k$ at the highest frequency of the scan range (forward end-fire). As it can be inferred from (4.2), this condition is equivalent to the design constraint that $d < \lambda_0/2$ (λ_0 being the free-space wavelength) at the highest frequency [16] or, equivalently, the phase velocity must be made sufficiently slow such that $v_{-1}^{a} < c/3$ [14].

Figure 4.4 shows a unit cell with transverse slots on the wide wall, designed to achieve broadside radiation at 5GHz. The dimensions of the unit cell are $L = 67.7$ mm, $d = 19.42$ mm, $a = 60$ mm, $b = 3.1$ mm, with slot dimensions $l_s = 0.7$ mm and $w_s = 20$ mm. These slots are non-resonant, as the width and the length are smaller than $\lambda_g/2$ [10], [17]. Figure 4.5 illustrates the effective phase constant of the space harmonic $n - 1$ of the unit cell. To extract this value, CST Studio 2014 simulator was used to obtain the phase of the transmission coefficient of a unit cell in perfect matching condition. Finally, this value was substituted as $\beta_n L$ in Equation (4.3).

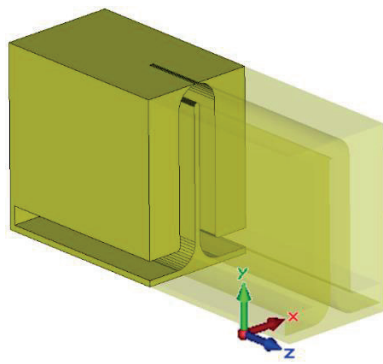


Figure 4.4. First proposed Unit Cell.

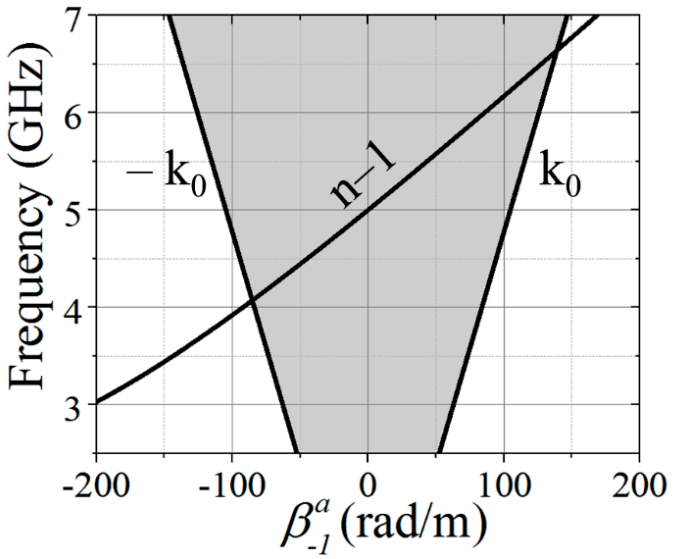


Figure 4.5. Dispersion diagram for the scape harmonic $n{-}1$ on the aperture. The radiation region is highlighted in gray.

In the following images (Figure 4.6 and Figure 4.7), the reflection coefficient is shown for 5 unit cells and 30 unit cells, the field distribution in absolute value at 5 GHz, and the field distribution in absolute value at 4.5 GHz for an antenna composed of 30 unit cells.

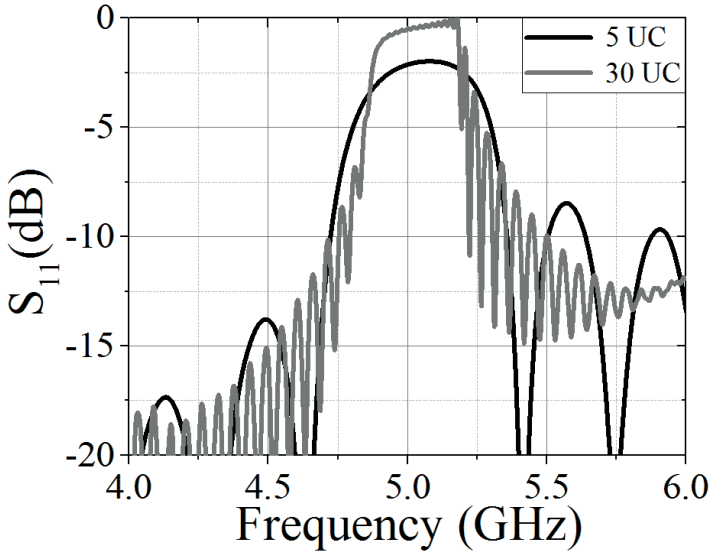
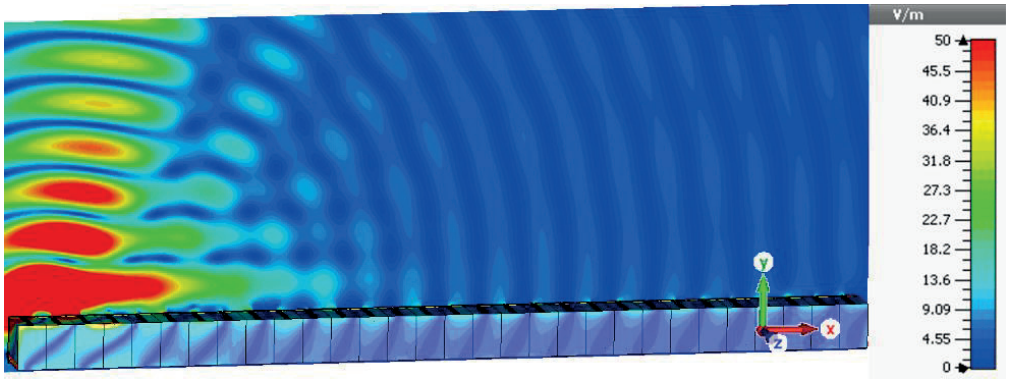
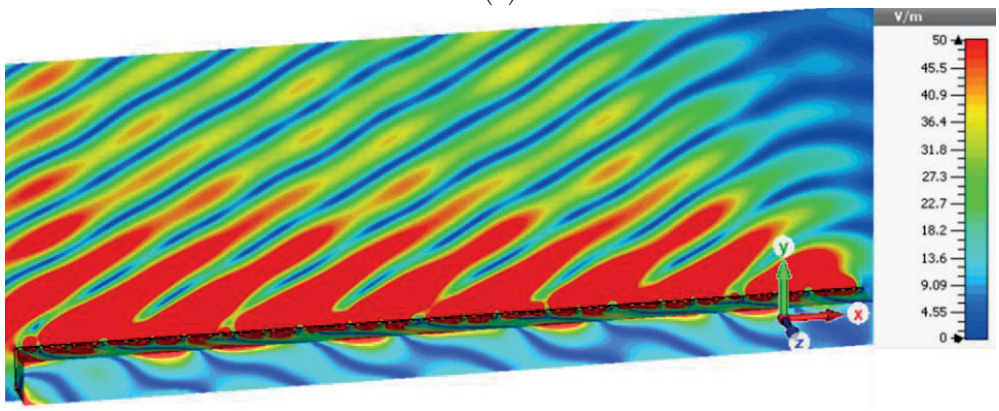


Figure 4.6. Reflection coefficient (black line represents the simulated results with 5 UC, while dark grey corresponds to 30 UC).

As observed, at the operational frequency where the beam steers in the broadside direction, the OSB emerges, becoming more pronounced when considering a higher number of unit cells.



(a)



(b)

Figure 4.7. Field distribution around the LWA composed by 30 UC under perfect matching condition. (a) 5 GHz. (b) 4.5 GHz.

In Figure 4.7, it can be seen that the electric field stops propagating through the structure within this region. It can also be observed that some residual radiation occurs due to the transition between the reflected and transmitted signal. However, the gain of the antenna remains under 2 dB. On the other hand, outside of the OSB region, the antenna radiates as expected, offering a maximum gain of 16.6 dB.

The appearance of the open stopband in periodic structures is associated with a significant amount of power from the wave travelling along the structure being reflected back to the source, rather than radiated, producing large

mismatch. As the number of unit cells increase, or the radiated power increases, the mismatch produced by the stopband [10]-[11] as shown in Figure 4.6. Typically, this problem is solved loading the unit cell with a second element located $\lambda_g/4$ apart from the radiating element. However, this approach usually only mitigates the OSB region.

Considering radiation from the $n = -1$ space harmonic, it follows from (4.4) that $\beta_{-1}^{a} = 0$ at the broadside radiation and $\beta_0 L = 2\pi$, according to (4.3). To prevent the open stopband for the $n = -1$ space harmonic, each unit cell will be load with two identical slots, one of them placed in the top wall of the waveguide (Slot_A) and the other in the bottom wall (Slot_B), as shown in Fig. 4.8.

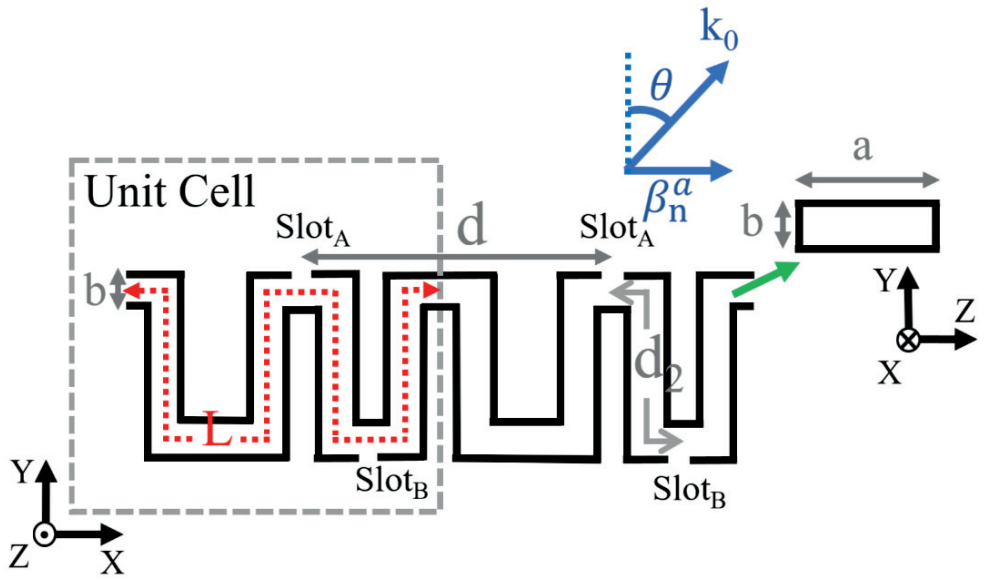


Figure 4.8. Sketch of the proposed unit cell. © 2023 IEEE. Reprinted, with permission, from [18].

Notice that this configuration will produce bidirectional radiation pattern, which may be desirable in specific applications where areas with limited space need to offer a wide coverage in wireless communications such as tunnels, long streets, or coal mines [19]-[21]. The radiating slots can be modelled using the single-element impedance representation provided that the slots width is small compared with the slots length and slot lengths are less than $\lambda_g/2$. Since the top and bottom slots are both identical and are designed to be non-resonant, they can be represented by a resistance in series with a reactance [17], [22].

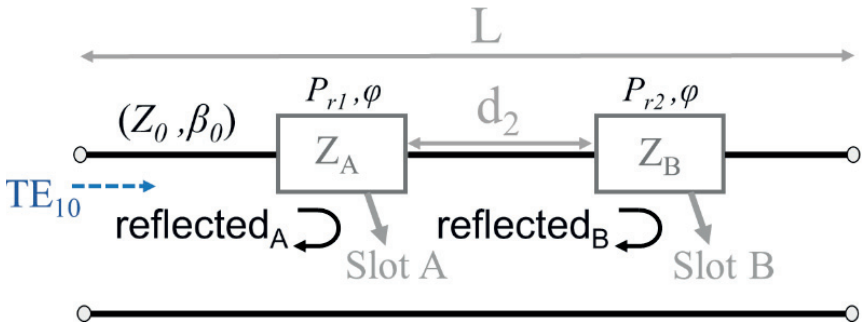


Figure 4.9. Equivalent circuit of the unit cell. © 2023 IEEE. Reprinted, with permission, from [18].

The resistance accounts for the radiated power through the slot and the reactance correspond to the reactive power. In order to avoid the wave being reflected to the source, the bottom slots must be located at a specific distance, d_2 (see Fig.4.9), from the top slot so that at the beginning of the unit cell reflection from the top and bottom slots are 180º out-of-phase. Let us consider that only the fundamental TE_{10} mode (slightly perturbed by the presence of the slots) propagates inside the waveguide with a phase constant β_0. Assuming that the reflection coefficient at the top and bottom slots are equal each other, the difference in phase delay at the beginning of the unit cell for the waves reflected at both slots will differ in two times the round-trip phase delay between the two elements, i.e., $-2\beta_0 d_2$, plus two times the additional phase, φ, due to the wave going through the top slot, which leads to

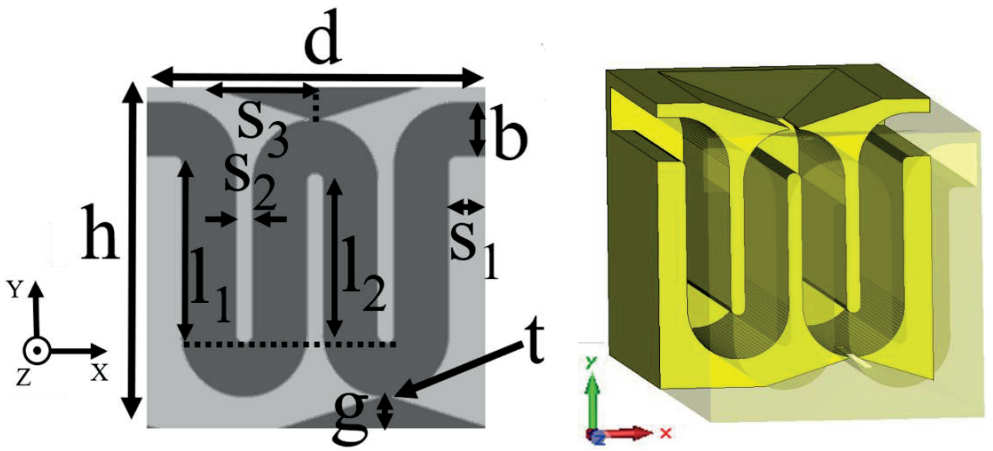
$$d_2 = \frac{\lambda_0}{4}\left(1 + \frac{2\varphi}{\pi}\right) \tag{4.5}$$

where λ_0 corresponds to the free-space wavelength at the broadside frequency. The phase φ introduced by a single slot can be obtained from electromagnetic simulation, by comparing the phase of the S_{21} parameter of the unit cell in the case of considering only one slot and without slots, under perfect matching condition.

4.2 Design of the Leaky Wave Antenna

The proposed LWA is designed for an emerging broadside beam at 5 GHz from the $n = -1$ space harmonic. The layout of the unit cell for the proposed

LWA is shown in Fig.4.10 In order to reduce the interelement spacing and prevent the appearance of grating lobes, non-standard waveguide dimensions were employed. The width of the waveguide was set to ensure the propagation of the fundamental TE_{10} mode at the operating frequency range. The narrow wall was designed to reduce the distance between slots. The dimensions of the rectangular slots ($l_s = 0.7$mm and $w_s = 20$ mm) were chosen to achieve maximum radiation resistance, comply with manufacturer's specifications, and avoid slot resonance. Once the slot dimensions were chosen, the amount of power radiated per unit cell can be controlled with the slot thickness, t. Making it lower increases the leakage rate with a minimum change in the phase constant of the guided wave. A dimensioned ramp hole (related to the parameter s_3) was used to set the slot thickness to 0.1 mm, as the manufacturer's specifications required a minimum wall width of 2 mm.



(a) (b)

Figure 4.10 (a) Unit cell cross section layout. Metallization is highlighted in light gray and the absence of metallization in dark gray. Dimensions are: a = 60 mm, b = 3.1 mm, d = 19.42 mm, h= 20.2 mm, l_1 = 11 mm, l_2 = 10, s_1 = 2.01mm, s_2 = 1 mm, s_3 = 20.35 mm, g = 2 mm, t = 0.1 mm. © 2023 IEEE. Reprinted, with permission, from [18]. (b) 3D view of the proposed unit cell.

To obtain the serpentine length of a unit cell L, and the distance between two consecutive slots, d_2, the following steps were taken. First, the meandered length L was set to $\lambda_g = 6.92$ cm, which corresponds to the guide wavelength evaluated at the broadside frequency of 5 GHz. Next, as is shown in Fig.4.11 the phase $\varphi = -0.19$ rad (-11^o) was obtained from electromagnetic simulation

of the unit cell under perfect matching condition, by subtracting the phase of the S_{21} parameter without slot to the S_{21} parameter with one slot at 5 GHz. Finally, the bottom slot was placed at a distance $d_2 = 15.2$ mm, calculated using (4.5), from the top slot and the meandered length L was modified to ensure that the phase of the S_{21} parameter equals -2π at the broadside frequency.

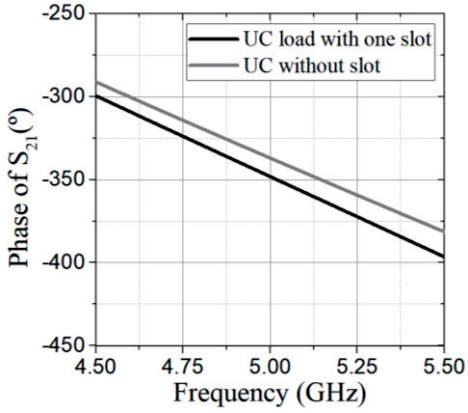


Fig. 4.11 Phase of the transmission coefficient of a unit cell under perfect matching condition (black line represents the UC loaded with 1 slot, while dark grey corresponds to the UC without slot). © 2023 IEEE. Reprinted, with permission, from [18].

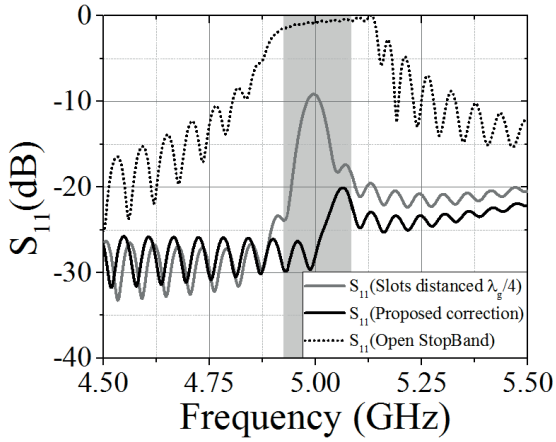


Figure 4.12 Comparison of 30-UC under perfect match simulation S-parameters (black line represents the results applying equation 3, dark grey corresponds to the slots separated by $\lambda_g/4$ and black dotted line represents the design with OSB). Light grey indicates the open stopband region. © 2023 IEEE. Reprinted, with permission, from [18].

As observed in Figure 4.12, the application of the proposed correction successfully eliminates the OSB, resulting in a reduction of reflected power by over 15 dB compared to the most common method.

For the design of the unidirectional version, two options were explored: one using a rectangular cavity (Fig.4.13) and the other employing a ground plane (Fig.4.14) [23].

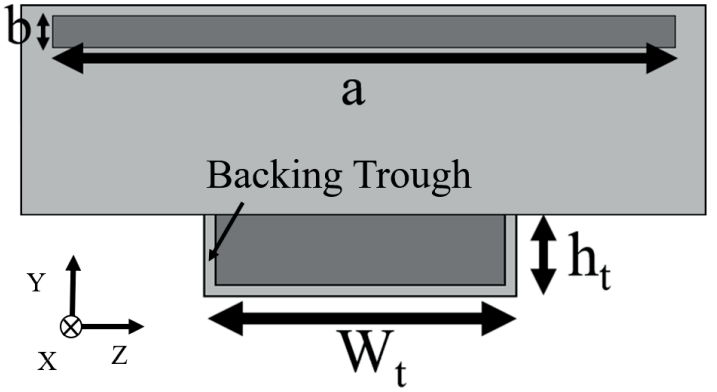


Figure 4.13 Schematic of the unidirectional version based on backing trough. Metallization is highlighted in light gray and the absence of metallization in dark gray. © 2023 IEEE. Reprinted, with permission, from [18].

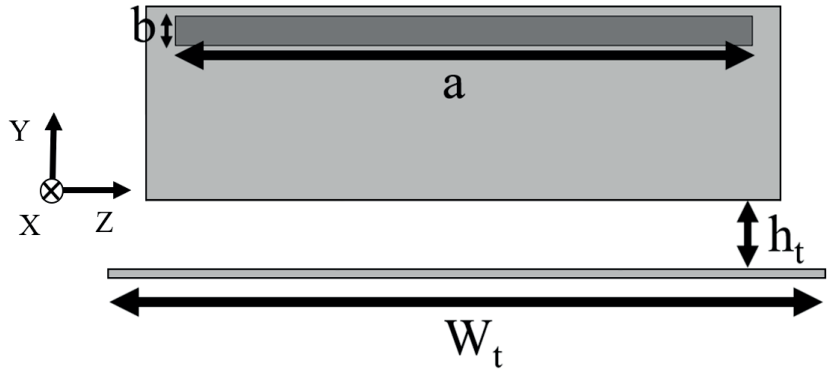


Figure 4.14 Schematic of the unidirectional version based on ground plane. Metallization is highlighted in light gray and the absence of metallization in dark gray.

The first technique involves a long metallic cavity that can be thought as a waveguide operating well below the cutoff frequency of the first dominant mode. This ensures the elimination of transverse resonances. Moreover, since most of the power is radiated from the structure before it reaches the open end

of the metallic cavity, any longitudinal resonances are effectively eliminated. Then, to prevent excitation of the dominant TE_{10} mode, the width and height of the metal cavity must satisfy the condition

$$w_t < \frac{c}{2f_h} \qquad h_t < \frac{c}{2f_h} \tag{4.6}$$

where f_h is the highest scan frequency, which in this case is 6 GHz. Typically, the most efficient distance of the cavity from the surface is $\lambda_g/4$. On the other hand, for the cavity width, it should be at least as large as the slots.

The second technique involves placing a ground plane parallel to the slots at a distance h_t. In this case, the most efficient distance from the device's surface is $h_t = \lambda_0/4$, while the width must be at least as large as the aperture. Simulation software was employed to analyze the impact of these techniques on the OSB region. Next, a comparison of the S parameters for the optimized designs of the two unidirectional versions is presented.

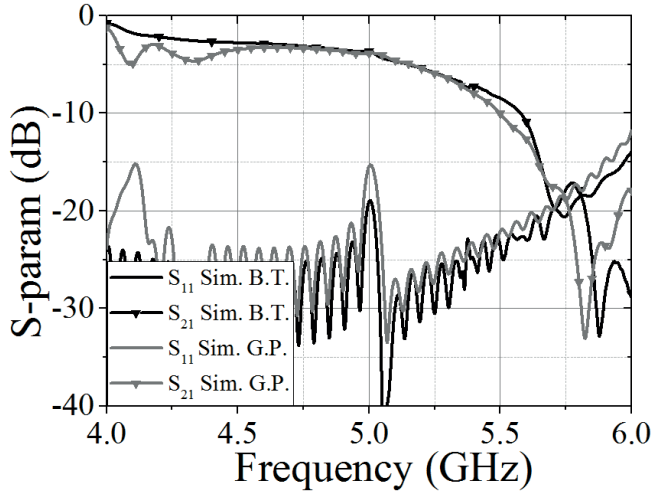


Figure 4.15 Comparison of 30-UC under perfect match simulation S-parameters (the black line represents results with the backing, while dark grey corresponds to results with the ground plane).

In both cases, optimization was carried out through a parameter sweep in CST under perfect matching conditions. The simulations were conducted on a structure composed of 30 UCs. The optimized values used in Figure 4.15 were $h_t = 22$ mm and $w_t = 27$ mm for the backing through design, and $h_t = 16$ mm and $w_t = 90$ for the ground plane-based design. For the backing through design,

it was observed that beyond a distance of 18 mm (0.26 λ_g) from the surface, the structure's effect on OSB suppression was minimal, while the cavity width was crucial. The wider the cavity [complying with condition (4.6)]), the less affect it on OSB suppression. On the other hand, in the case of the ground plane design, the critical parameter was the distance from the surface. The reflection losses in the version with a rectangular cavity are -19 dB, while for the ground plane design, they are -15 dB at the frequency corresponding to broadside radiation. Also, it can be observed that both configurations dissipate approximately the same amount of power. Furthermore, in general, both designs exhibited the same radiation efficiency and identical gain. Furthermore, the waveguide cavity-based design offers a much more compact arrangement. For these reasons, the unidirectional design carried out was with a rectangular cavity.

To power the structure, a matching network must be designed. Waveguides derive their energy by exciting an electric or magnetic field within the structure. This excitation can be achieved through options such as a probe, a loop antenna, or a patch antenna, among other planar elements inserted into the waveguide [10], [24]-[25]. There are proposed in-line transitions based on microstrip or substrate-integrated waveguide to waveguide [26]-[29]. However, these latter types of feed structures require dielectric materials, leading to increased losses and impacting the high-power handling capacity that air-filled waveguides typically offer [8]-[9], [30]. Alternatively, a waveguide can be powered by coupled slots [31]-[32]. In this case, the signal should be generated using one of the methods mentioned above. The choice between these methods depends on the specific design requirements.

The most used technique in rectangular waveguide is based on a small probe inserted into the waveguide and supplied with a coaxial cable. By coupling the probe into the waveguide, the current that flows into the probe at first produces and E field which causes an H field, then the stablished electromagnetic field is transmitted through the waveguide. In the opposite way, energy can be removed from a waveguide using the same technique. To set up an electric field of considerable intensity inside the waveguide, the probe must be placed at the point of maximum efficiency. Normally, in rectangular waveguide, the most efficient place to locate the prove is in the center of the wide wall, distanced $\lambda_g/4$ to the shorted end of the waveguide and parallel to the narrow wall with

a length of $\lambda_0/4$ [10]-[33]. Another way to power a waveguide is to inject the energy through a small loop that will carry a high current. In this case, the energy will be injected into the waveguide by coupling the small loop generating a magnetic field that will cause the appearance of an electric field. Only if the frequency of the current in the loop is within the bandwidth of the waveguide, energy will be transferred to the waveguide.

Since this structure will be analyzed as an electromagnetic field confinement device for high power applications, the transition was based on a small probe inserted into the waveguide, facilitated by a commercial SMA connector. The waveguide hight required to the signal excitation is higher than the wide wall of the unit cell. To achieve this transition a matching network based on stepped impedance and tapered transition was designed, as illustrated in Fig.4.16 [34]-[35]. The parameters were optimized by means of CST Studio 2014 under perfect matching conditions to ensure enough transmission power from 4.2 to 6 GHz. The material used for the waveguide structure was aluminum ($\sigma = 3.56 \cdot 10^7$ m/s). To model the dielectric surrounding the inner conductor of the coaxial cable, Rogers RT5870 ($\varepsilon_r = 2.33$, $\tan\delta = 0.0012$) was used. To carry out the simulations, two waveguide ports was used. The first one was placed in the coaxial, and the second one was positioned at the end of the waveguide transition (corresponding with the narrow wall b).

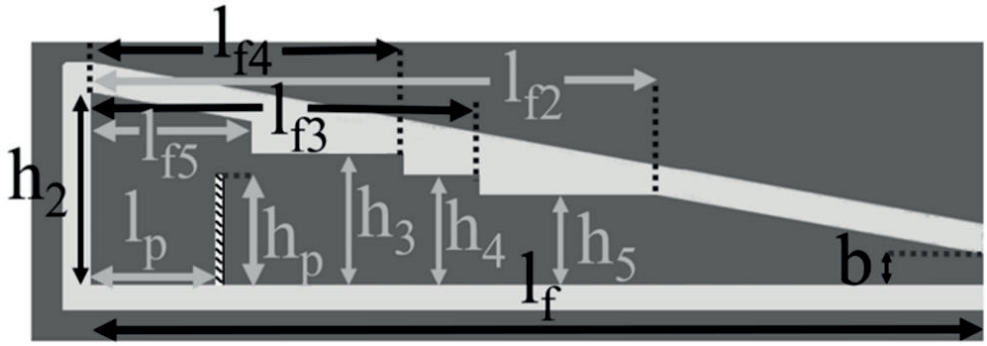


Figure 4.16 Layout of the matching network. Metallization is highlighted in light gray and the absence of metallization in dark gray. Dimensions are: a = 60 mm, b = 3.1 mm, h_2 = 19 mm, h_p = 13 mm, h_3 = 13 mm, h_4 = 11 mm, h_5 = 9 mm, l_f = 89 mm, l_{f2} = 55.4 mm, l_{f3} = 38.5 mm, l_{f4} = 31 mm, l_{f5} = 16 mm, l_p = 10.5 mm. © 2023 IEEE. Reprinted, with permission, from [18].

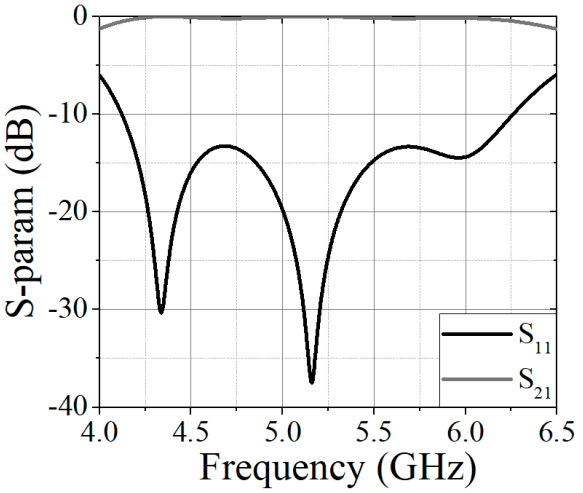


Figure 4.17 S-Parameters of the matching network.

As seen in Figure 4.17, reflection losses below -10 dB were achieved within the frequency operation band. Additionally, at the frequency where the structure radiates in the broadside direction, reflection losses are below -20 dB, indicating that over 99% of the power is transmitted to the periodic structure.

Considering that this structure will be analyzed in the surface wave mode, to implement an EMFCD in Chapter 5, the matching network was designed to be modular, separate from the unit cells. Furthermore, the structure composed by 30 UC was divided into two parts. The following illustrates the design of the matching network and the unit cells with the relevant modifications to enable their fabrication.

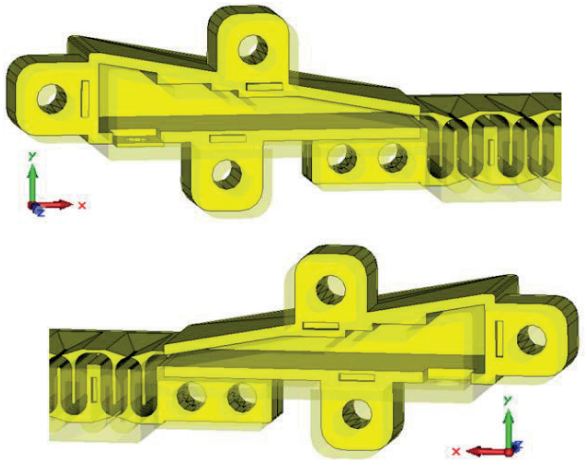


Figure 4.18 Designed modulated matching network prototype.

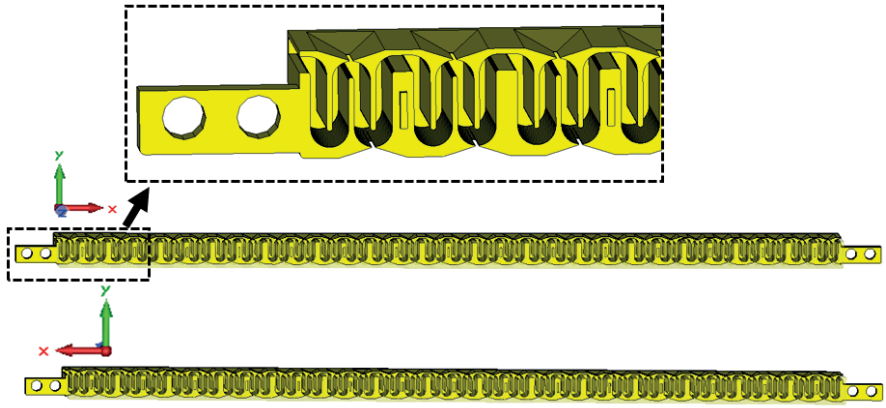


Figure 4.19 Design of the periodic structure.

4.3 Fabrication and experimental results

As indicated in the previous chapter, an attempt was made to manufacture the device using 3D printing, but this was not successful. Finally, the design was outsourced to a company external to the Universitat Autònoma de Barcelona. The prototype was produced using computer numerical control (CNC) machining, following the design shown in Figures 4.18-4.19. The material used was 6063 aluminum comprised of approximately 98% aluminum and 2% other metals such as copper and magnesium. The probe inserted into the waveguide was a commercial SMA connector (RS pro straight panel mount SMA connector, jack, solder termination, RS Stock No: 546-3181). The inner conductor of this connector was modified according to the dimensions of Figure 4.16. The backing trough was fabricated in PLA using 3D printing and was metallized with aluminum adhesive tape.

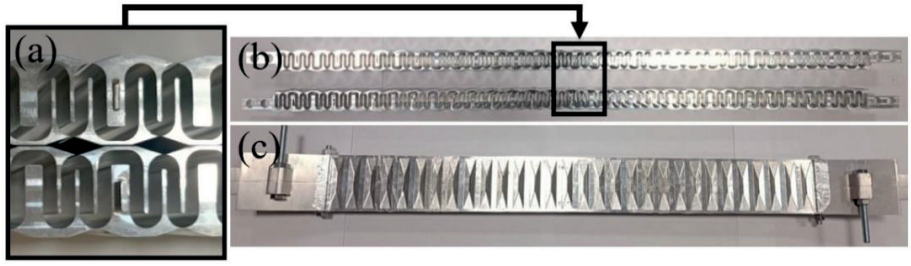


Figure 4.20 Fabricated prototype. (a) Cross-sectional zoom view of the serpentine in the *xy*-plane according to Fig. 1. (b) Cross-sectional view of the total serpentine length in the *xy*-plane. (c) Full view of the device in the *xz*-plane. © 2023 IEEE. Reprinted, with permission, from [18].



Figure 4.21 Full view of the waveguide cavity and the unidirectional LWA arrangement.

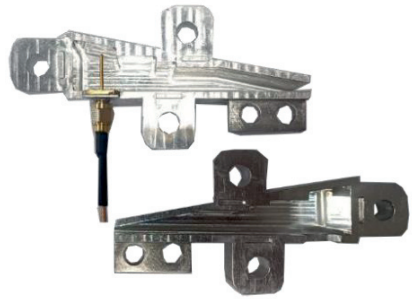


Figure 4.22 Fabricated matching network prototype.

To obtain the experimental S-parameters, a PNA Network Analyzer N5221A was used. The structure was connected through a coaxial cable and terminated with a load of 50 Ω. The measured S-parameters of the same structure considering the bidirectional antenna, unidirectional version and only the top slots (by covering the bottom slots with aluminium adhesive tape) was made for comparison purposes.

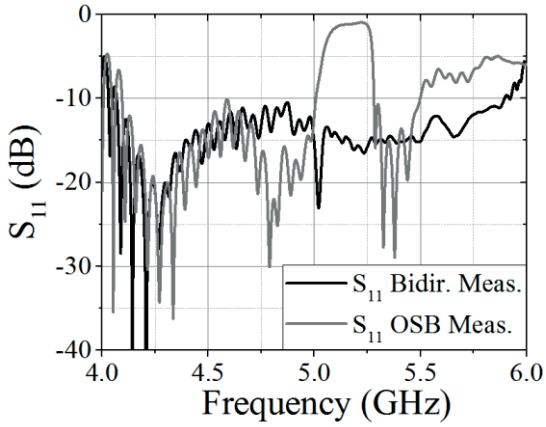


Figure 4.23 Measured reflection coefficient of the LWA (black line represents the bidirectional configuration, while dark grey line corresponds to bottom slots covered with aluminum adhesive).

In the case of considering only the top slots, an open stopband appears in the form of a strong mismatch of about 200 MHz bandwidth around the broadside frequency, just above 5 GHz. However, when both the top and bottom slots are considered the open stop band is eliminated and the matching level is reduced below −20 dB at the broadside frequency. A slight shift towards higher frequencies is obtained for the structure with only top slots due to the lack of the phase advance from bottom slots.

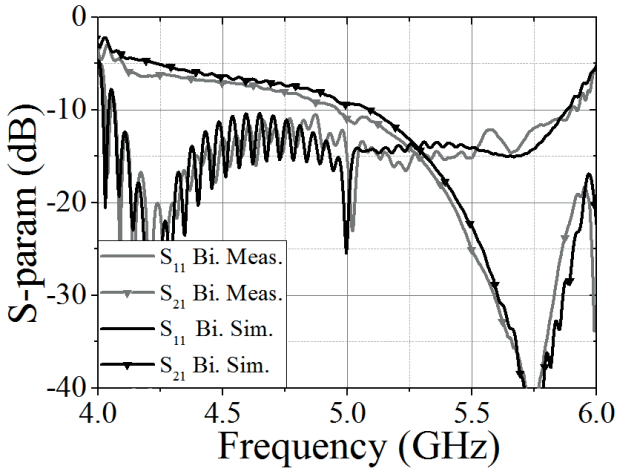


Figure 4.24 Measured and simulated S-parameters of the bidirectional arrangement (the black line corresponds to simulated results, while the dark grey line represents experimental results).

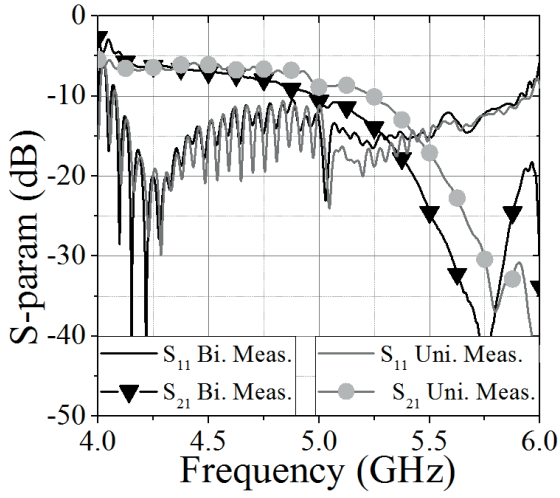


Figure 4.25 Comparison of measured S-parameters (the black line corresponds to simulated results, while the dark grey line represents experimental results).

The Figure 4.24 display a comparison between simulated and measured results of the S parameters for the bidirectional arrangement. As observed, there is a strong agreement between experimental and simulated outcomes. Additionally, in Figure 4.25, a comparison is made between experimental results of the bidirectional configuration and the unidirectional version based on backing through. It can be noticed that the presence of the backing trough does not induce significant changes in the reflection coefficient. At the frequency of broadside radiation, a matching level below −20 dB is achieved. This suggests that the suppression of the OSB through the slots on the bottom surface is still effective. However, it can be observed that the unidirectional design dissipates less power. This is because the backing through collects the energy that the slots should radiate from the bottom surface and redirects it to the top slots, but not all of it is radiated so finally is dissipated in the load.

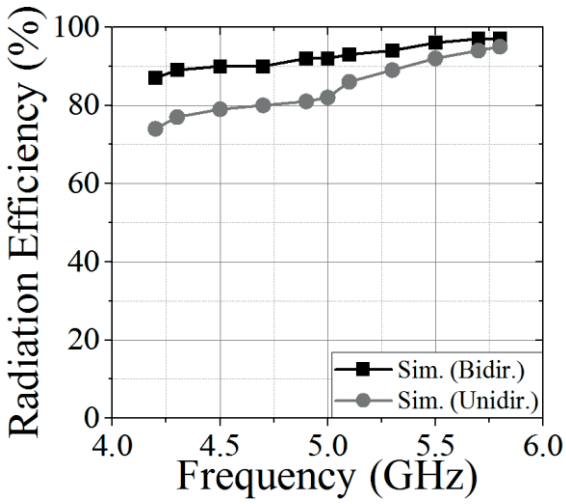


Figure 4.26 Simulated radiation efficiency (the black lines corresponds to bidirectional arrangement, while the dark grey line represents unidirectional version).

The simulated radiation efficiency ranges from 83% to 97% for the bidirectional structure and from 72% to 93% for the unidirectional version. To validate the beam-steering characteristics of the LWA, a far-field measurement system is used. The measurement setup consists of an Agilent E8364B PNA series 2-port network analyzer and a characterized horn antenna as reference antenna. Figure 4.27 shows the unidirectional LWA in the anechoic chamber. To facilitate the measurement, a support capable of withstanding the weight of

the antenna and integrating with the rotating platform was fabricated using 3D printing.

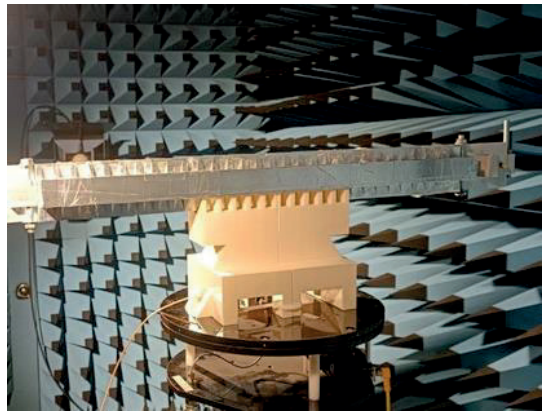


Figure 4.27 LWA and far-field measurement setup.

The following image displays the scan angle of the main beam for both the unidirectional and bidirectional antennas, along with the theoretical radiation angle.

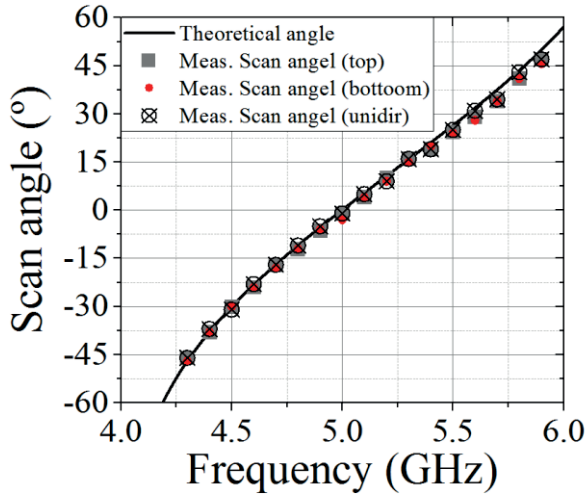


Figure 4.28 Scan angel (red dots and grey squares represent the bottom and top surfaces, respectively, in the bidirectional arrangement. A crossed-out circle indicates the unidirectional results, while a black line represents the theoretical).

To calculate the theoretical scan angle, equation (4.4) was used substituting $\beta_{n-1}L$ with the phase of the transmission coefficient of a unit cell under perfect matching condition. It can be appreciated that very good matching is achieved showing a linear dependence of the radiation angle and the frequency. This

linearity is useful for applications like frequency-scanned frequency-modulated continuous wave (FMCW) radars [15] among other scanning systems [36]. Examining (4.4) reveals a trade-off between the scan rate, calculated as the frequency derivative of the beam angle radiation, and the scanning linearity, deduced as the second frequency derivative of the beam angle (see appendix I). These quantities, when evaluated at the broadside frequency, demonstrate inverse and direct proportionality relationships with the period d, respectively. By controlling this parameter, one can adjust the scan rate and the scan linearity of the structure. As the frequency sweeps from 4.3 to 5.7 GHz, the main beam steers from $-35°$ to $42°$ in both structures, with the beam directed to broadside at 5 GHz. The measured gains for both unidirectional and bidirectional versions are depicted in Figure 4.29 showing a maximum value of 16.5 dB and 15.5 dB, respectively. The structure with a bidirectional pattern exhibits a difference between top and bottom gains, particularly in broadside radiation. This disparity in broadside radiation is primarily attributed to the open stop band phenomenon. In the rest of the scan direction, it is mainly ascribed to the dimensions of the top and bottom slots due to manufacturing tolerances. As expected, an increase on the gain (of 2 dB average) was observed for the unidirectional antenna compared to the bidirectional one, which shows that most of the back radiation is recovered by the backing trough.

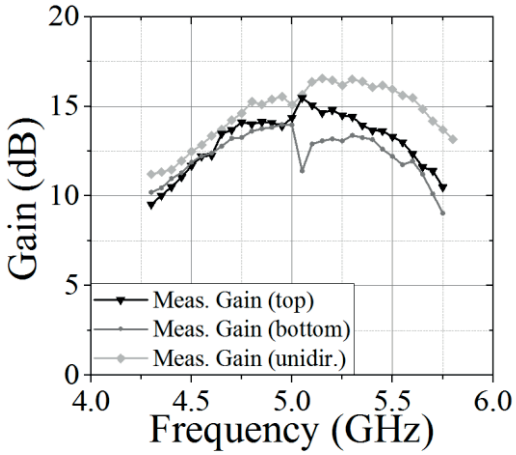
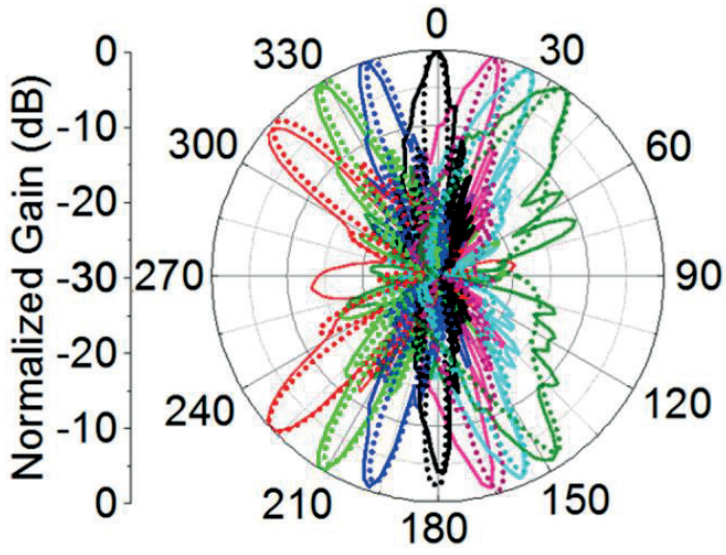
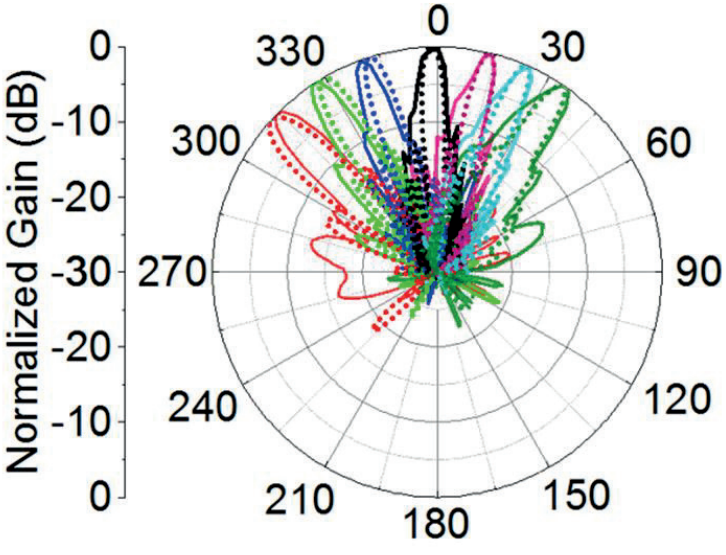


Figure 4.29 Measured gain (the black line represents the top surface, dark gray corresponds to the bottom surface, and light gray indicates the unidirectional arrangement.).



(a)



(b)

Figure 4.31 Normalized measured (solid lines) and simulated (dotted lines) radiation pattern in the E plane for (a) the bidirectional LWA and (b) the unidirectional version. The considered frequencies are 4.3 GHz (red), 4.5 GHz (light green), 4.7 GHz (dark blue), 5 GHz (black), 5.3 GHz (magenta), 5.5 GHz (cyan), and 5.7 GHz (dark green). © 2023 IEEE. Reprinted, with permission, from [18].

The simulated and measured normalized radiation patterns in the E-plane demonstrate good agreement for both the bidirectional structure and the

unidirectional version. Secondary lobes around -13 dB can be observed in relation to the main lobe in all beams. This lobe level aligns with a uniform distribution of the aperture, as anticipated due to the identical nature of all slots. In the unidirectional scenario, one can observe how the rectangular cavity efficiently redirects the energy from the slots, transitioning it from the bottom surface to the top surface.

4.4 Conclusions

In this chapter, a novel periodic leaky-wave antenna with backward to forward scanning capability is presented. The proposed structure, composed of 30 UCs, achieve an effective suppression of the open stopband for efficient broadside radiation at 5 GHz without any grating lobes. Furthermore, two unidirectional versions are analyzed. The rectangular cavity-based design exhibited superior performance compared to the ground plane-based design in dealing with the open stopband region. Additionally, the rectangular cavity design provides a more compact device.

The measured and simulated S-parameters, radiation pattern, and gain are reported for the unidirectional arrangement based on backing trough and the bidirectional structure.

In Table 4.1 a frequency scan antenna features comparison is shown. In this table, the open stopband is considered as rejected with a matching level under - 10 dB at broadside frequency radiation. This antenna can be configured with a bidirectional radiation pattern and a unidirectional radiation pattern.

In [35] a LWA based on fully metallic corrugated parallel-plate waveguide (PPW) technology is proposed. The antenna design includes a corrugated plate, a smooth plate, and a feeding structure with wideband impedance matching. The study addresses challenges such as the open stopband effect and proposes solutions, such as introducing two no-identical elements within a radiating unit. However, the OSB is mitigated but not eliminated. In [12], a serpentine waveguide structure, loaded with slots along its broad wall, was employed to feed an array of patch antennas. The study successfully suppressed the open stopband by introducing reflection cancellation pillars with optimized size and placement relative to the slot. Despite this achievement, the presence of grating lobes was inevitable due to constraints on the width of the serpentine

waveguide's broad wall. Moreover, the presence of pillars, introduce Ohmic losses, reducing the radiation efficiency. In [15], a waveguide antenna design was introduced, allowing for a side-by-side arrangement of multiple antennas due to its narrower width. This design incorporated cylindrical posts positioned at the center of the waveguide, resulting in a modest reduction of the open stopband. The study demonstrated the absence of grating lobes, except for a minor back-lobe near the cut-off frequency. However, the presence of these cylindrical posts led to a notable dissipation of power through Ohmic loss, thereby decreasing the overall radiation efficiency. The design presented in [37] involves using a CRLH waveguide with air-filled double ridge corrugations (DRCs). The unit cell of the waveguide consists of a traditional rectangular waveguide with one broad wall periodically loaded with air-filled short-circuited DRCs. This structure supports both forward and backward wave propagation simultaneously. However, the proposed unit cell do not eliminate the OSB, only managing to mitigate it to -7.5 dB. Additionally, the radiation efficiency and scan linearity is relatively low.

The proposed structure in this thesis, in both versions, achieves a high-power handling capability, high frequency scan range with a linear scan variation, high radiation efficiency, high gain, low loss, and good stability and reliability. The geometrical arrangement has a narrower lateral profile, which allows placing several of them side-by-side to either and obtain a pencil beam. The experimental results show a backward to forward scanning capability from $-35°$ to $42°$ for both the unidirectional and bidirectional versions, with a maximum measured gain of 15.5 dB and 16.5 dB, respectively.

Table 4.1. Performance comparison with other air-filled FSAs. © 2023 IEEE. Reprinted, with permission, from [18].

Ref.	Type	Bandwidth (GHz)	Radiation Eff. (%)	Scanning angle (º)	Gain (dB)	Grating lobes	OSB	Length (λ_0)
[35]	Corrugated PPW	28~40	>80	-42.5~5.5	9.1~14.1	No	Mitigated	9.4
[12]	Array antenna	230~245	60	-24~24.5	29~30	Yes	Eliminated	34
[15]	Waveguide LWA	27~34.7	54~90	-38~27	11.5~19	No	Mitigated	27.6
[30]	SSDA	9.7~10.3	<60	-23~16	12~20	No	Yes	23.3
[37]	Waveguide LWA	30.5-40	40~75	-29~31	16~19.5	No	Mitigated	31
Proposed	SSAA Bidirectional	4.3~5.7	83~97 (sim)	-42~34	10~15.5	No	Eliminated	9.7
	SSAA Unidirectional	4.3~5.7	72~93 (sim)	-43~36	11.2~16.4	No	Eliminated	9.7

REFERENCES

[1] J. Liu, et al., "A simple technique for open-stopband suppression in periodic leaky-wave antennas using two nonidentical elements per unit cell", IEEE Trans. Antennas Propag., vol. 66, no. 6, pp. 2741-2751, Jun. 2018, doi: 10.1109/TAP.2018.2819701.

[2] A. J. Mackay and G. V. Eleftheriades, "Meandered and Dispersion-Enhanced Planar Leaky-Wave Antenna With Fast Beam Scanning," in IEEE Antennas and Wireless Propagation Letters, vol. 20, no. 8, pp. 1596-1600, Aug. 2021, doi: 10.1109/LAWP.2021.3091979.

[3] S. Paulotto, et al. "A novel technique for open-stopband suppression in 1-D periodic printed leaky-wave antennas", IEEE Trans. Antennas Propag., vol. 57, no. 7, pp. 1894-1906, Jul. 2009, doi: 10.1109/TAP.2009.2019900.

[4] D. Comite et al., "A dual-layer planar leaky-wave antenna designed for linear scanning through broadside", IEEE Antennas Wireless Propag. Lett., vol. 16, pp. 1106-1110, 2016, doi: 10.1109/LAWP.2016.2639586.

[5] P. Baccarelli, et al., "Open-stopband suppression via double asymmetric discontinuities in 1-D periodic 2-D leaky-wave structures", IEEE Antennas Wireless Propag. Lett., vol. 18, no. 10, pp. 2066-2070, Oct. 2019, doi: 10.1109/LAWP.2019.2937473.

[6] X.-L. Tang, "Continuous beam steering through broadside using asymmetrically modulated Goubau line leaky-wave antennas", Sci. Rep., vol. 7, 2017, 10.1038/s41598-017-12118-8.

[7] M. Kuznetcov et al., "Half-Annular Leaky-Wave Antenna With Suppressed Open Stopband: Design and Experimental Testing," in IEEE Antennas and Wireless Propagation Letters, vol. 22, no. 5, pp. 1204-1208, May 2023, doi: 10.1109/LAWP.2023.3236614.

[8] David M. Pozar, Microwave Engineering, Hoboken, NJ :Wiley, 2012.

[9] Richard C. Johnson, Antenna Engineering Handbook, third eddition, USA, NY, New York:McGraw-Hill, 2007.

[10] J. L. Volakis, Antenna Engineering Handbook, USA, NY, New York:McGraw-Hill, 2007.

[11] C. A. Balanis, Modern Antenna Handbook, Hoboken, NJ, USA:Wiley, 2008.

[12] K. Sarabandi, A. Jam, M. Vahidpour, and J. East, "A Novel Frequency Beam-Steering Antenna Array for Submillimeter-Wave Applications," in IEEE Transactions on Terahertz Science and Technology, vol. 8, no. 6, pp. 654-665, Nov. 2018, doi: 10.1109/TTHZ.2018.2866019.

[13] Young Ju Lee, Junho Yeo, R. Mittra, and Wee Sang Park, "Application of electromagnetic bandgap (EBG) superstrates with controllable defects for a class of patch antennas as spatial angular filters," in IEEE Transactions on Antennas and Propagation, vol. 53, no. 1, pp. 224-235, Jan. 2005, doi: 10.1109/TAP.2004.840521.

[14] A. A. Oliner, "1963 Short Course on Microwave Field and Network Techniques" Brooklyn, Polytechnic Institute of Brooklyn, Tuesday, June 4, 1963.

[15] A. Ohadi and G. V. Eleftheriades, "Slotted Waveguide Frequency-Scanned Slow-Wave Antenna With Reduced Sensitivity of the Closed Stopband at Millimeter-Wave Frequencies," in IEEE Access, vol. 10, pp. 27783-27793, 2022, doi: 10.1109/ACCESS.2022.3152905.

[16] M. Guglielmi and G. Boccalone, "A novel theory for dielectric-inset waveguide leaky-wave antennas," in IEEE Transactions on Antennas and Propagation, vol. 39, no. 4, pp. 497-504, April 1991, doi: 10.1109/8.81463.

[17] Richard C. Johnson, Antenna Engineering Handbook, third eddition, USA, NY, New York:McGraw-Hill, 2007.

[18] Á. Jaque, G. Zamora and J. Bonache, "Frequency Scanning Leaky-wave Slot Antenna Array Based on Serpentine Waveguide with Open Stopband Suppression," in IEEE Antennas and Wireless Propagation Letters, doi: 10.1109/LAWP.2023.3324063.

[19] F. Ge, H. Zhao, S. Li and X. Yin, "Bidirectional Scanning Antenna Based on Surface Wave Mode," in IEEE Antennas and Wireless Propagation Letters, vol. 21, no. 8, pp. 1592-1596, Aug. 2022, doi: 10.1109/LAWP.2022.3174879.

[20] Z. L. Ma and L. J. Jiang, "One-Dimensional Triple Periodic Dual-Beam Microstrip Leaky-Wave Antenna," in IEEE Antennas and Wireless Propagation Letters, vol. 14, pp. 390-393, 2015, doi: 10.1109/LAWP.2014.2365394.

[21] L. Liu, Z. Zhang, Z. Tian and Z. Feng, "A Bidirectional Endfire Array With Compact Antenna Elements for Coal Mine/Tunnel Communication," in IEEE Antennas and Wireless Propagation Letters, vol. 11, pp. 342-345, 2012, doi: 10.1109/LAWP.2012.2191383.

[22] Chou, Ke-Ru; Lin, Han-Nien; Lu, Wei-Hsien; Chang, Heng-Wen; and Tiong, Kwong-Kau (2015) "DESIGN AND OPERATION OF AN EDGE-WALL SLOTTED WAVEGUIDE ARRAY ANTENNA WITH ULTRALOW SIDE LOBES FOR APPLICATION OF OFF-SHORE RADAR," Journal of Marine Science and Technology: Vol. 23: Iss. 5, Article 5. DOI: 10.6119/JMST-015-0226-2.

[23] A. Grbic and G. V. Eleftheriades, "Leaky CPW-based slot antenna arrays for millimeter-wave applications," in IEEE Transactions on Antennas and Propagation, vol. 50, no. 11, pp. 1494-1504, Nov. 2002, doi: 10.1109/TAP.2002.804259.

[24] N. T. Tuan, K. Sakakibara and N. Kikuma, "Bandwidth Extension of Planar Microstrip-to-Waveguide Transition by Via-Hole Locations at Both Sides of Microstrip Line," 2019 IEEE International Symposium on Antennas and Propagation and USNC-URSI Radio Science Meeting, Atlanta, GA, USA, 2019, pp. 673-674, doi: 10.1109/APUSNCURSINRSM.2019.8888571.

[25] B. Li, J. Zhang, Y. Deng, T. Ma, Z. Zhou and L. Sun, "W-band Microstrip-to-Waveguide Transition without Back-short Structure," 2021 International Conference on Microwave and Millimeter Wave Technology (ICMMT), Nanjing, China, 2021, pp. 1-2, doi: 10.1109/ICMMT52847.2021.9618261.

[26] M. Sarkar and A. Majumder, "A Novel Broadband Microstrip to Waveguide Transition at W band with High Manufacturing Tolerance Suitable for MMIC Packaging," 2018 IEEE MTT-S International Microwave and RF Conference (IMaRC), Kolkata, India, 2018, pp. 1-4, doi: 10.1109/IMaRC.2018.8877214.

[27] Z. Xu, J. Xu and C. Qian, "Novel In-Line Microstrip-to-Waveguide Transition Based on E-Plane Probe T-Junction Structure," in IEEE Microwave and Wireless Components Letters, vol. 31, no. 9, pp. 1051-1054, Sept. 2021, doi: 10.1109/LMWC.2021.3083281.

[28] C. Wu et al., "Millimeter-Wave Waveguide-to-Microstrip Inline Transition Using a Wedge-Waveguide Iris," in IEEE Transactions on Microwave Theory

and Techniques, vol. 70, no. 2, pp. 1087-1096, Feb. 2022, doi: 10.1109/TMTT.2021.3123349.

[29] J. M. Pérez, A. Rebollo, R. Gonzalo and I. Ederra, "An inline microstrip-to-waveguide transition operating in the full W-Band based on a Chebyshev multisection transformer," 2016 10th European Conference on Antennas and Propagation (EuCAP), Davos, Switzerland, 2016, pp. 1-4, doi: 10.1109/EuCAP.2016.7481796.

[30] W. Yin et al., "Frequency Scanning Single-Ridge Serpentine Dual-Slot-Waveguide Array Antenna," in IEEE Access, vol. 8, pp. 77245-77254, 2020, doi: 10.1109/ACCESS.2020.2989318.

[31] Trinh-Van, Son & Song, Sung Chan & Seo, Seung-Hee & Hwang, Keum. "Waveguide Slot Array Antenna with a Hybrid-Phase Feed for Grating Lobe Reduction. International Journal of Antennas and Propagation. 2016. 10.1155/2016/4825924.

[32] Jae-Ho Lee, Takuichi Hirono, Jiro Hirokawa and Makoto Ando, "A center-feed waveguide transverse slot linear array using a transverse-slot feed for blocking reduction," 2008 IEEE Antennas and Propagation Society International Symposium, San Diego, CA, 2008, pp. 1-4, doi: 10.1109/APS.2008.4619808.

[33] P. Enayati and D. Zarifi, "Design of a Wideband Coaxial-to-Rectangular Waveguide Transition Based on Supershapes," in IEEE Access, vol. 10, pp. 121924-121929, 2022, doi: 10.1109/ACCESS.2022.3222796.

[34] W. Yi, E. Li, G. Guo and R. Nie, "An X-band coaxial-to-rectangular waveguide transition," IEEE International Conference on Microwave Technology & Computational Electromagnetics, Beijing, China, 2011, pp. 129-131, doi: 10.1109/ICMTCE.2011.5915181.

[35] Z. Liu, H. Lu, J. Liu, S. Yang, Y. Liu and X. Lv, "Compact Fully Metallic Millimeter-Wave Waveguide-Fed Periodic Leaky-Wave Antenna Based on Corrugated Parallel-Plate Waveguides," in IEEE Antennas and Wireless Propagation Letters, vol.

[36] M. Skolnik, Radar Handbook, New York, NY, USA:McGraw-Hill, 2008.

[37] Q. Yang, X. Zhao and Y. Zhang, "Design of CRLH Leaky-Wave Antenna With Low Sidelobe Level," in IEEE Access, vol. 7, pp. 178224-178234, 2019, doi: 10.1109/ACCESS.2019.2958496.

Chapter 5

Design of Electromagnetic Field Confinement Devices

In this chapter, two electromagnetic field confinement devices are proposed, designed, and characterized. One design is based on a uniform structure with a central slit, while the other design is based on the same periodic structure as discussed in Chapter 4 but with a different matching network. In this chapter, design equations are developed based on the peculiarities of each structure. The periodic structure is designed for RFID applications at an operation frequency of 867MHz, while the second approach is intended at 4 GHz for high-power applications such as energy transfer. Finally, the results of the different designs are analyzed and compared.

5.1 Electromagnetic Field Confinement based on SIW for RFID applications

An Ultra-High Frequency (UHF) Radio Frequency Identification (RFID) system is a remote data storage and retrieval system that uses RFID tags, cards, or transponders. It generally consists of a reader with an antenna that sends a radio frequency signal to a tag and receives a backscattered signal in return, allowing for target identification. UHF RFID systems have been widely

used in logistics, transport, and supply chain applications for tracking and wireless identification, among other uses.

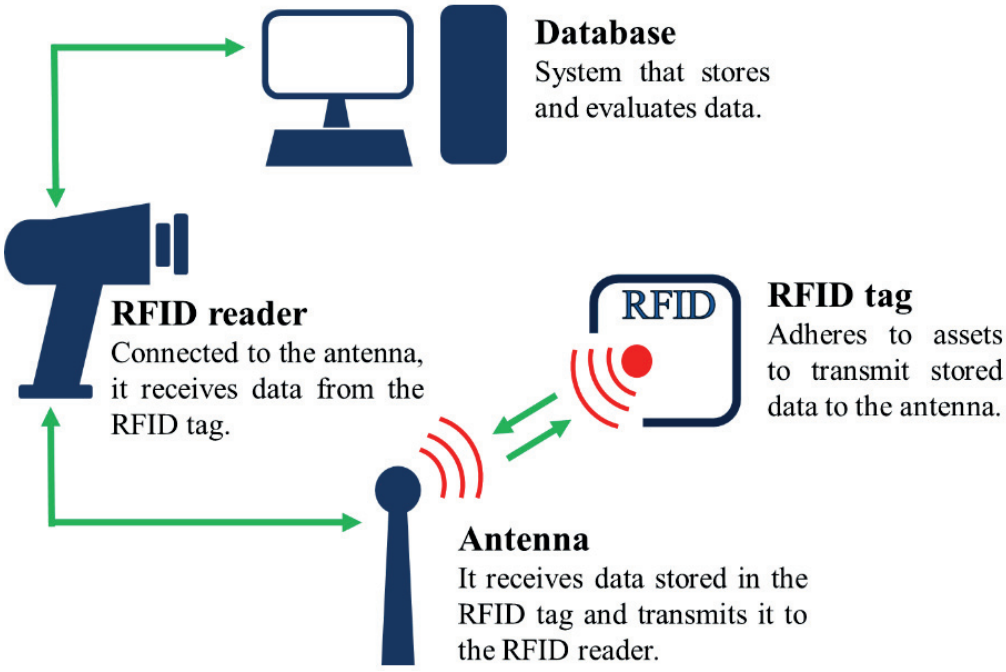


Figure 5.1 RFID system cycle.

Current regulations for UHF-RFID impose a maximum level of power density that can be sent by the reader, limiting the communication range between far-field RFID reader antennas and passive tags to typically 6-8 m [1]. Although conventional far-field RFID reader antennas have been extensively studied [1]-[3], they are not suitable for low-range detection. It is difficult to achieve adequate illumination volume with negligible levels of radiation leakage beyond it for near-field (NF) applications. As previously mentioned in Chapter 2, some of these applications are: points of sale at shops and stores in desktop readers [4]-[5], printer encoders [6]-[7], smart shelves [8]-[9], and smart point readers [10]-[11], among others. To address these limitations, our research group proposed the use of field confinement devices [12].

5.1.1 Principle of operation

The electromagnetic field confinement device is based on an SIW structure loaded with a longitudinal slit along the propagation direction (x-axis) located at the centre of the wide wall, and an exponential tapered transition between

the access lines and the SIW structure. Figure 5.2 shows a schematic representation of the structure.

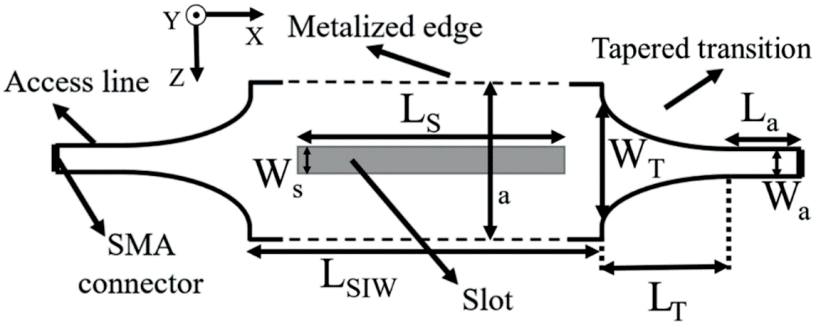


Figure 5.2 Sketch of the electromagnetic field confinement device (the solid grey represents the dielectric, and the dashed black line indicates the metallized wall).

Recalling the equation (2.17) developed in Chapter 2.3 [12], which allows determining the attenuation constant α_y of the electric field in the broadside direction from the guided mode phase constant, we have:

$$\alpha_y = \sqrt{\beta^2 - {k_0}^2} \tag{5.1}$$

where β is the phase constant of the guide mode and k_0 is the wavenumber in a vacuum. In rectangular non-magnetic dielectric-filled waveguide the $TE_{m,n}$ mode phase constant is defined as [13]-[14]

$$\beta_g = \pi \sqrt{\varepsilon_r \mu_0 \left(\frac{2f}{c}\right)^2 - \left[\left(\frac{m}{a}\right)^2 + \left(\frac{n}{b}\right)^2\right]} \tag{5.2}$$

where a and b are the dimensions of the waveguide width wall and narrow wall respectively, f is the operation frequency, ε_r is the relative permittivity of the substrate, and c is the speed of light in vacuum. Considering only the TE10 mode from equation 5.2, and adding the guided mode to equation 5.1, it becomes possible to determine the necessary SIW structure width to achieve a desired decay factor at a specified operating frequency.

$$\boxed{a = \frac{\pi}{\sqrt{(\varepsilon_r - 1) \cdot (2\pi f/c)^2 - {\alpha_y}^2}}} \tag{5.3}$$

Finally, the field distribution will determine whether the electric field experiences exponential decay or follows a Hankel function of the first kind, order 1 [12].

5.1.2 Device design

The electromagnetic confinement device was designed to achieve 1 dB/cm decay factor in European RFID EPC Gen 2 protocol. The frequency range in RFID European regulations is 865.6 - 867.6 MHz. The material used in the design was Rogers RO3010 laminate, which consists in $h = 1.27$ mm dielectric thickness with a relative electric permittivity $\varepsilon_r = 11.2$ and $tag\delta = 0.002$, sandwiched by two copper plates of $t = 35$ µm thickness.

To feed the electromagnetic field confinement device, a coaxial-to-SIW transition matching network based on an access line of 50 Ω and a taper transition was designed. The parameters of the exponential taper transition were obtained using the procedure proposed in [14]-[15]. Subsequently, these values were optimized through a parameter sweep in CST Studio. The following equations allow to obtain the width of the transition taper W_t:

$$\frac{1}{W_e} = \begin{cases} \dfrac{60}{\eta h}\ln\left(8\dfrac{h}{W_t} + 0.25\dfrac{W_t}{h}\right) & \dfrac{a}{h} < 1 \\ \dfrac{120\pi}{\eta h\left[\dfrac{W_t}{h} + 1.393 + 0.667\ln\left(\dfrac{W_t}{h} + 1.444\right)\right]} & \dfrac{a}{h} > 1 \end{cases} \tag{5.4}$$

$$\frac{1}{W_e} = \frac{4.38}{a} e^{\left(-0.627\frac{\varepsilon_r}{\frac{\varepsilon_r+1}{2}+\frac{\varepsilon_r-1}{2\sqrt{1+12\frac{h}{W_t}}}}\right)} \tag{5.5}$$

where η is the impedance of free space, h is the dielectric thickness, a is the width of the SIW structure, and ε_r is the relative permittivity.

The taper lengths must be chosen as a multiple of a quarter of a wavelength in order to minimize the return loss. Thus, the parameter L_t is given by

$$L_T = \frac{\lambda}{4}n = \frac{c}{4\sqrt{\epsilon_r}f}n \tag{5.6}$$

where n is any natural number. Computing equation (5.3) to obtain a decay factor $\alpha_y = 1$ dB/cm at 867 MHz the value $a = 55.84$ mm was obtained. This decay factor corresponds to a characteristic distance $d_\alpha = 8.7$cm. Next, the length and the width of the access lines were computed with Matlab, yielding $L_a = 10$ mm and $W_a = 1.15$ mm, respectively. Finally, applying (5.4) – (5.6) the value $W_t = 21$ mm and $L_t = 51.3$ mm for $n = 2$ was obtained. The designed tapered transition follows the function $f(x)=e^{(0.034x)}$. In order to optimize the parameters of the tapered transition, a parameter sweep simulation under perfect matching conditions between the access line and the SIW structure was made. Figure 5.3 shows the return losses of the matching network computed according [14]-[15] and optimized.

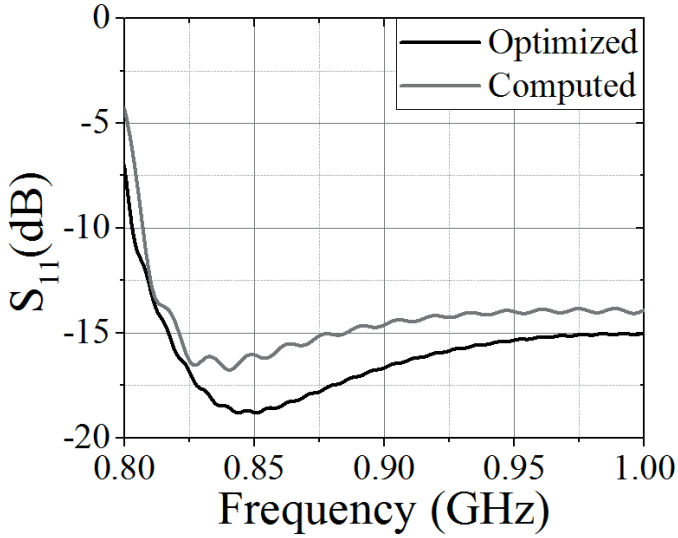


Figure 5.3 Reflection coefficient (the black solid line represents optimized parameters, while the dark grey solid line corresponds to computed parameters).

As can be seen, a reduction of approximately 3 dB in return losses at operation frequency was achieved. The final design parameters of the electromagnetic field confinement device are summarized in the following table.

Table 5.1. Dimensions of the electromagnetic field confinement device.

	L_a	W_a	L_t	W_t	L_s	W_s	a	L_{SIW}
Value (mm)	10	1.15	64	9.96	576	1	55.84	596

The width of the slit (W_s = 1 mm) was chosen to provide enough electromagnetic field in the aperture, prevent mismatching, and be small enough to minimize perturbation of the propagating TE_{10} mode. Since the structure can be made arbitrarily large, considering the size constrains of the milling machine, the SIW length L_{SIW} and the slit length L_s were set to 596 mm and 576 mm respectively.

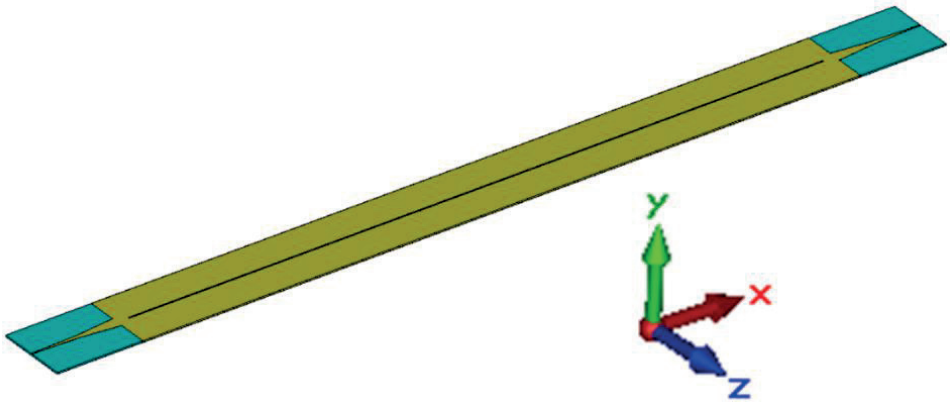


Figure 5.4 Design of the electromagnetic confinement device.

Figure 5.4 illustrates the final design of the electromagnetic field confinement device. As observed in Figure 5.5, the isolines of the electric field amplitude in the broadside direction exhibit a flat distribution from 1 cm of the surface. Therefore, this field uniformity in the z-direction up the slit will implies an exponential decay factor in the centre of the structure according to (2.16). However, within 1 cm from the surface, a somewhat more cylindrical dependence becomes apparent. This cylindrical dependence also can be observed in z-direction from the edge of the device. In these cases, the field decay will be proportional to the Hankel function of first kind and order 1 [12].

In the case of the US (United States) RFID protocol, the frequency range is 902-928 MHz. Using the same design and considering 915 MHz, the computation in (5.1) yields an attenuation constant $\alpha_y = 1.97$ dB/cm, corresponding to a d_a = 4.57 cm. In this case, the electric field isolines also exhibits flat distribution from 1 cm of the surface in broadside direction, and the field continues bound to the surface.

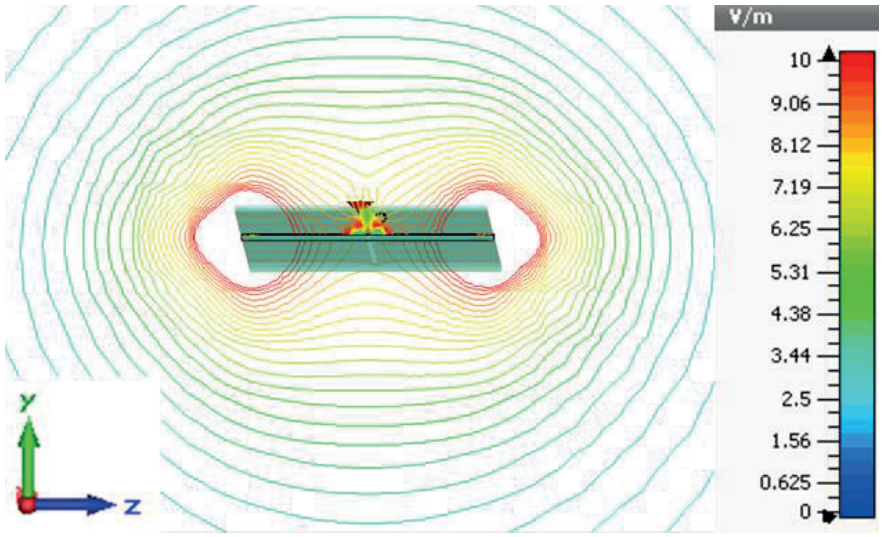


Figure 5.5 Isolines of the field amplitude at 867 MHz. Simulation in CST Microwave Studio with waveguide ports and open boundary conditions.

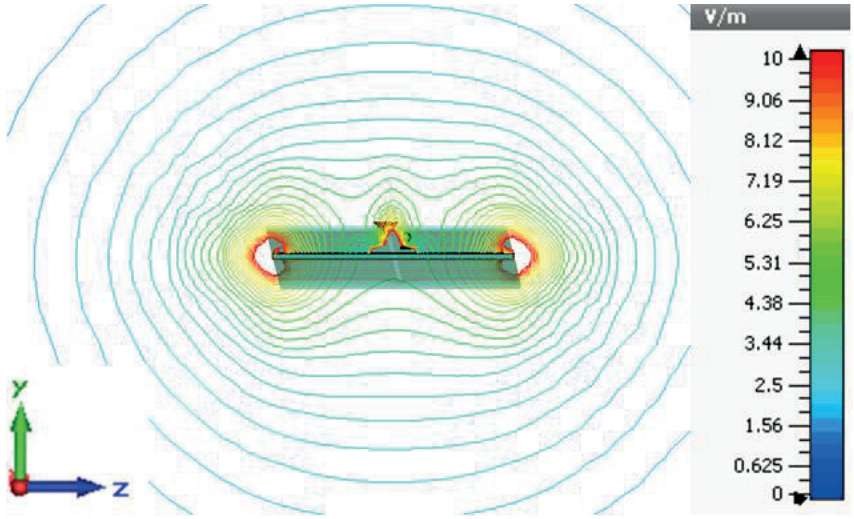


Figure 5.6 Isolines of the field amplitude at 915 MHz. Simulation in CST Microwave Studio with waveguide ports and open boundary conditions.

In Figure 5.7 is shown that this device features a current distribution that maximizes the electric field in the y-direction at the center of the structure and in the z-direction between the slit and the edges of the device. This ensures the reading of tags oriented along the y-direction and z-direction on the surface of the structure.

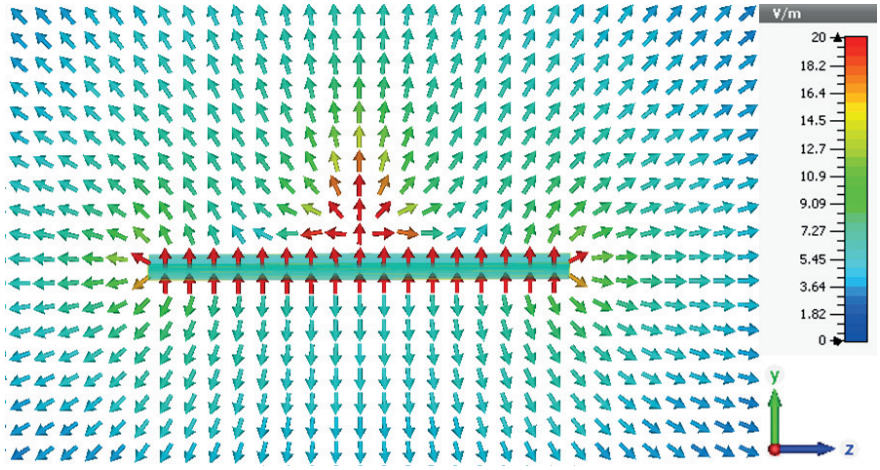


Figure 5.7 Electric pattern at 867 MHz in the *yz*-plane.

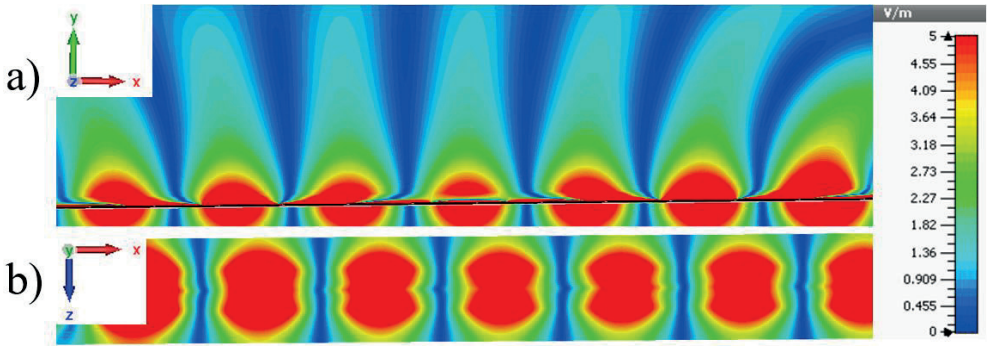


Figure 5.8 Electric field in absolute value at 867 MHz. (a) *xy*-plane. (b) *xz*-plane at 10 mm from the surface.

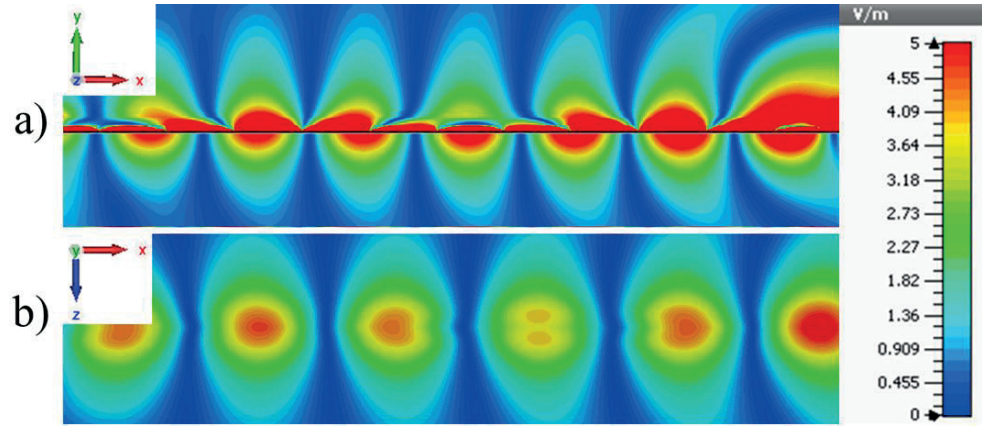


Figure 5.9 Electric field in absolute value at 915 MHz. (a) *xy*-plane. (b) *xz*-plane at 10 mm from the surface.

5.1.3 Measured results

The device was fabricated from a Rogers RO3010 laminate (Figure 5.10). The manufactured structure has been done by means of a milling machine. The design was divided into two symmetrical parts and then soldered with tin. Typically, vias are used to connect conductor traces in different layers of the substrate, ensuring electrical continuity and allowing the signal to flow through the structure. However, to metalize the sides of the fabricated prototype, a conductive silver paint was used. To validate the metallization process, the S-parameters ware measured with the PNA Network Analyzer N5221A and compared to the simulated results.



Figure 5.10 Fabricated prototype.

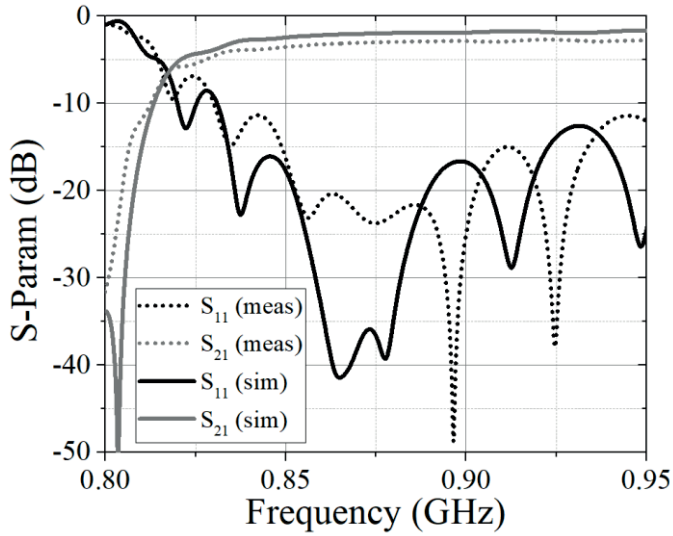


Figure 5.11 S-parameters (the black solid line represents the simulated reflection coefficient, the dark grey solid line represents the simulated transmission coefficient, the black dotted line represents the measured reflection coefficient, and the dark grey dotted line represents the measured transmission coefficient).

Figure 5.11 shows a high level of agreement between the simulated and measured scattering parameters. These results shown the effectiveness of the metallization technique employed, which successfully transforms the commercial laminate into a substrate integrated waveguide structure. A good

matching with the reference impedance is appreciated at the operating frequency (below – 20 dB). The simulated and measured S_{21} at 867MHz are – 2.1 dB and – 3 dB respectively corresponding to an attenuation of 0.035 dB/cm and 0.05 dB/cm.

The electric field measurements were taken by means of an electric field probe (Narda PMM EP-60) in an anechoic chamber. This probe has a frequency bandwidth of 100 kHz to 9.25 GHz and is capable of detecting electric fields within the range of 0.14 to 140 V/m. The structure was excited by means of a pure tone created by a signal generator, amplified with a power amplifier, and transferred (1 W) through a coaxial cable ended with a 3.5 mm SMA connector. The device was terminated with a 50 Ω resistive load.

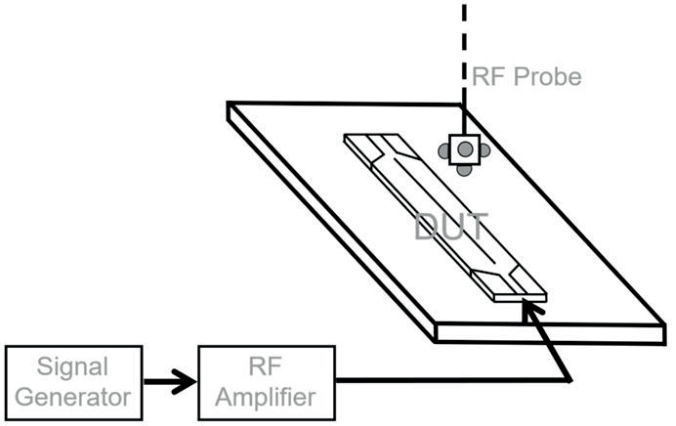


Figure 5.12 Sketch of the measurement setup.

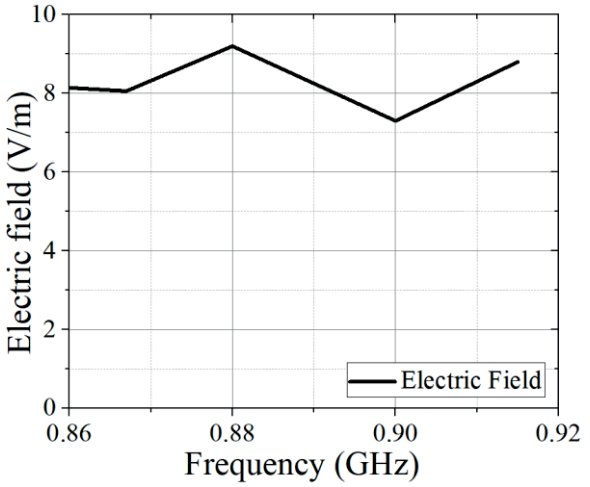


Figure 5.13 Measured field at 1cm from the surface.

Figure 5.13 shows the electric field measured at different frequencies at a distance of 1 cm from the surface. As observed, the electric field on the device's surface ranges from 9 V/m to 7 V/m, showing minimal variation with frequency.

In figure 5.14 a comparison between the measured and theoretical attenuation constant is shown. The analytical result was inferred using equations (5.1) and (5.2) considering only the TE_{10} mode, $\varepsilon_r = 11.2$ and $a = 55.84$ mm. The measured results were obtained by determining the slope of the fitting of the measured normalized electric field (until the electric field drops to 1.8 V). It can be observed that there is a strong correlation between the measured decay factor and the analytical one.

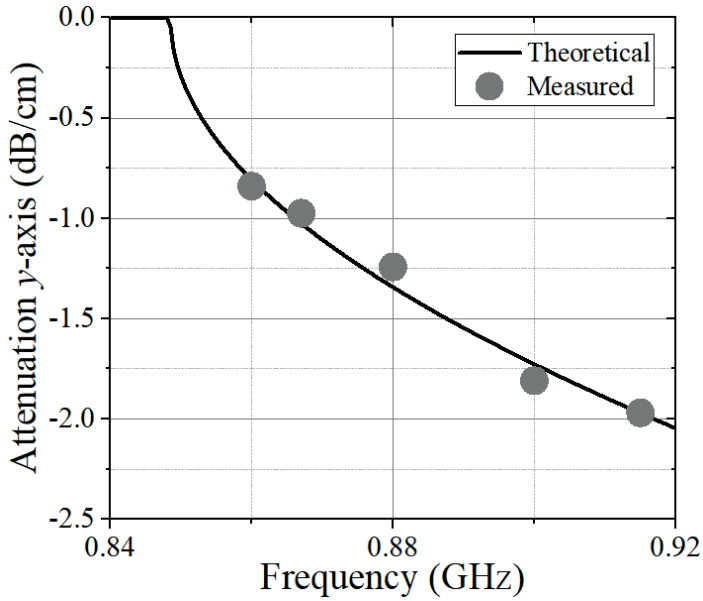


Figure 5.14 Attenuation constant in broadside direction (grey dots represent measured results, while the black solid line represents analytical results).

Figure 5.15 shows the normalized electric field expressed in dB. The electric field was measured from 1 cm away from the surface until the measured electric field dropped below 1.5 V. The experimental results show a very good agreement with the analytical results. Furthermore, when the electric field drops below -12 dB, the attenuation starts to decrease. However, at that point, the field level is already very low compared to the surface level and becomes negligible for RFID applications. Considering that commercial RFID tags

typically require a field strength of 1-2V/m to activate, this design could be used in some applications with a detection distance of up to 14 cm at 867 MHz (Europe) and up to 7 cm at 915 MHz (United States).

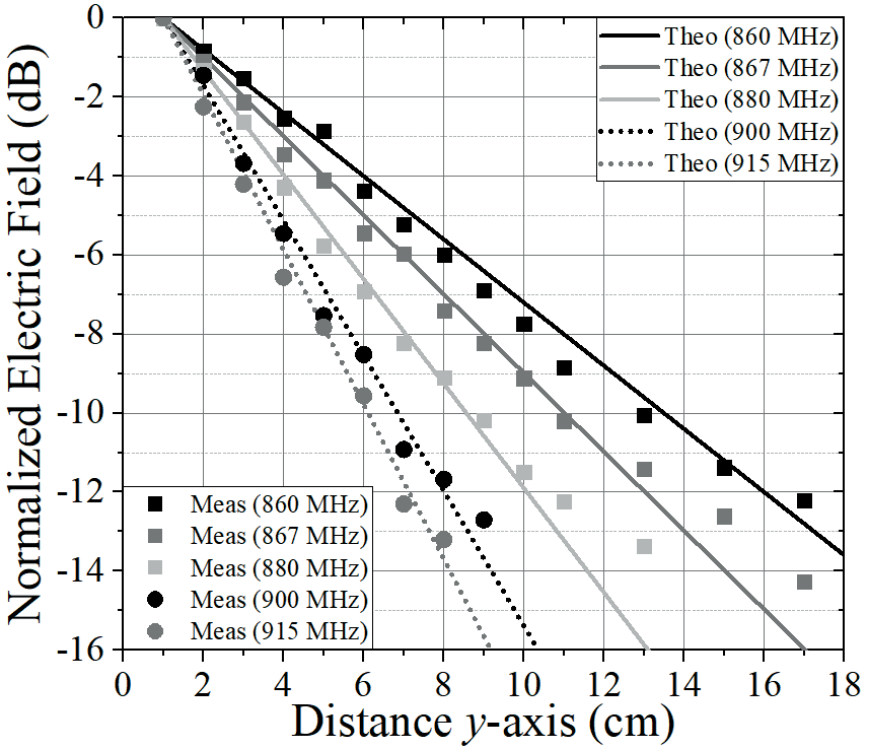


Figure 5.15 Normalized electric field (symbols represent measured results, while solid and dotted lines represent theoretical results).

With this design, the power density undergoes a reduction of a factor of two for every 3 cm of distance in the European protocol, and for every 1.5 cm of distance in the United States protocol. Through the redesign of the device or an increase in supplied power (while considering the different protocols restrictions), the detection range can be extended or reduced based on the specific application requirements.

To validate that the structure does not radiate, the far-field measurement setup was used. Figures 5.16 and 5.17 depict the measured gain of the structure in the *xy*-plane and *zy*-plane at 867 MHz and 915 MHz, respectively. In both cases, the gain consistently remains below -15 dB, indicating that the structure has a negligible level of radiation for both the European RFID protocol and the American RFID protocol.

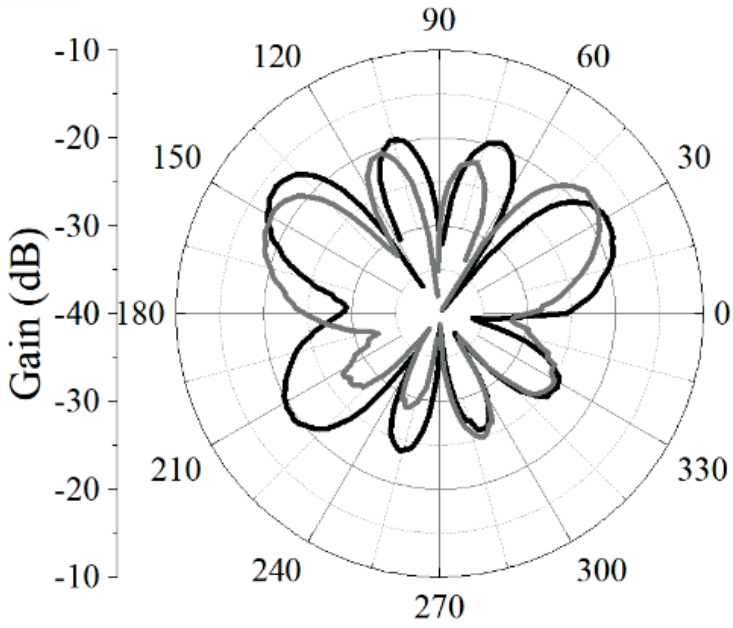


Figure 5.16 Gain measured in the *xy*-plane (the black line represents the results at 867 MHz, while the dark grey line represents the results at 915 MHz).

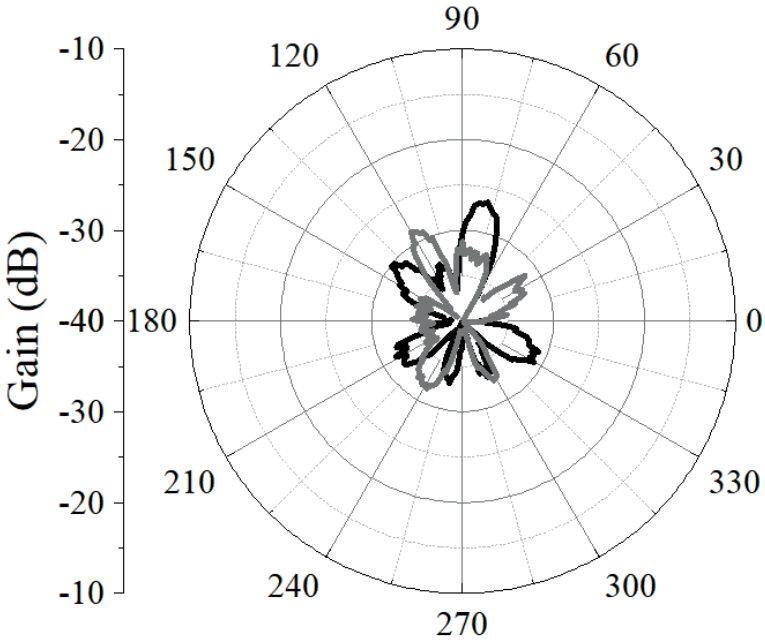


Figure 5.17 Gain measured in the *zy*-plane (the black line represents the results at 867 MHz, while the dark grey line represents the results at 915 MHz).

5.2 Electromagnetic Field Confinement based on Waveguide

International Commission on Non-Ionizing Radiation Protection (ICNIRP) establishes guidelines and directives for protecting against non-ionizing radiation. Established exposure limits, as outlined in [17]-[18], delineate the maximum permissible levels of electromagnetic fields to which humans can be exposed. Compliance with these limits is essential for the commercialization of any product utilizing this technology. Therefore, effective control of the evanescent waves holds significant potential for applications in this field. In this context, the use of rectangular waveguides emerges as a highly interesting technology, particularly due to their capability to handle high powers, and low losses [14], [19]. The theory developed in [12] provides a framework that can be effectively applied in the implementation and control of evanescent waves in rectangular waveguides.

5.2.1 Principle of operation

The proposed electromagnetic field confinement device is based on a periodic serpentine rectangular waveguide loaded with transverse rectangular slots and a transition between a coaxial cable and the waveguide. Figure 5.18 shows a schematic representation of two consecutive unit cells.

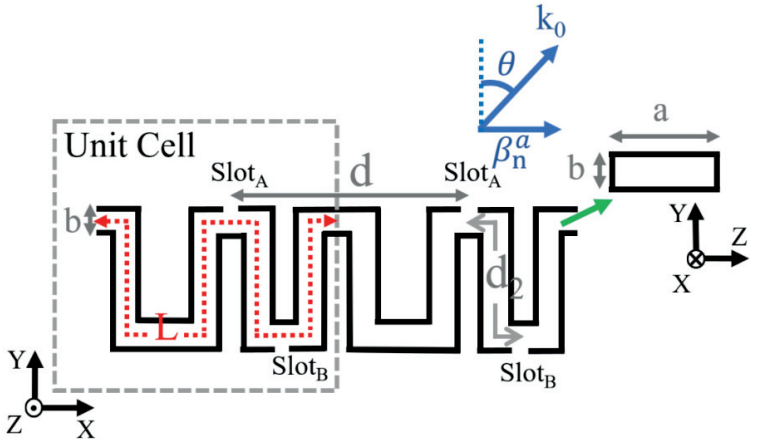


Figure 5.18 Sketch of the unit cells.

As can be observed, the proposed unit cell is the same as used in the last chapter to design the main LWA. In this serpentine arrangement, the effective phase constant of each of the nth space harmonics on the aperture can be written as

$$\beta_n^a = \frac{(\beta_g L + 2\pi n_{sh})}{d} \tag{5.7}$$

where β_g is the guide phase constant in the rectangular waveguide, L is the serpentine length, d is the distance of two consecutive slots and n_{sh} is the number of the space harmonic, named as such to distinguish it from the subindex of the TE_{mn} mode. The guide phase constant in the rectangular waveguide is defined as [13]-[14].

$$\beta_g = \sqrt{(k_0)^2 - \left[\left(\frac{m\pi}{a}\right)^2 + \left(\frac{n\pi}{b}\right)^2\right]} \tag{5.8}$$

where a and b are the dimensions of the waveguide width wall and narrow wall respectively and k_0 is the wavevector.

Considering only the TE_{10} mode from equation 5.8, and adding the effective guided mode to equation 5.1, it becomes possible to predict the attenuation constant in broadside direction at a specified operating frequency.

$$\alpha_y = \sqrt{\left(\frac{\left(\sqrt{(k_0)^2 - \left[\left(\frac{m\pi}{a}\right)^2 + \left(\frac{n\pi}{b}\right)^2\right]}\right)L + 2\pi n_{sh}}{d}\right)^2 - {k_0}^2} \tag{5.9}$$

It is important to clarify that the equation (5.9) do not consider the phase shift introduced by the slots placed in the unit cell. Accurate way to obtain the decay factor is by means of simulation. In this scenario, the transmission coefficient phase $-\phi_{21}$, derived from simulating a unit cell under perfect matching conditions, will be equivalent to $\beta_g L$.

$$\alpha_y = \sqrt{\left(\frac{-(\phi_{21} + 2\pi n_{sh})}{d}\right)^2 - {k_0}^2} \tag{5.10}$$

Whit the equation (5.10) it is possible to control α_y for a specific application requirement only manipulating the distance between slots and the width of the wide wall. Analyzing equations (5.9) and (5.10), it can be deduced that a specific attenuation constant can be achieved at two different frequencies,

provided that the structure operates in the surface wave mode $\left(\left(\beta_n^{a2} - {k_0}^2\right) > 0\right)$ and $n_{sh} < 0$. Under these conditions, the phase constant at the aperture can be either positive or negative.

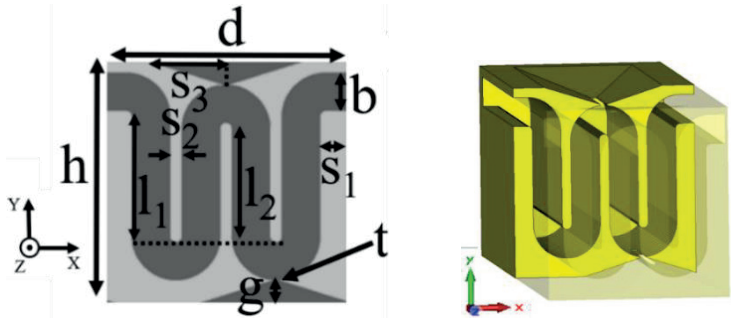
$$\alpha_y = \sqrt{(\beta_n^a)^2 - {k_0}^2} = \sqrt{(-\beta_n^a)^2 - {k_0}^2} \tag{5.11}$$

For negative values of β_n^{a2}, the structure will operate in the second quadrant, whereas for positive values of β_n^{a2}, it will be in the first quadrant.

5.2.2 Device design

The electromagnetic field confinement device was designed based on the same structure as in Chapter 4. The unit cell was designed to obtain broadside radiation at 5GHz as reference. The periodic structure was composed by 30-unit cells. This proposed unit cell confines the electromagnetic field both on the top and bottom surfaces. However, a unidirectional version was also analyzed. In this case, the slots on the bottom surface were suppressed by metallization.

Figure 5.20 depicts the phase of the transmission coefficient for the unit cell described in 5.19. The simulation was conducted using CST Studio 2014, with two waveguide ports placed at each end of the unit cell to achieve perfect matching conditions. For comparison purpose, the simulation was carried out in three different scenarios: with 2 slots, with one slot, and without slots. Afterward, the attenuation constant in the broadside direction was calculated.



(a) (b)

Figure 5.19 (a) Unit cell cross section layout. Metallization is highlighted in light gray and the absence of metallization in dark gray. Dimensions are: a = 60 mm, b = 3.1 mm, d = 19.42 mm, h= 20.2 mm, l_1 = 11 mm, l_2 = 10, s_1 = 2.01mm, s_2 = 1 mm, s_3 = 20.35 mm, g = 2 mm, t = 0.1 mm. (b) 3D view of the unit cell.

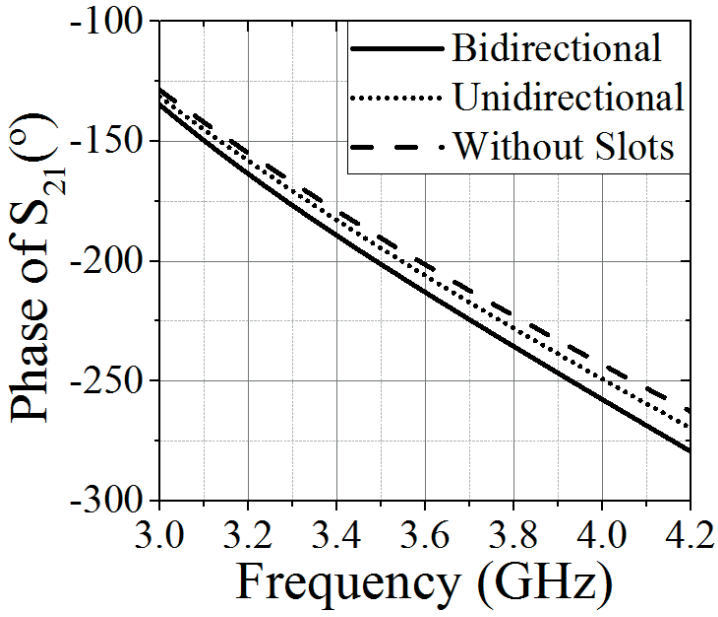


Figure 5.20 Phase of the transmission coefficient under perfect matching condition (solid black line represents 2 slots per UC, black dotted line represents 1 slot per UC, and black dashed line represents no slots).

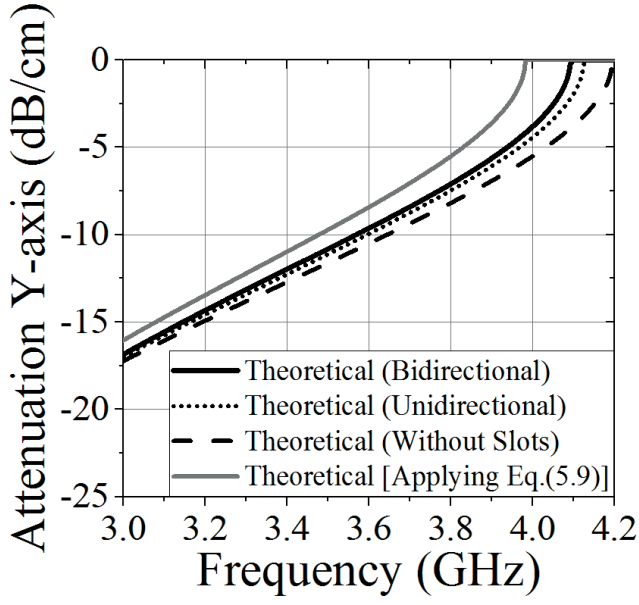


Figure 5.21 Theoretical electromagnetic field attenuation (the black line represents 2 slots per UC, the black dotted line represents 1 slot per UC, the black dashed line indicates no slots, and the gray line corresponds to the solution obtained using equation 5.9).

In Figure 5.21 the attenuation constant was derived from (5.10) using the phase obtained in the simulation (Fig. 5.20). However, for the purely theoretical case, the equation (5.9) was used with the following parameters: $a = 60$ mm, $L = 71.83$ mm, $d = 19.42$ mm, $n_{sh} = -1$, m $= 1$. These parameters determine broadside radiation at 5 GHz, without considering the phase contribution introduced by the slots. As can be observed, each slot introduces an approximately 10-degree of phase shift. Additionally, the phase shift is not constant with frequencies. This variability arises because the slot introduces a greater phase shift to the guided signal as the wavelength approaches the dimensions of the slot. Hence, as it is demonstrated, this factor influences the control of α_y.

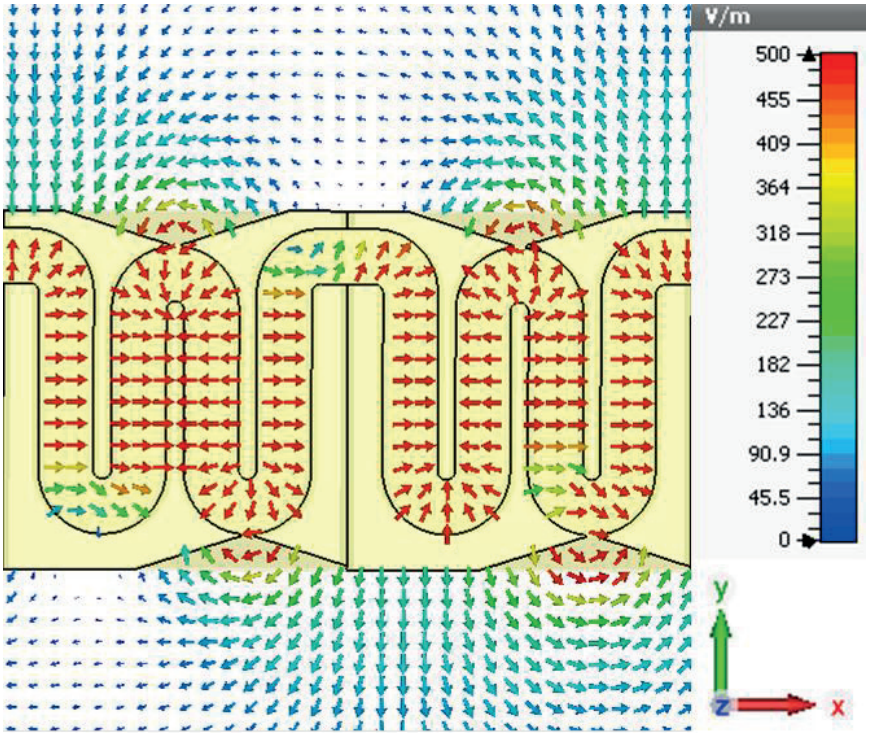


Figure 5.22 Electric pattern at 4 GHz in the xy-plane.

This device showcases a field distribution that maximizes the electric field in the x-direction in most of the space surrounding the structure.

In figures 5.23 and 24, a more cylindrical dependence of the isolines is present within a few centimeters from the surface (z-axis $= 0$). In this area, the field induced by high-order Floquet modes exhibits a higher decay ratio

compared to the field generated by the $n - 1$ mode, given their shorter wavelengths [12]. Beyond these $\approx$ 3 cm, a flat dependence is observed. This enables the approximation of electric field attenuation using an exponential expression.

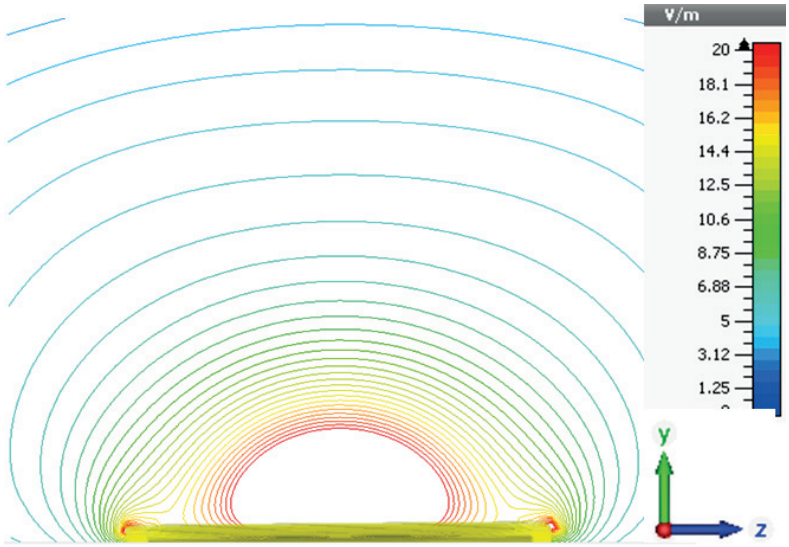


Figure 5.23 Isolines of the field amplitude at 3.8 GHz. Simulation in CST Microwave Studio with waveguide ports and open boundary conditions.

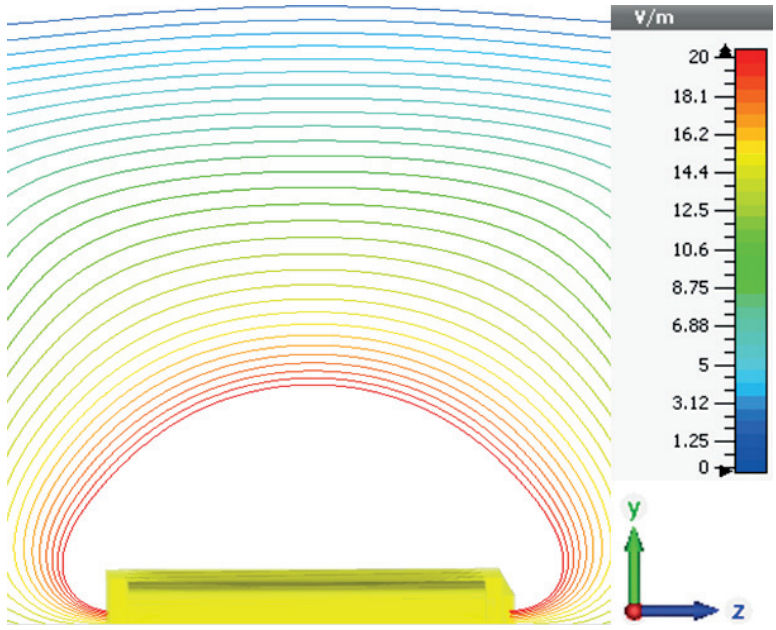


Figure 5.24 Isolines of the field amplitude at 4 GHz. Simulation in CST Microwave Studio with waveguide ports and open boundary conditions.

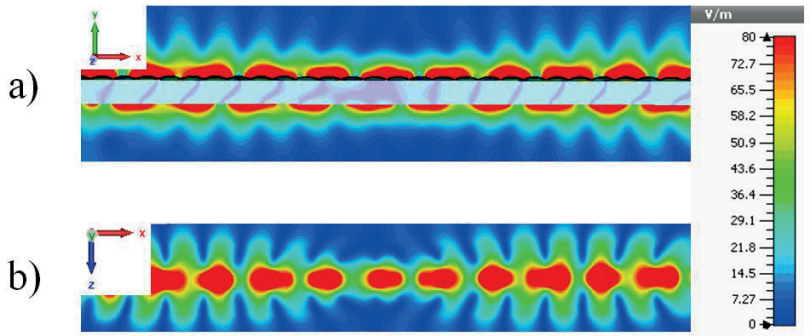


Figure 5.25 Electric field in absolute value at 4 GHz. (a) *xy*-plane. (b) *xz*-plane at 5 mm from the surface.

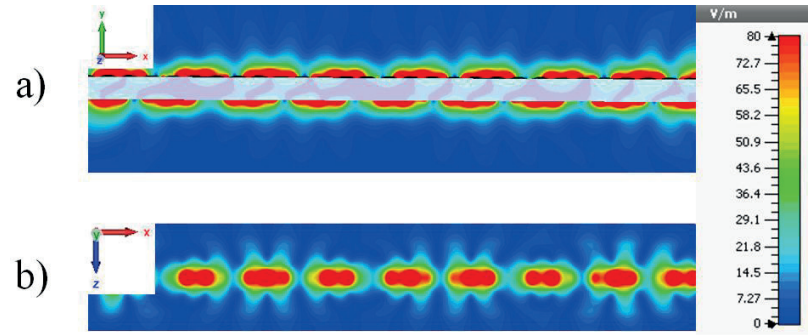


Figure 5.26 Electric field in absolute value at 3.8 GHz. (a) *xy*-plane. (b) *xz*-plane at 5 mm from the surface.

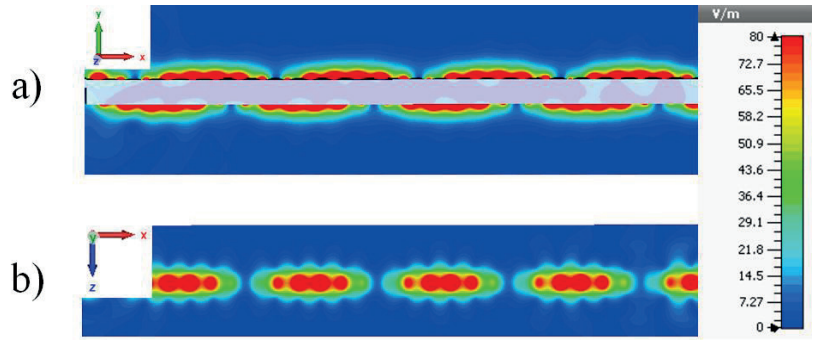


Figure 5.27 Electric field in absolute value at 3.6 GHz. (a) *xy*-plane. (b) *xz*-plane at 5 mm from the surface.

In Figures 5.25 – 5.27, the electric field magnitude is shown at frequencies of 4, 3.8, and 3.6 GHz on the surface of the structure. As observed, as the field approaches the light cone (4.1 GHz), the surface field magnitude increases. This is attributed to the fact that the attenuation constant tends to zero as it

approaches the radiative operating mode. Theoretically, it can be deduced from Equation 5.1, as the guided mode phase constant approaches k_0, the field decay constant decreases. It can also be noted how the field remains entirely confined to the surface of the device without significant radiation.

To analyze the structure in the surface operation mode, a matching network was designed to enable the transition from the coaxial cable to the waveguide, covering the frequency range from 3.6 to 4.1 GHz. To achieve this, the dimensions of l_p and h_p were calculated to obtain maximum efficiency, i.e., $\lambda_0/4$. Subsequently, the values were adjusted through simulation. Then, a transition between h_2 and b was implemented, experimenting with various configurations to minimize the size of the matching network. Finally, a transition based on a step impedance with $Z_1/Z_L = Z_0/Z_1 = 0.5$ and a stepped impedance with a length of $2\lambda_g$ was used (Figure 5.28). The parameters were optimized by means of CST Studio 2014.

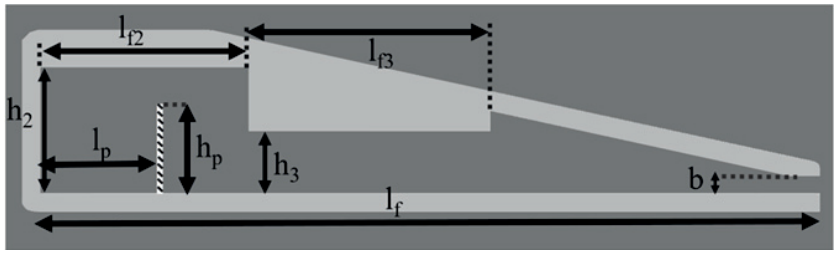


Figure 5.28 Matching network cross section layout. Metallization is highlighted in light gray and the absence of metallization in dark gray. Dimensions are: $h_2 = 30$ mm, $h_3 = 10.5$ mm, $h_p = 15$ mm, $l_f = 125$ mm, $l_{f2} = 35$ mm, $l_{f3} = 40$ mm, $l_p = 15$ mm.

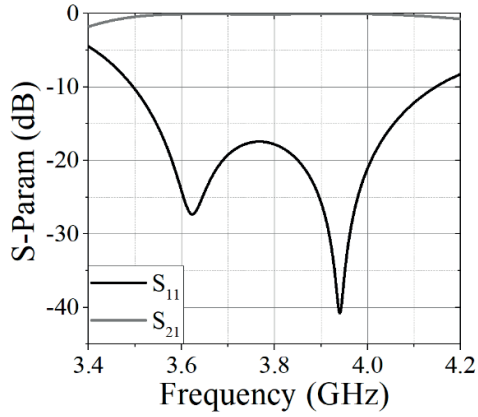


Figure 5.29 S-Parameters of the matching network.

The results in Figure 5.29 were obtained through a simulation under perfect matching conditions, using two waveguide ports. The first port was located at the coaxial cable, and the second port was positioned at the end of the waveguide, similar to the approach taken in the design of the matching network for the leaky wave antenna. A bandwidth was achieved with reflection losses below -10 dB, ranging from 3.6 to 4.1 GHz. Finally, the design was modified to make it modular, as depicted in Figure 5.30.

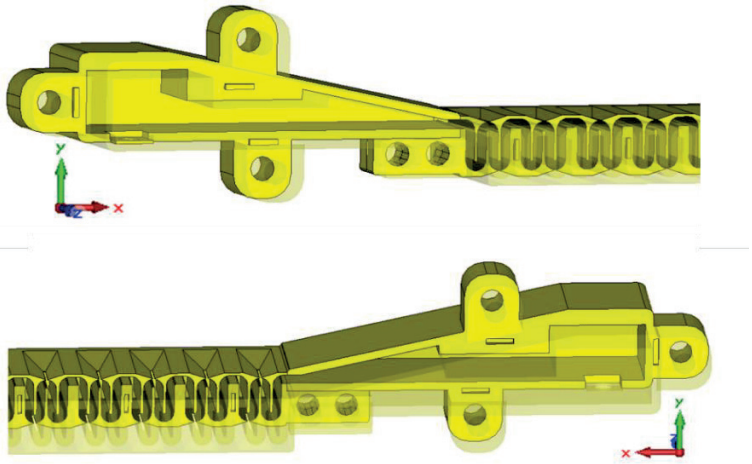


Figure 5.30 Designed matching network prototype.

5.2.3 Fabricated prototype and measured results

The matching network was manufactured by an external company, using CNC technology. The structure was crafted from 6063 aluminum alloy, and the SMA connector (RS Pro straight panel mount SMA connector, jack, solder termination, RS Stock No: 546-3181) within the waveguide was modified as depicted in Figure 5.28. The periodic structure comprises 30 unit cells divided into two parts along the center of the *xy*-plane. Once all the parts were assembled, adhesive aluminum tape was added on the outside of the transition between the matching network and the unit cells to minimize reflection losses. Additionally, aluminum adhesive was applied to the bottom surface of the fabricated prototype to evaluate its unidirectional version.

The measurement setup consisted of a PNA Network Analyzer N5221A and an electric field measurement probe, specifically the Narda PMM EP-600 probe. For all electric field measurements, a power of 0.1 W was applied to the

structure through the Network Analyzer. The following image depicts the matching network and the assembled prototype.

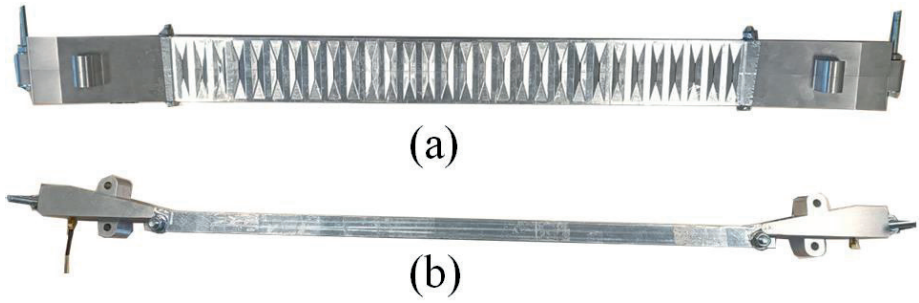


Figure 5.31 Full view of the device. (a) *xz*-plane. (b) *xy*-plane.

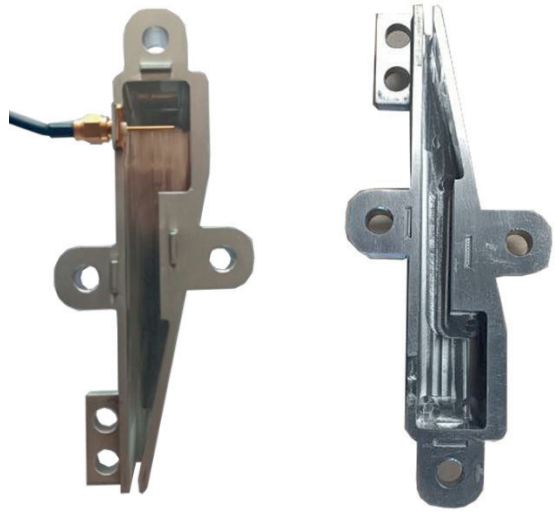


Figure 5.32 (a) Fabricated matching network prototype.

Figures 5.33 and 5.34 shown the comparison between the measured and the simulated S-parameters. Empirical results very similar to those expected through simulation can be observed. The simulated and the measured insertion losses in bidirectional version are below $-$ 1.9 and $-$ 2.1 dB respectively. These measured losses, manly attributed to metal losses, correspond to an attenuation of 0.036 dB/cm. In the unidirectional version, the simulated and measured insertion losses are below $-$ 2 dB, corresponding to an attenuation of 0.035 dB/cm. In general, empirical S-parameters are very similar to those expected through simulation. These results shown a significant potential to incorporate additional unit cells into the device, thereby expanding the illumination area.

It can also be observed that there is an increase in insertion losses from 4 GHz due the transition between the surface wave mode to the radiative wave mode.

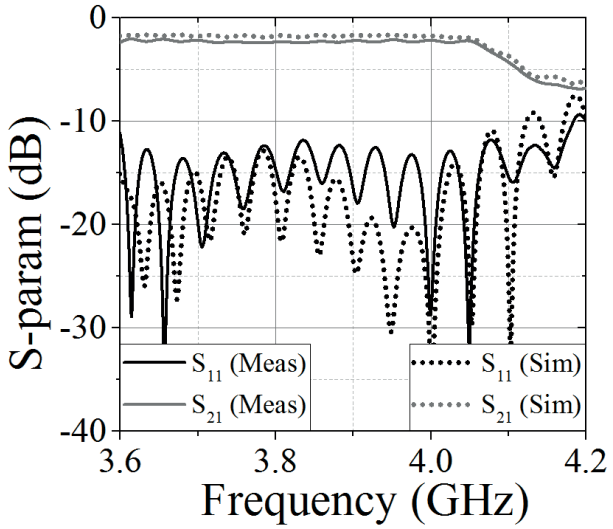


Figure 5.33 S-parameters of the bidirectional electromagnetic field confinement device (the solid line represents measured data, while the dotted line corresponds to simulated results).

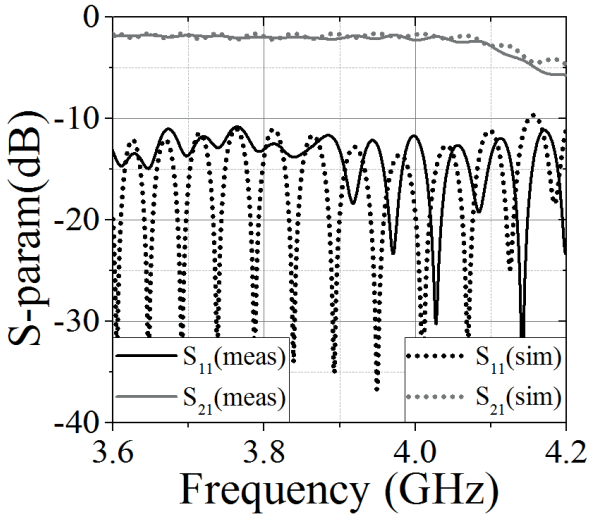


Figure 5.34 S-parameters of the unidirectional electromagnetic field confinement device (the solid line represents measured data, while the dotted line corresponds to simulated results).

In Figures 5.35 and 5.36, the absolute value of the electric field measured with the electric probe at various positions from the top and bottom surfaces

of the device is depicted. It can be observed that in both cases, the trend is exponential. However, the initial samples deviate slightly from the theoretical trend. This is attributed to the contribution of high order space harmonics [12]. Nevertheless, above 3 cm away from the surface, the field decay matches the theoretical trend. The results obtained at 4.085 GHz indicate that even near the limit of the surface operation mode (4.1 GHz), the prediction of electric field attenuation is still working correctly.

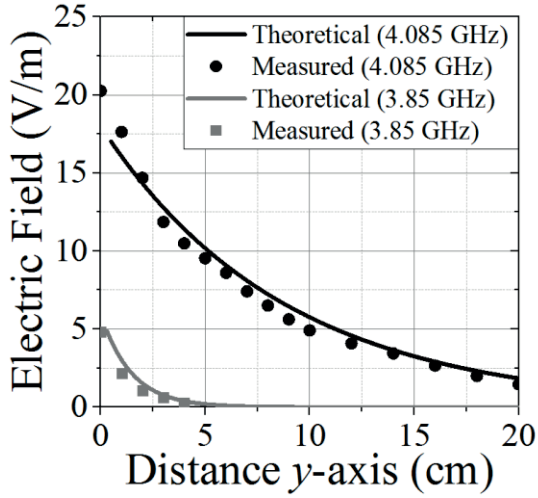


Figure 5.35 Electric field in y-axis on top surface (the symbols represent measured data, while the solid line corresponds to theoretical predictions).

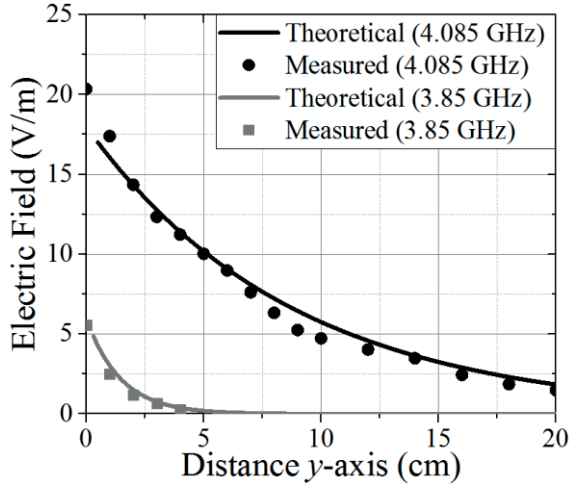


Figure 5.36 Electric field in y-axis on bottom surface (the symbols represent measured data, while the solid line corresponds to theoretical predictions).

In Figure 5.37, the electric field at a distance of 0.1 cm from the surface of the device is depicted for both configurations. This value was employed to normalize the electric field decay illustrated in Figure 5.38.

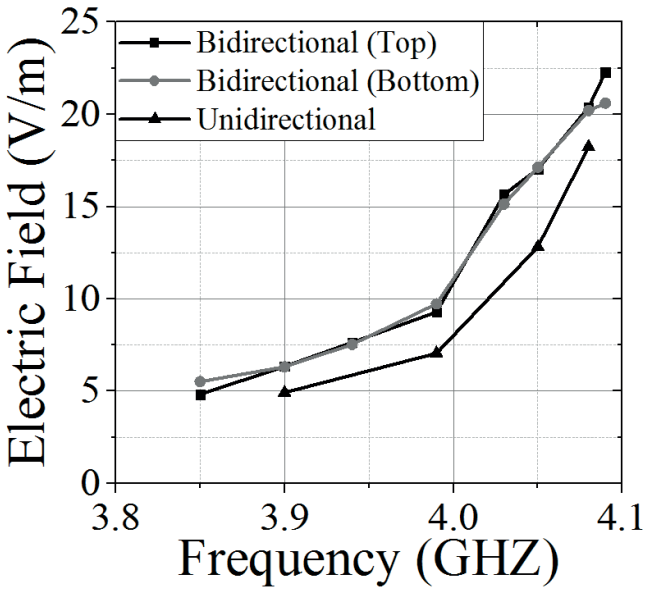


Figure 5.37 Measured electric field at 0,1 cm from the surface of the electromagnetic field confinement device.

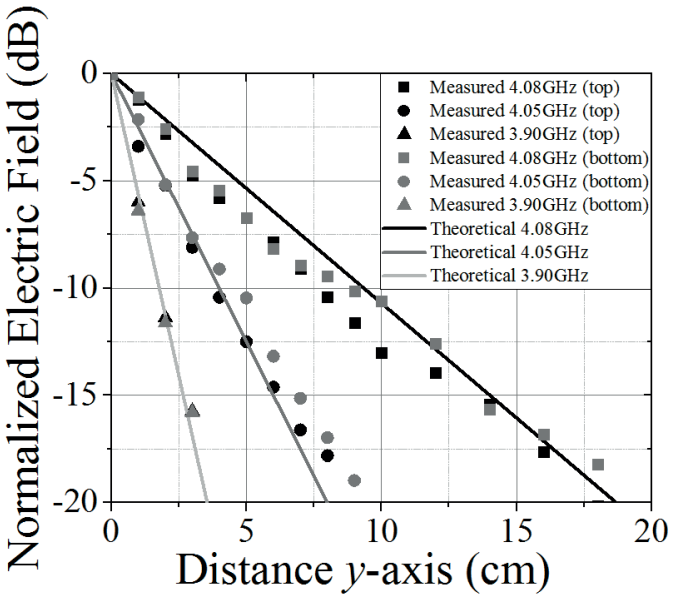


Figure 5.38 Normalized electric field decay in broadside direction (the symbols represent measured data, while the solid line corresponds to theoretical analysis).

In Figures 5.39 and 5.40, a comparison is presented between the measured attenuation constant and the theoretical analysis at different frequencies for both bidirectional and unidirectional arrangements.

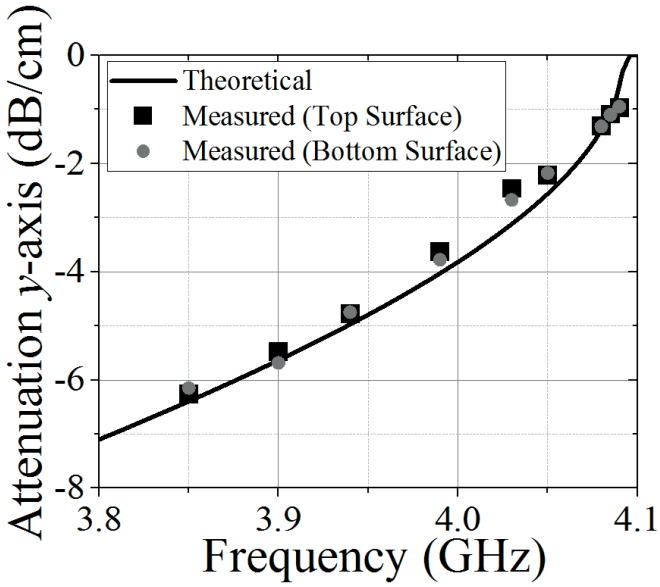


Figure 5.39 Attenuation constant in bidirectional arrangement (black squares represent measurements on the top surface, gray dots represent measurements on the bottom surface, and the black line corresponds to the theoretical prediction).

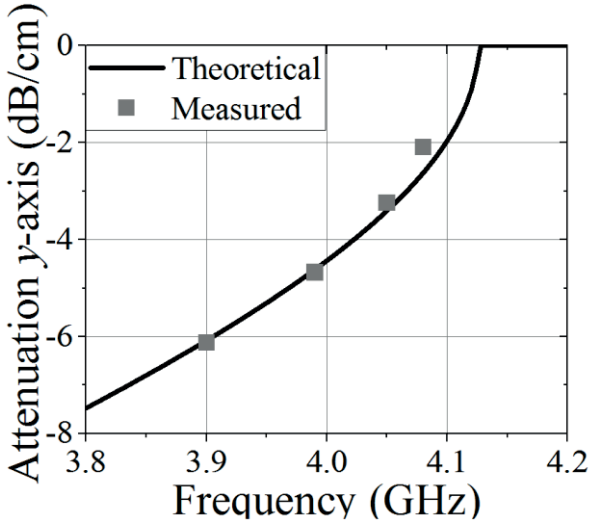


Figure 5.40 Attenuation constant in unidirectional arrangement (gray squares represent measured data, while the black line corresponds to the theoretical prediction).

The results were obtained by measuring the electric field level using an electric field probe from the surface until the signal dropped below 0.2 V/m. Afterward, the results were normalized, and the slope of the line was determined. The theoretical prediction was calculated using the same method as employed in Figure 5.22. The obtained results showcase a high degree of accuracy. Even as the frequency approaches the light cone, the attenuation in the broadside direction consistently aligns with the theoretical predictions.

Figure 5.41 shows the radiation pattern at different frequencies in the bidirectional arrangement.

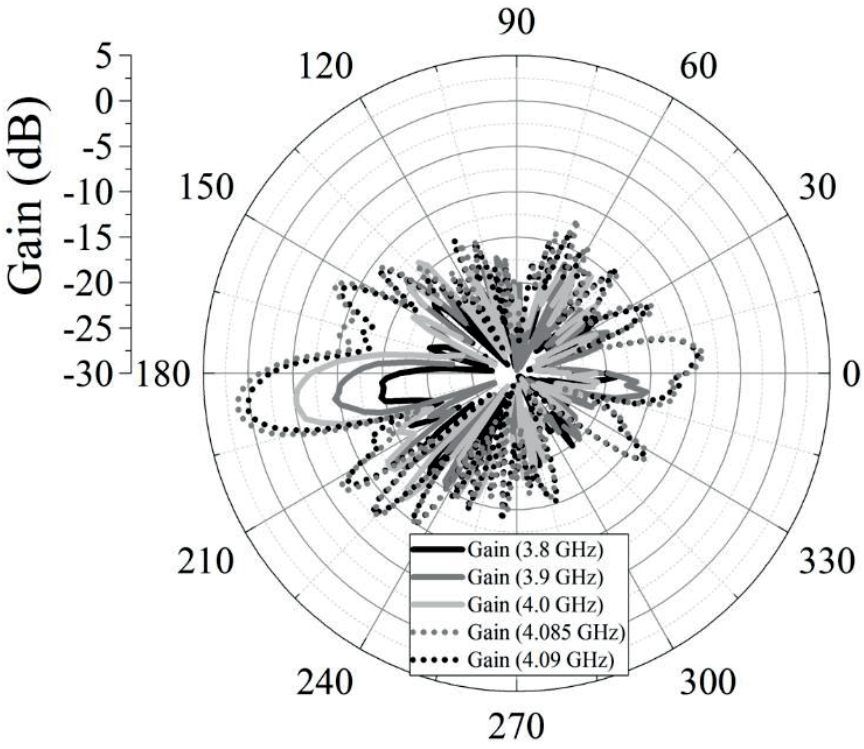


Figure 5.41 Measured radiation pattern in E plane at different frequencies (*xy*-plane).

As the frequency approaches the light cone, the radiation pattern exhibits a main low lobe (0.2 dB at 4.09 GHz) near the endfire direction (*x*-axis). This is due to the transition process between the surface wave mode and the radiative mode. However, in the other directions, the radiation remains below - 7.5 dB. To minimize this additional radiation, some approaches can be considered. The

first approach involves increasing the length of the structure by adding more unit cells. This approach is proposed because leakage radiation is mainly attributed to the finite characteristics of the structure, which introduces a windowing effect on the transmitted signal. This can be inferred through the analysis of the Fourier transform of the spatial functions involved. In this scenario, the functions under consideration are the sinusoidal transmitted signal and the finite length of the structure, portrayed as a rectangular pulse. The Fourier transform of a rectangular pulse result in a *Sinc(kL)* function, while the Fourier transform of the travelling wave corresponds to a delta function. This leads to a *Sinc* function placed at the effective phase constant in the reciprocal space (see Appendix II). In a *Sinc* function, the width of the lobes increases inversely proportional to the pulse length. The higher the value of the *Sinc(kL)* function within the light cone in the evanescent mode, the greater the leakage radiation. If the structure is very short, it's possible that even part of the main lobe of the *sinc* function is within the light cone. By increasing the length of the structure (by adding more unit cells), the width of the *Sinc* function will decrease, reducing the leakage radiation of the evanescent wave.

The second approach involves reducing the radiation resistance of the slots by reducing the size of the slots or increasing the depth. Another solution could modify the aperture distribution. Also, it can be considered the use of a RF absorbent structure to eliminate the backfire radiation when frequency approximates the light cone [20], [21]. Furthermore, it can be observed that below 3.9 GHz, the gain is consistently below -10 dB across all directions, effectively ensuring the preservation of the electromagnetic field confined to the surface of the device.

5.3 Comparison and conclusions

When dealing with electromagnetic field confinement devices, the main objective is the correct prediction of the field decay. Additionally, other important requisites to consider are the insertion losses and the confinement capacity. Table 5.1 provides a comprehensive comparison of features for various electromagnetic field confinement devices. The table includes assessments of each structure's power-handling capability, operational capacity in radiative

mode, operating frequency, size in terms of wavelength, signal losses during propagation, confinement capacity (gain), presence of Floquet modes, and electric field patterns.

Concerning the advantages of the EMFCD based on air-filled waveguide, the main ones are their ability to handle high power and their low losses. Compared with the SIW device and [12], this design achieves low insertion losses. This enables the design of longer devices, expanding the illumination area, and be used in applications that require high power. Another advantage is that generates higher levels of electric field in the surface. As proven, with 90% less power supplied compared to the Substrate Integrated Waveguide device, it achieved almost two times higher electric field levels. Furthermore, this design has frequency scanning capability.

On the other hand, the key advantage of the EMFCD based on SIW is its simple and cost-effective design. Furthermore, being a uniform structure, it avoids the appearance of space harmonics, allowing only the fundamental mode to be present. Additionally, it demonstrates superior confinement capabilities due to significantly lower gain when compared to the waveguide design. As demonstrated, as the frequency approaches the light cone, the gain of the waveguide device increases from -10 dB to 0.2 dB. In contrast, the SIW design maintains a constant gain below $-$ 15 dB.

In this chapter, two novel electromagnetic field confinement devices are presented and characterized. One design based on SIW technology was designed for RFID applications, whereas the second, geared towards high-power applications such as energy transfer, operates between 3.6 - 4.2GHz. Specific design equations are developed for each structure. Both devices demonstrate an innovative approach to control the decay of the evanescent mode. Experimental results support the effectiveness of the proposed designs, opening opportunities for future enhancements and practical applications.

Table 5.1. Performance comparison of different Electromagnetic field confinement devices.

Ref.	Topology	Operation Frequency (GHz)	Floquet modes (cm)	Length (λ_0)	Electric field pattern (direction)	Losses (dB/cm)	High power capacity	Gain (dB)	Radiative capacity
[12]	CRLH	0.75 - 1	4	0.9	z	≈0.15	no	< - 20	Yes
5.1	SIW	0.84 - 1	no	1.72	y	≈0.05	no	< - 15	No
5.2	Waveguide	3.6 - 4.1	3	7.8	x	≈0.036	yes	< 0.2 < - 10	Yes

REFERENCES

[1] Finkenzeller, K. RFID Handbook: Radio-Frequency Identification Fundamentals and Applications (Wiley, Chichester, 2004).

[2] R. Cao and S. -C. Yu, "Wideband Compact CPW-Fed Circularly Polarized Antenna for Universal UHF RFID Reader," in IEEE Transactions on Antennas and Propagation, vol. 63, no. 9, pp. 4148-4151, Sept. 2015, doi: 10.1109/TAP.2015.2443156.

[3] S. Ahmed, A. Mehmood, L. Sydänheimo, L. Ukkonen and T. Björninen, "Glove-Integrated Textile Antenna with Reduced SAR for Wearable UHF RFID Reader," 2019 IEEE International Conference on RFID Technology and Applications (RFID-TA), Pisa, Italy, 2019, pp. 231-235, doi: 10.1109/RFID-TA.2019.8892251.

[4] R. Caso, A. Michel, A. Buffi, P. Nepa and G. Isola, "A modular antenna for UHF RFID near-field desktop reader," 2014 IEEE RFID Technology and Applications Conference (RFID-TA), Tampere, Finland, 2014, pp. 204-207, doi: 10.1109/RFID-TA.2014.6934228.

[5] A. Michel and P. Nepa, "UHF-RFID Desktop Reader Antennas: Performance Analysis in the Near-Field Region," in IEEE Antennas and Wireless Propagation Letters, vol. 15, pp. 1430-1433, 2016, doi: 10.1109/LAWP.2015.2511926

[6] A. Michel, A. Buffi, P. Nepa and G. Manara, "Antennas for UHF-RFID printer-encoders," 2015 IEEE 15th Mediterranean Microwave Symposium (MMS), Lecce, Italy, 2015, pp. 1-4, doi: 10.1109/MMS.2015.7375399.

[7] A. Michel, A. Buffi, P. Nepa and G. Manara, "Optimal antennas for RFID printer-encoders," 2016 IEEE International Symposium on Antennas and Propagation (APSURSI), Fajardo, PR, USA, 2016, pp. 1475-1476, doi: 10.1109/APS.2016.7696444.

[8] C. R. Medeiros, J. R. Costa and C. A. Fernandes, "RFID Smart Shelf With Confined Detection Volume at UHF," in IEEE Antennas and Wireless Propagation Letters, vol. 7, pp. 773-776, 2008, doi: 10.1109/LAWP.2008.2008672.

[9] J. S. Choi, H. Lee, D. W. Engels and R. Elmasri, "Passive UHF RFID-Based Localization Using Detection of Tag Interference on Smart Shelf," in IEEE

Transactions on Systems, Man, and Cybernetics, Part C (Applications and Reviews), vol. 42, no. 2, pp. 268-275, March 2012, doi: 10.1109/TSMCC.2011.2119312.

[10] A. Michel, M. Rodriguez Pino and P. Nepa, "Reconfigurable Modular Antenna for NF UHF RFID Smart Point Readers," in IEEE Transactions on Antennas and Propagation, vol. 65, no. 2, pp. 498-506, Feb. 2017, doi: 10.1109/TAP.2016.2640140.

[11] A. Michel, M. Rodriguez Pino and P. Nepa, "Reconfigurable Modular Antenna for NF UHF RFID Smart Point Readers," in IEEE Transactions on Antennas and Propagation, vol. 65, no. 2, pp. 498-506, Feb. 2017, doi: 10.1109/TAP.2016.2640140.

[12] Bonache, J., Zamora, G., Paredes, F. et al. Controlling the Electromagnetic Field Confinement with Metamaterials. Sci Rep 6, 37739 (2016).

[13] Robert E. Collin, "Foundations for Microwave Engineering", second edition, USA, New Jersey, IEEE Press, 2000

[14] David M. Pozar, "Microwave Engineering", fourth edition, Hoboken, NJ, USA:John Wiley & Sons Inc, 2011.

[15] D. Deslandes, "Design equations for tapered microstrip-to-Substrate Integrated Waveguide transitions," 2010 IEEE MTT-S International Microwave Symposium, Anaheim, CA, USA, 2010, pp. 704-707, doi: 10.1109/MWSYM.2010.5517884.

[16] Grine, Farouk & Benhabiles, Mohamed & mohamed lahdi, Riabi. (2017). Ku-band Transition with not Metalized Air-Vias between Microstrip Line and Substrate Integrated Waveguide. Journal of Microwaves, Optoelectronics and Electromagnetic Applications. 16. 50-58. 10.1590/2179-10742017v16i1778.

[17] "Guidelines for limiting exposure to time-varying electric magnetic and electromagnetic fields (up to 300 ghz)", Health Physics, vol. 74, no. 4, pp. 494-522, 1998.

[18] "ICNIRP Guidelines for Limiting Exposure to Time-Varying Electric Magnetic and Electromagnetic Fields (1 Hz to 100 kHz)", Health Physics, vol. 99, no. 6, pp. 818-836, December 2010.

[19] W. Yin et al., "Frequency Scanning Single-Ridge Serpentine Dual-Slot-Waveguide Array Antenna," in IEEE Access, vol. 8, pp. 77245-77254, 2020, doi: 10.1109/ACCESS.2020.2989318.

[20] E. S. Kireyev and Y. E. Mitelman, "Radiation pattern null elimination of the radiosonde antenna," 2013 23rd International Crimean Conference "Microwave & Telecommunication Technology", Sevastopol, Ukraine, 2013, pp. 606-607.

[21] V. Puri and H. S. Singh, "A Compact Ultrathin Metamaterial Absorber for C, K and Ka Band Microwave Frequency Regime," 2020 IEEE MTT-S Latin America Microwave Conference (LAMC 2020), Cali, Colombia, 2021, pp. 1-3, doi: 10.1109/LAMC50424.2021.9602614.

Chapter 6

Conclusions and future work

Conclusions

In this thesis, it has been proposed, analyzed and characterized leaky wave antennas and electromagnetic field confinement devices on different technologies and working principles. Furthermore, different microwave devices have been prototyped with 3D printing and diverse metallization process have been explored.

The thesis is structured into five chapters, in addition to this concluding chapter. After introducing the motivation and overarching objectives in Chapter 1, most relevant aspects discussed in each chapter and their conclusions are outlined below:

An overview of leaky wave antennas and electromagnetic field confinement devices is carried out in **Chapter 2**. This chapter presents various types of LWAs, along with the limitations and challenges associated with different topologies. It also explores potential applications and the current state of the art. Additionally, it details the concept of EMFCDs, their potential applications, market scope, and the theoretical development that has been used to delve into new designs for different scenarios.

Chapter 3 explores the use of 3D printing for making prototypes of microwave devices. The chapter looks into whether different materials and ways of metallization can be used to prototype different microwave devices using

planar and waveguide technology. The chapter examined if 3D printing can be practical for different radiofrequency (RF) devices. Furthermore, the chapter includes the characterization of the conductivity of various materials, such as silver paint ($\sigma = 5.6*10^6$ S/m), nickel spray ($1.05*10^4$), aluminium adhesive tape ($\sigma = 4.72*10^6$ S/m), and the Electrifi 3D printing material ($\sigma = 2.88$ S/m). Both silver paint and aluminium tape yielded good results in terms of electrical conductivity. However, in the case of the Electrifi material and nickel spray, very low conductivity levels were obtained. An improvement in conductivity was also obtained by applying a galvanization process to both silver paint and nickel spray, increasing the electrical conductivity by 10% and 100%, respectively. Practical experimentation is conducted with a stepped impedance filter and a functional horn antenna, both manufactured using PLA. While the actual results might not have matched the original plans, this work forms a solid foundation for the following chapters. Important materials like aluminium tape and silver paint are used to reduce reflection losses and add metal coatings to the Substrate Integrated Waveguide (SIW) structure.

In **Chapter 4** a novel periodic leaky-wave antenna with backward to forward scanning capability is presented. The proposed arrangement, composed of 30 UCs, along with the proposed design approach, successfully suppresses the open stopband, a common issue to deal in periodic LWAs that degrades the radiated beam around the broadside direction. Furthermore, the proposed air-filled structure has a narrower lateral profile, which allows placing several of them side-by-side to obtain a pencil beam. This proposed configuration achieves an efficient broadside radiation at 5 GHz with a high radiation efficiency without any grating lobes. Moreover, two unidirectional versions are analyzed by mean of software simulation. The backing trough design exhibited higher performance compared to the unidirectional ground plane-based design in terms of degradation of open stopband. Within this context, both antenna versions (with unidirectional and bidirectional radiation pattern) have been designed, fabricated, and characterized. Furthermore, a modular matching network based on coaxial to waveguide transition was designed to achieve an efficient power transmission between 4.2 to 6 GHz. The simulated results showed a radiation efficiency between 83 to 97 % and 72 to 93% for the bidirectional and unidirectional versions. The measured and simulated S-parameters, radiation pattern, and gain were reported and compared. The experimental results

showed a backward to forward scanning capability from $-35°$ to $42°$ for both the unidirectional and bidirectional versions. The scanning angle demonstrated a high linearity dependency with frequency. The maximum measured gain was 15.5 dB in the bidirectional configuration and 16.5 dB in the unidirectional version.

Chapter 5 is dedicated to the analysis of novel electromagnetic field confinement devices. These devices generate an evanescent wave, in which the field decay in the broadside direction can be predicted based on design equations. In subchapter 5.1, an electromagnetic field confinement device tailored for RFID applications under the European protocol (867 MHz) has been developed. Design equations were introduced to regulate the attenuation constant of the field, and a corresponding design procedure was also put forward, providing a comprehensive approach to controlling the evanescent wave's characteristics. The device was built on a substrate integrated waveguide structure, featuring a longitudinal slit along the propagation direction located at the center of the wide wall. An exponential tapered transition connects the access lines and the SIW structure. In that chapter, the simulated electric field generated on the surface of the structure was presented and analyzed. The radiation pattern, S-parameters, and electric field were simulated and measured. The electric field measurements were taken using an electric field probe. This design emphasizes simplicity and cost-effectiveness. In this design, the measured results closely matched the theoretical ones, validating the design process and the proposed theoretical equations. On the other hand, subchapter 5.2 introduced an EMFCD based on air-filled waveguide. This design used the same periodic structure analized in chapter 4 as LWA, is studied in surface wave mode. The proposed device was based on a periodic serpentine rectangular waveguide loaded with transverse rectangular slots and a transition between the coaxial cable and the serpentine. A prototype was designed, fabricated, and measured with an operation frequency between 3.6 to 4.2 GHz. Two versions (unidirectional and bidirectional) were analyzed. The design methodology has been demonstrated with accuracy to predict the field decay in broadside direction. However, the gain of the waveguide device increases from -10 dB to 0.2 dB as the frequency approaches the light cone. The measured insertion losses corresponded to an attenuation of 0.035 and 0.036 dB/cm in unidirectional and bidirectional designs respectively. The low

insertion losses facilitate the possibility of expanding the illuminated area if needed.

Future Work

Some further work may be conducted in the research lines that have emerged from this thesis. Among these, it is worth highlighting:

- The possibilities regarding the design of EMFCDs are countless. In the context, the analysis of new travelling wave structures in order to reduce the transmission losses, increasing the confinement capability, reduce the dimensions, among other performances could be an interesting research line to develop.
- Fully design a wireless energy transfer system for high-power applications based on the air-filled structure proposed in this thesis. This includes study the possibility of incorporating RF absorbent material, among other approaches to address leakage in backward radiation presented near the light cone and the design of a receiver system.
- Study the viability of prototyping with resin and laser 3D printer for microwave devices. These types of 3D printer offer much resolution than the traditional. Furthermore, new conductive materials that can be useful in microwave devices prototypes have emerged in recent years.
- Examinate a new unit cell for LWAs that allows the elimination of the OSB using pillars. Investigate the possibility of creating radiation patterns with low levels of secondary lobes by considering current distributions generated not only by the width and length of the slots but also incorporating the depth of the slot.

APPENDIX I

Analyses of the frequency scanning linearity in serpentine arrangement

The first derivative provides information about the rate and direction of change of the function at various points, and the second derivative provides additional information about the concavity and the acceleration of the function's change. By analyzing the derivate and the second derivate of the scanning angle at a specific point, one can obtain the parameters that will directly affect the linearity of the frequency scanning and the scan ratio.

The first frequency derivate of the angle θ of the main radiated beam in the serpentine arrangement can be written as

$$\frac{\partial\theta}{\partial k} = \frac{\partial sen^{-1}\left(\frac{\beta_n^a}{k}\right)}{\partial k} = \frac{\partial sen^{-1}\left(\left(\frac{L}{d}\sqrt{1-\left(\frac{k_c}{k}\right)^2}+\frac{2\pi n}{kd}\right)\right)}{\partial k} \qquad (A.1)$$

where d is the distance between two consecutive slots corresponds, n is a specific space harmonic, k_c is the cutoff wavenumber, L is the length of the serpentine, and k is the wavenumber. Solving $(A.1)$ derivate the following result is achieve

APPENDIX I

$$\frac{\partial\theta}{\partial k}=\frac{\left(\frac{Lk_c{}^2}{dk^3\sqrt{1-\frac{k_c{}^2}{k^2}}}-\frac{2\pi n}{k^2 d}\right)}{\left(\sqrt{1-\left(\frac{L}{d}\sqrt{1-\left(\frac{k_c}{k}\right)^2}+\frac{2\pi n}{kd}\right)^2}\right)^{3/2}} \tag{A.2}$$

By focusing on the frequency where broadside radiation is achieved the length of the serpentine must be

$$L=\frac{-2\pi n}{k_b\sqrt{1-\frac{k_c{}^2}{k_b{}^2}}} \tag{A.3}$$

where k_b is the wavenumber in broadside radiation. At $k = k_b$, the second derivate can be expressed as

$$\left.\frac{\partial\theta}{\partial k}\right|_{k=k_b}=\boxed{\frac{-2\pi n}{dk_b{}^2}\left(\frac{k_c{}^2}{k_b{}^2-k_c{}^2}+1\right)} \tag{A.4}$$

In the case of the second frequency derivate of the angle θ of the main radiated beam can be written as

$$\frac{\partial^2\theta}{\partial^2 k}=\frac{\partial^2 sen^{-1}\left(\left(\frac{L}{d}\sqrt{1-\left(\frac{k_c}{k}\right)^2}+\frac{2\pi n}{kd}\right)\right)}{\partial k^2} \tag{A.5}$$

Deriving (A.5) yields the following result

$$\frac{\partial^2\theta}{\partial^2 k}=\frac{\left(\frac{L}{d}\sqrt{1-\frac{k_c{}^2}{k^2}}+\frac{2\pi n}{kd}\right)\left(\frac{Lk_c{}^2}{dk^3\sqrt{1-\frac{k_c{}^2}{k^2}}}-\frac{2\pi n}{k^2 d}\right)^2}{\left(\sqrt{1-\left(\frac{L}{d}\sqrt{1-\left(\frac{k_c}{k}\right)^2}+\frac{2\pi n}{kd}\right)^2}\right)^{3/2}}+\frac{\frac{4\pi n}{k^3 d}-\frac{Lk_c{}^4}{dk^6\left(1-\frac{k_c{}^2}{k^2}\right)^{\frac{3}{2}}}-\frac{3Lk_c{}^2}{dk^4\sqrt{1-\frac{k_c{}^2}{k^2}}}}{\sqrt{1-\left(\frac{L}{d}\sqrt{1-\left(\frac{k_c}{k}\right)^2}+\frac{2\pi n}{kd}\right)^2}} \tag{A.6}$$

Finally, in broadside radiation the second derivate will be

$$\left.\frac{\partial^2\theta}{\partial^2 k}\right|_{k=k_b} = \frac{4\pi n}{d{k_b}^3}\left(1+\left(\frac{{k_c}^4}{2{k_b}^4\left(1-\left(\frac{k_c}{k_b}\right)^2\right)^2}\right)+\left(\frac{3{k_c}^2}{2{k_b}^2\left(1-\left(\frac{k_c}{k_b}\right)^2\right)}\right)\right) \quad (A.7)$$

Appendix I

APPENDIX II

Analyses of the residual radiation in finite EMFCDs

Reciprocal space, also known as *k*-space, offers a visualization of the outcomes resulting from the Fourier transform of a spatial function. The reciprocal space is a space over which the Fourier transform of a spatial function is represented at spatial frequencies or wavevectors of plane waves of the Fourier transform. The domain of the spatial function itself is commonly known as real space.

The transmitted signal and the window function (given the finite nature of the structure) in real space will be defined as

$$f(x) = A \cdot e^{-jx\beta} \tag{A.8}$$

$$f_2(x) = \begin{cases} 1, & |x| \leq \dfrac{L}{2} \\ 0\,, & |x| > \dfrac{L}{2} \end{cases} \tag{A.9}$$

respectively, where A is the signal amplitude, x is the spatial position, L is the total length of the structure, and β is the effective phase constant of the propagated signal. The Fourier transform of A8 and A9 are A10 and A11 respectively

APPENDIX II

$$X(k) = \int_{-\infty}^{+\infty} A \cdot e^{-jx\beta} e^{-jkx}\, dx = A\pi\big(\delta(k-\beta)\big) \qquad (A.10)$$

$$X_2(k) = \int_{-\infty}^{+\infty} x_2(x)\, e^{-jkx}\, dx = sinc(kx) \qquad (A.11)$$

The multiplication of these functions will be

$$X(k)X_2(k) = A\pi\big(sinc(k-\beta)\big) \qquad (A.12)$$

Even in the surface mode, a portion of the secondary lobes can enter within the light cone, explaining the phenomenon of leakage radiation. Furthermore, near the boundary between the surface mode and the radiative mode, a portion of the main lobe may enter within the cone of light. Since the width level of the lobes increase inversely proportional to the width of the rectangular pulse, it can be deduced that by increasing the total length of the structure, the level of leakage radiation can be reduced. Figure AP1 shows a representation of three structures in surface wave mode with different lengths.

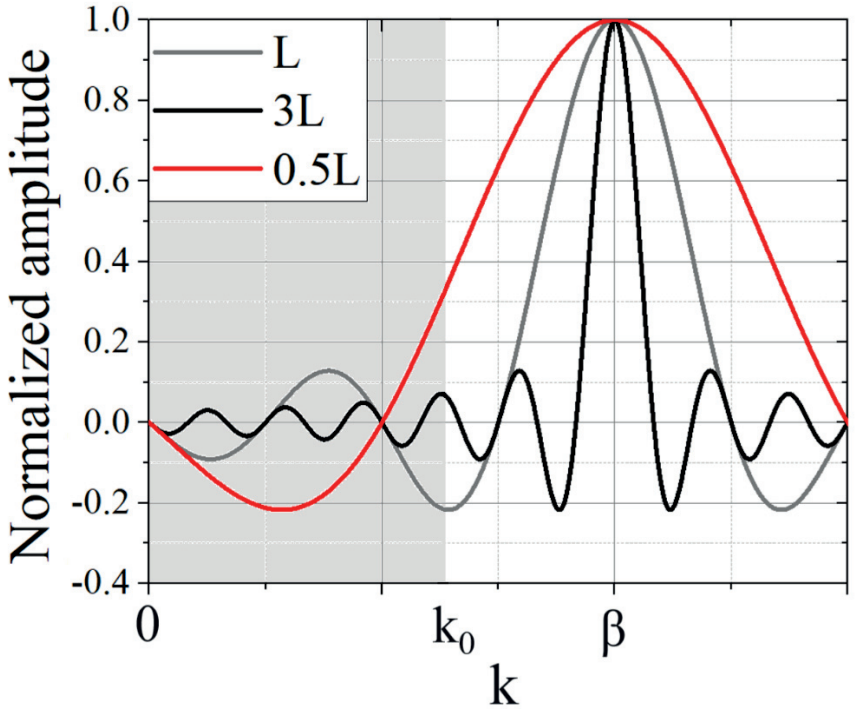


Figure AP1 Representation of the same structure with different total length. Radiation region is highlighted in gray

Author list of publications

International Journals

- Á. Jaque, G. Zamora and J. Bonache, "Frequency Scanning Leaky-wave Slot Antenna Array Based on Serpentine Waveguide with Open Stopband Suppression," in IEEE Antennas and Wireless Propagation Letters, doi: 10.1109/LAWP.2023.3324063.
- Á. Jaque, G. Zamora and J. Bonache, "A Novel Electromagnetic Field Confinement Device Based on Slotted Serpentine Waveguide", in process of publication.
- Á. Jaque, G. Zamora and J. Bonache, "Novel Electromagnetic Field Confinement Device SIW Technology-based for RFID Near-field Applications", in process of publication.

International Conferences

- Á. Jaque, G. Zamora and J. Bonache, "Slotted waveguide leaky-wave antenna based on meandered delay-lines", IEEE International Symposium on Antennas and Propagation and USNC-URSI Radio Science Meeting, Denver, Colorado, USA, July 2022.